

Photodisruption in biological tissues using femtosecond laser pulses

A thesis presented

by

Nan Shen

to

The Department of Physics

in partial fulfillment of the requirements

for the degree of

Doctor of Philosophy

in the subject of

Physics

Harvard University

Cambridge, Massachusetts

January, 2003

Photodisruption in biological tissues using femtosecond laser pulses

Abstract

Transparent materials do not ordinarily absorb visible or near-infrared light. However, the intensity of a tightly focused femtosecond laser pulse is great enough that nonlinear absorption of the laser energy takes place in transparent materials, leading to optical breakdown and permanent material modification. Because the absorption process is nonlinear, absorption and material modification are confined to the extremely small focal volume.

Optical breakdown in transparent or semi-transparent biological tissues depends on intensity rather than energy. As a result, focused femtosecond pulses induce optical breakdown with significantly less pulse energy than is required with longer pulses. The use of femtosecond pulses therefore minimizes the amount of energy deposited into the targeted region of the sample, minimizing mechanical and thermal effects that lead to collateral damage in adjacent tissues.

We demonstrate photodisruptive surgery in animal skin tissue and single cells using 100-fs laser pulses. In mouse skin, we create surface incisions and subsurface cavities with much less collateral damage to the surrounding tissue than is produced with picosecond pulses. Using pulses with only a few nanojoules of energy obtained from an unamplified femtosecond oscillator, we destroy single mitochondria in live cells without affecting cell viability, providing insights into the structure of the mitochondrial network. An apparatus is constructed to perform subcellular surgery and multiphoton 3D laser scanning imaging simultaneously with a single laser and objective lens.

© 2003 by Nan Shen
All rights reserved.

For my parents and Aunt Qingyun

Acknowledgments

I am indebted to my advisor professor Eric Mazur for the opportunity to work in his group and his support throughout my thesis research. Eric has set for me a high standard of clarity of thinking and expression. I know the skills that I have learned from him will always serve me well in the years to come.

Because of Eric's gift for choosing graduated students who integrate well into the group, I have had the pleasure of working with a number of great fellow group members. I have learned tremendously from working with Chris Schaffer and Nozomi Nishimura on the laser surgery project. Debajyoto Datta joined the project in his sophomore year. We have walked through many ups and downs together. Although Phil LeDuc and I started collaboration only a year ago, Phil has become an important member of the team and has been a source of innovation. I also want to thank Jon Ashcom, Chris Roeser, Jim Carey, and Rafael Gattass, each of whom has provided a large amount of quite unreciprocated aid. I am grateful for the invaluable advises Catherine Crouch has given me over the years. My heartfelt thanks are extended to Adam Fagan, who not only helped me improve the thesis, but also made the long hours before graduation infinitely less painful which I will always remember. The new members of the Mazur group, Maria Kandyla, Iva Maxwell, and Sam Chung have brought refreshed enthusiasm and energy to the group and to me. Thank you for the great experience of being part of the Mazur group.

Table of Contents

Abstract

Chapter 1: Introduction.....1

Chapter 2: Propagation of ultrashort laser pulses in transparent materials.....7

2.1	Linear propagation.....	8
2.2	Nonlinear propagation.....	9
2.2.1	The nonlinear index of refraction.....	10
2.2.2	Self-focusing.....	12
2.2.3	Filamentation.....	16
2.2.3.1	Self-channeling of laser beam.....	17
2.2.3.2	The moving focus model.....	17
2.3	Femtosecond laser induced optical breakdown.....	19
2.3.1	Multiphoton and tunneling ionization.....	20
2.3.2	Avalanche ionization.....	21
2.3.3	Plasma absorption.....	22
2.3.4	Discussion.....	24
2.4	Laser systems.....	25
2.4.1	Regenerative femtosecond laser amplifier.....	26
2.4.2	Long-cavity oscillator.....	28
	References.....	29

Chapter 3: Femtosecond laser surgery in turbid tissue..... 32

3.1	Light propagation in turbid tissues.....	32
3.1.1	Reflection and refraction.....	32
3.1.2	Absorption.....	35
3.1.3	Scattering.....	37
3.1.4	Lasers for turbid tissue surgery.....	38
3.2	Laser tissue surgery mechanisms.....	39
3.2.1	Photochemical interaction.....	40
3.2.2	Thermal interaction.....	41
3.2.3	UV ablation.....	43
3.2.4	Plasma-induced ablation and disruption.....	44
3.3	Femtosecond laser photodisruption.....	47
3.3.1	Introduction.....	48
3.3.2	Experimental setup.....	51
3.3.3	Sample preparation and processing.....	52
3.3.4	Results and discussion.....	53

3.3.4.1	Precise incision.....	53
3.3.4.2	Subsurface disruption.....	54
3.3.4.3	Subsurface filamentation.....	56
3.4	Conclusion.....	60
	References.....	62
Chapter 4: Disruption of subcellular organelles inside live cells.....		67
4.1	Introduction.....	67
4.2	Optical imaging of cells.....	73
4.2.1	Fluorescent imaging.....	74
4.2.2	Confocal laser scanning microscopy.....	76
4.3	Fluorescence methods.....	78
4.3.1	Immunological staining.....	79
4.3.2	Fluorescent protein.....	80
4.4	Results and discussion.....	83
4.4.1	Disruption in fixed cells.....	83
4.4.2	Disruption in live cells.....	88
4.4.3	Discussion.....	91
4.5	Applications.....	92
4.6	Conclusion.....	96
	References.....	97
Chapter 5: Multiphoton imaging with a modified femtosecond laser oscillator.....		101
5.1	Principles of multiphoton laser scanning microscopy	101
5.1.1	Multiphoton vs. single photon imaging.....	102
5.1.2	Resolution of multiphoton imaging.....	105
5.1.3	Discussion.....	107
5.1.3.1	Absorption cross-section of fluorophores	108
5.1.3.2	Photobleaching and photodamage of fluorophores	110
5.2	Microscope setup.....	112
5.2.1	Laser source.....	113
5.2.2	Scanning system.....	114
5.2.3	Detection.....	116
5.2.4	Combining multiphoton imaging with subcellular surgery.....	117
5.3	System performance and discussion.....	118
5.4	Summary.....	120
	References.....	121
Chapter 6: Outlook.....		127

List of Figures

Figure 2.1 Nonlinear index of refraction and self-focusing of a laser beam.....	12
Figure 2.2 Total internal reflection and self-focusing.....	13
Figure 2.3 The moving focus model of filamentation.....	18
Figure 2.4 Schematic diagrams of multiphoton and tunneling ionization.....	20
Figure 2.5 Schematic diagram of avalanche ionization.....	22
Figure 2.6 Reflectivity of a plasma.....	24
Figure 2.7 Schematic diagram of a Ti:sapphire laser oscillator.....	27
Figure 3.1 Schematic diagram of the structure of skin tissue.....	34
Figure 3.2 Absorption spectrum of water.....	36
Figure 3.3 Temperature profile in water after laser irradiation.....	43
Figure 3.4 Radius of the laser-produced plasma, pressure wave, and cavitation bubble in water.....	45
Figure 3.5 Surface and bulk disruption in skin tissue with femtosecond and picosecond laser pulses.....	49
Figure 3.6 Schematic diagram of laser disruption in skin tissue.....	51
Figure 3.7 Femtosecond laser incision in mouse skin tissue.....	53
Figure 3.8 Subsurface cavities in mouse skin tissue.....	55
Figure 3.9 Subsurface cavities in mouse skin tissue produced with two different laser pulse energy.....	55
Figure 3.10 Filaments in pig skin tissue.....	57
Figure 3.11 Filaments in mouse skin tissue.....	57
Figure 4.1 Energy threshold for plasma generation in water for different laser pulse durations and the corresponding temperature change.....	70
Figure 4.2 Schematic diagram of the cell surgery setup.....	73
Figure 4.3 Energy diagram of the fluorescence.....	74
Figure 4.4 Absorption and emission spectra of fluorescein and rhodamine.....	76
Figure 4.5 Epi-fluorescence microscope image of a fixed fibroblast cell.....	76
Figure 4.6 Schematic illustration of the function of the pinhole in the confocal microscope.....	78
Figure 4.7 Spectral response of the fluorescent filter sets.....	80
Figure 4.8 Epi-fluorescence microscope image of a live BCE cell with YFP-transfected mitochondria.....	81
Figure 4.9 Absorption and emission spectra of five fluorescent proteins.....	82
Figure 4.10 Images of a fixed fibroblast cell before and after CW and femtosecond laser irradiation.....	84

Figure 4.11 Confocal microscope image of a fixed fibroblast cell with femtosecond laser disruption.....	86
Figure 4.12 Confocal microscope images of a fixed fibroblast cell after disruption using 2 nJ laser pulses.....	87
Figure 4.13 Images of a fixed fibroblast cell after disruption using 1.5 nJ laser pulses...	88
Figure 4.14 Disruption of a single mitochondrion in a live BCE cell.....	89
Figure 4.15 Test of cell viability of laser disruption using ethidium bromide.....	91
Figure 4.16 Disruption of a single mitochondrion in a live BCE cell and observation of fluorescence intensity change over time.....	95
Figure 4.17 Laser disruption effects on the microtubule network	96
Figure 5.1 Schematic diagram of the excitation volume in single- and multiphoton imaging.....	103
Figure 5.2 Energy diagrams of single- and multiphoton fluorescence.....	104
Figure 5.3 Schematic diagram of setup for femtosecond laser cell surgery with multiphoton imaging.....	112
Figure 5.4 Schematic illustration of the principle of scanning optics.....	115
Figure 5.5 Multiphoton microscope image of fluorescent microspheres.....	119

List of Tables

Table 3.1 Laser light penetration depth in skin tissue.....	12
Table 3.2 Dissociation energy of selected chemical bonds.....	13
Table 4.1 Threshold intensities and energies of plasma generation in water for different laser pulse durations.....	18

Chapter 1

Introduction

Since its invention in the 1960s [1], the laser has steadily gained recognition as an important tool in both basic scientific research and technology. Experiments with lasers have enhanced understanding of how light interacts with matter; particularly in nonlinear regimes; lasers were also used to permanently change the properties of materials. The development of femtosecond pulsed lasers in the 1980s [2, 3] opened up additional exciting possibilities in many fields. Today, femtosecond lasers are used to study chemical reactions, probe material properties, image single molecules, and machine a wide range of materials with great precision.

Femtosecond laser pulses are brief enough that they can be used to examine processes too rapid to study with other instruments. The time course of bond-breaking in chemical reactions and electron-electron, electron-phonon, and phonon-phonon interactions in materials can be probed with femtosecond laser pulses. Focused femtosecond laser pulses with moderate pulse energy generate high electric field intensities, which is otherwise difficult to obtain. With such high intensity, extreme nonequilibrium conditions are created. One example is the almost instantaneous

generation of a large number of hot electrons in a material with cold ions. The high field intensity of a femtosecond laser pulse can easily exceed the Coulomb potential (10^9 W/cm²) that binds electrons to the ionic core in atoms. As a result, valence electrons in almost any material can be ionized through nonlinear mechanisms such as multiphoton and avalanche ionization. Ionization causes optical breakdown, permanently modifying the material [4].

In this thesis we present an experimental study of the interaction of femtosecond laser pulses with transparent and semi-transparent biological tissues, such as skin and cell cultures. We explore the potential of using femtosecond laser induced optical breakdown to precisely manipulate tissue, cells and subcellular structures for medical and biological research. The remainder of this thesis is organized as follows:

Chapter 2: Propagation of femtosecond laser pulses in transparent materials

This chapter briefly reviews the nonlinear optical interactions which govern how materials respond to high intensity laser pulses. We describe both self-focusing phenomena arising from the intensity-dependent index of refraction and mechanisms of nonlinear ionization which lead to material modification. The different laser systems used in the experiments are also described.

Chapter 3: Ultrashort laser pulses in turbid tissue

When a powerful femtosecond laser pulse is focused in a material, the high intensity created at the focus causes nonlinear ionization that can vaporize material in the focal

volume. In this chapter, we present experimental results on femtosecond laser disruption of turbid tissues. The optical properties of skin tissue are briefly discussed, and a short review of existing techniques for laser ablation of tissue, as well as their mechanisms, is presented. We use a microscope objective lens to tightly focus the femtosecond laser pulses both on the surface and in the bulk of skin tissues. Both removal of surface tissue and incision through different tissue layers can be performed with higher precision than other techniques. We also demonstrate that femtosecond laser pulses can be used to create cavities in the bulk of a tissue without affecting the tissue surface. The size of the cavity is determined by the laser energy deposited in the tissue. Applications of precise tissue surgery with femtosecond laser pulses are described.

Chapter 4: Disruption of subcellular organelles in live cells

The high precision of material modification with femtosecond pulses permits us to target subcellular organelles in fixed and live cells. Using fixed cell samples, we determine that the energy threshold for femtosecond laser disruption of structures in cells is on the order of nanojoules. At this energy, disruption of a single subcellular organelle, such as a mitochondrion, can be carried out within a live cell without affecting cell viability. We apply the femtosecond subcellular disruption technique to study mitochondrial organization in bovine capillary endothelial (BCE) cells.

Chapter 5: Multiphoton imaging and future directions

Disruption in live cells requires nanojoules of laser pulse energy, which is within the energy range of a commercially available femtosecond laser oscillator. Furthermore, the high repetition pulses from an oscillator can be used for multiphoton imaging. Combining multiphoton imaging with laser photodisruption, therefore permits us to probe subcellular structures and observe cellular responses with high resolution in three dimensions. We use a femtosecond laser oscillator modified to produce a 25-MHz pulse train with pulse energies up to 20 nJ. The high-repetition-rate pulse train can be used for multiphoton imaging of cell samples; to disrupt target cellular structures, laser pulses can be switched out using an acousto-optic modulator. Multiphoton imaging has several advantages over conventional techniques such as epi-fluorescence and confocal microscopies. In this chapter we describe the physical basis and technical advantages of multiphoton laser scanning imaging, and explain how it can be combined with femtosecond laser disruption using a single laser and microscope objective.

Chapter 6: Conclusion and outlook

A summary of the principles involved in photodisruption of biological materials is presented. Despite extensive research on optical breakdown in transparent materials with femtosecond laser pulses, many open questions remain. Because biological systems are intrinsically complex, further studies are needed to better characterize laser-tissue interactions. Nevertheless, femtosecond laser disruption is demonstrated to be a unique

and useful tool for precise surgery at both the tissue and subcellular levels. Key results presented in this thesis are reviewed and future experiments are suggested.

References

1. T. H. Maiman, *Nature* **187**, 493 (1960).
2. R. L. Fork, C. V. Shank, R. Yen, *et al.*, *IEEE Journal of Quantum Electronics* **QE-19**, 500 (1983).
3. R. L. Fork, B. I. Green, and C. V. Shank, *Applied Physics Letters* **38**, 71 (1981).
4. N. Bloembergen, *IEEE Journal of Quantum Electronics* **QE-10**, 375 (1974).

Chapter 2

Propagation of ultrashort laser pulses in transparent materials

Propagation of light in a medium is a complex process. Depending on the properties of the incident light and the material, light can be affected by and can also modify the material. Because of the ultra-short duration and the resulting high peak power of the laser pulse we are using in this study, the material response to the incident laser light is drastically different from our daily experience of light-matter interaction, where light is produced by either the sun or a lamp. In this chapter, we briefly review some of the basic physics principles that govern light-matter interaction. We will concentrate specifically on transparent or nearly transparent materials that have low absorption in the visible to near infrared range of the electromagnetic wave spectrum.

In the first two sections of this chapter, we exam how the propagation of a laser pulse with moderate intensity gets affected by the medium and introduce nonlinear processes such as self-focusing induced filamentation. When the intensity of the laser pulse gets even higher, optical breakdown can occur and the material is modified by the

laser light. In the third part of the chapter, we will look at mechanisms responsible for such permanent modification in transparent materials. A brief overview of the lasers used in this study will also be presented at the end.

2.1 Linear propagation

The propagation of an electromagnetic wave in a medium is governed by the Maxwell's equations (in SI units) [1-3]

$$\begin{aligned}\nabla \cdot \mathbf{D} &= \rho \\ \nabla \cdot \mathbf{B} &= 0 \\ \nabla \times \mathbf{E} &= -\frac{\partial \mathbf{B}}{\partial t} \\ \nabla \times \mathbf{H} &= \frac{\partial \mathbf{D}}{\partial t} + \mathbf{J},\end{aligned}\tag{2.1}$$

and

$$\begin{aligned}\mathbf{D} &= \varepsilon_0 \mathbf{E} + \mathbf{P} \\ \mathbf{H} &= \frac{1}{\mu_0} \mathbf{B} - \mathbf{M},\end{aligned}\tag{2.2}$$

where ε_0 and μ_0 are the permittivity and permeability of free space. Assuming there is no free charge, no free current, and the material is nonmagnetic, we can reduce equation (2.1) using (2.2)

$$\nabla \times \nabla \times \mathbf{E} + \frac{1}{c^2} \frac{\partial^2 \mathbf{E}}{\partial t^2} = -\frac{1}{\varepsilon_0 c^2} \frac{\partial^2 \mathbf{P}}{\partial t^2}.\tag{2.3}$$

This is the most general form of the wave equation in optics. In conventional optics when the electric field strength is small, the polarization vector \mathbf{P} is a linear function of $\mathbf{E}(\mathbf{r}, t)$

$$\mathbf{P}(\mathbf{r}, t) = \varepsilon_0 \tilde{\chi}^{(1)} \mathbf{E}(\mathbf{r}, t),\tag{2.4}$$

where $\tilde{\chi}^{(1)}$ is the first order susceptibility tensor, a material dependent parameter. For an isotropic medium, the linear susceptibility is defined as the scalar quantity $\chi^{(1)}$. This further simplifies equation (2.4)

$$\nabla \times \nabla \times \mathbf{E} + \frac{n_0^2}{c^2} \frac{\partial^2 \mathbf{E}}{\partial t^2} = 0, \quad (2.5)$$

where n_0 is the index of refraction

$$n_0 = \sqrt{1 + \chi^{(1)}}. \quad (2.6)$$

2.2 Nonlinear propagation

The linear relation between \mathbf{P} and \mathbf{E} in equation (2.4) is only an approximation. At high field strengths, it is no longer valid. The dependence of the polarization on the field becomes nonlinear and is generally described as a power series of the electric field

$$\begin{aligned} \mathbf{P} &= \mathbf{P}^{(1)} + \mathbf{P}^{(2)} + \mathbf{P}^{(3)} + \dots \\ &= \epsilon_0 (\tilde{\chi}^{(1)} \mathbf{E} + \tilde{\chi}^{(2)} \mathbf{E} \mathbf{E} + \tilde{\chi}^{(3)} \mathbf{E} \mathbf{E} \mathbf{E} + \dots). \end{aligned} \quad (2.7)$$

In isotropic materials, the polarization vectors that are even powers of \mathbf{E} have to vanish in order to satisfy symmetry requirements. Equation (2.7) is thus reduced to

$$\begin{aligned} \mathbf{P} &= \mathbf{P}^{(1)} + \mathbf{P}^{(3)} + \dots \\ &= \epsilon_0 (\tilde{\chi}^{(1)} \mathbf{E} + \tilde{\chi}^{(3)} \mathbf{E} \mathbf{E} \mathbf{E} + \dots). \end{aligned} \quad (2.8)$$

In general, the nonlinear susceptibility is a complex quantity relating the complex amplitudes of the electric field and polarization. The magnitude of $\tilde{\chi}^{(n)}$ quickly decreases as the order n increases. For condensed matter, $\chi^{(n+1)} / \chi^{(n)}$ is of the order of $1/E_{\text{atom}} [3, 4]$, where E_{atom} is the binding field for the electron and is typically $\sim 10^8$ V/cm.

Therefore for incident light field with low strength, higher order polarizations are often neglected, and the observation of optical phenomena due to nonlinear polarizations requires high intensity laser beams¹.

2.2.1 The nonlinear index of refraction

In the case of weak nonlinearity, when the excitation field is far from any resonance, it is sufficient to truncate the series in equation (2.8) and retain only the third-order term. The field \mathbf{E} can be made up of several different frequency components, but as a simplification, let us consider a monochromatic field

$$\mathbf{E}(t) = \mathbf{E} \cos \omega t. \quad (2.9)$$

Substituting Equation (2.9) into Equation (2.8) and retain only the second term $\mathbf{P}^{(3)}$, the third-order polarization, we get

$$\mathbf{P}^{(3)} = \frac{1}{4} \chi^{(3)} \mathbf{E}^3 \cos 3\omega t + \frac{3}{4} \chi^{(3)} \mathbf{E}^3 \cos \omega t. \quad (2.10)$$

The first term in equation (2.10) describes a process called the third-harmonic generation. The second term describes the nonlinear contribution to the polarization at the same frequency of the incident field. The total polarization \mathbf{P} at the incident frequency can be expressed as

$$\mathbf{P} = \mathbf{P}^{(1)} + \mathbf{P}^{(3)} = \epsilon_0 (\chi^{(1)} + \chi^{(3)} |\mathbf{E}|^2) \mathbf{E} = \epsilon_0 \chi_{eff} \mathbf{E}, \quad (2.11)$$

where we have defined the effective susceptibility

$$\chi_{eff} = \chi^{(1)} + \frac{3}{4} \chi^{(3)} |\mathbf{E}|^2. \quad (2.12)$$

¹ The field strength of unfocused sun light is on the order of ~ 10 V/cm. Femtosecond laser pulses have peak power of gigawatts and can easily reach a field strength of $\sim 10^9$ V/cm.

Substituting equation (2.11) into the wave equation, we get the modified index of refraction

$$\begin{aligned} n &= \sqrt{1 + \chi^{(1)} + \frac{3}{4} \chi^{(3)} |\mathbf{E}|^2} \\ &\cong n_0 + \frac{\frac{3}{4} \chi^{(3)} |\mathbf{E}|^2}{2n_0}. \end{aligned} \quad (2.13)$$

Rewriting equation (2.13) in terms of the time-averaged intensity of the optical field I , we have

$$n = n_0 + n_2 I, \quad (2.14)$$

where

$$I = \frac{1}{2} \varepsilon_0 c n_0 |\mathbf{E}|^2, \quad (2.15)$$

and

$$n_2 = \frac{\frac{3}{4} \chi^{(3)}}{\varepsilon_0 c n_0^2}. \quad (2.16)$$

Under high intensity laser irradiation, materials with a third-order susceptibility will generate an intensity dependent contribution to the index of refraction, an effect called the optical Kerr nonlinearity. The typical values of n_2 for dielectric materials are small but positive at frequency far from resonance, roughly 10^{-14} – 10^{-17} cm²/W. In our study, we tightly focus femtosecond laser pulses in transparent or nearly transparent dielectric materials, which generate high intensity at the focus (10^{13} W/cm²). The intensity dependent index of refraction plays an important role in determining light propagation in the material.

2.2.2 Self-focusing

The intensity-dependent index of refraction gives rise to an optical phenomenon called self-focusing. As illustrated in Figure 2.1, when a laser pulse with a gaussian transverse intensity distribution is incident on a material with third-order nonlinearity, the intensity profile produces a gaussian transverse refractive index distribution. The material at the center of laser beam sees a higher intensity and produces a larger index of refraction than the material at the wings of the beam. As a result, the material is turned effectively into a positive lens, and tends to focus the incident laser beam. When an external focusing lens is used, the final focus appears closer to the beam entrance than predicted by the focusing lens only.

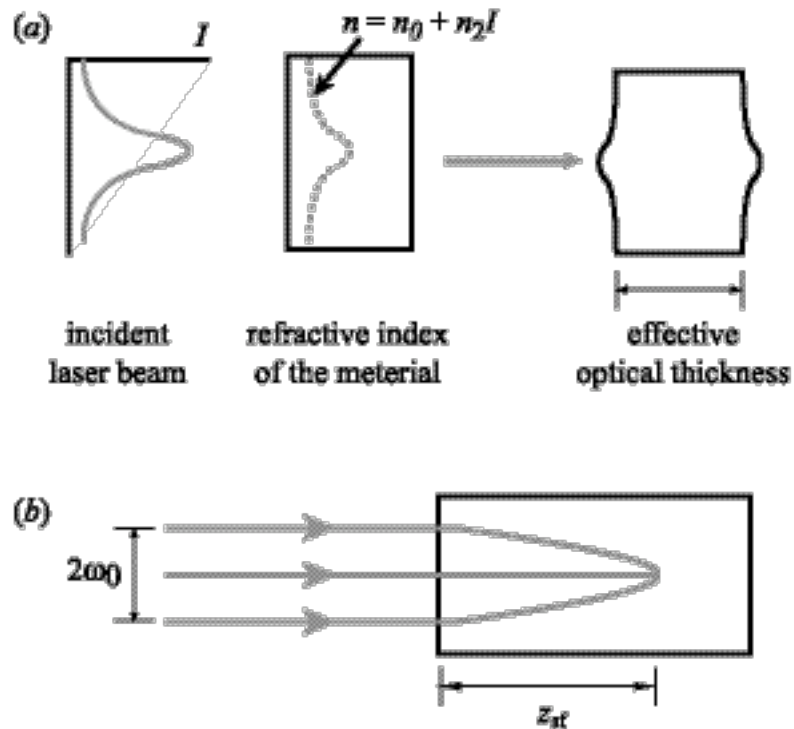


Figure 2.1 Self-focusing of a laser beam. (a) An intense laser beam with a gaussian spatial profile induces a nonlinear index of refraction in the material. (b) The material acts like an effective lens and tend to bring the beam to a focus at z_{sf} .

In the absence of self-focusing, a beam with finite cross section will also diffract [3, 4]. Only when self-focusing is stronger than diffraction does the beam self-focus. Consider the case when diffraction exactly balances self-focusing [3]. For the purpose of simplification, let us look at a laser beam with a flattop intensity distribution (Figure 2.2), which induces a $n_2 I$ in the middle where the beam intensity is nonzero.

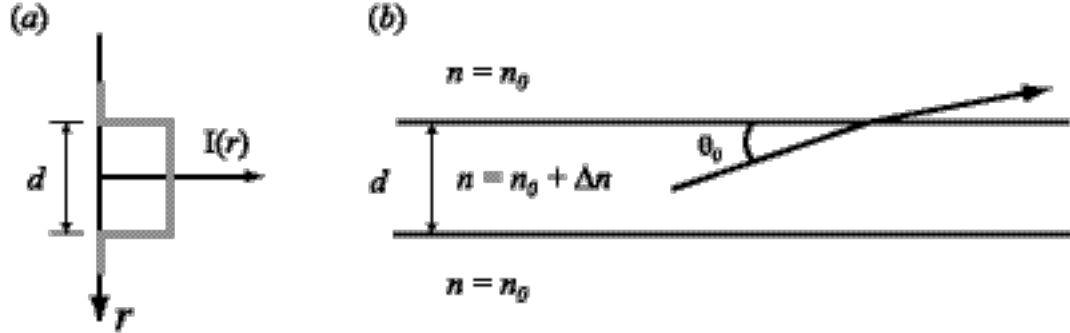


Figure 2.2 Total internal reflection in a medium at the boundary of a refractive index change produced by propagating laser beam with flat-top intensity distribution. (a) Radial intensity profile of the laser beam. (b) Indices of refraction in and outside the beam propagation region with a ray of light incident at angle θ_0 on the boundary of this refractive index change

In order for a ray to remain within the laser beam, it has to experience total internal reflection at the boundary between the two regions with different indices of refraction. Total internal reflection will occur as long as θ , measured relative to the interface, is less than the critical angle θ_0 which is determined by the indices of refraction of the two regions

$$\cos \theta_0 = \frac{n_0}{n_0 + \Delta n}. \quad (2.17)$$

Since Δn is small, equation (2.17) can be approximated by

$$\begin{aligned}
1 - \frac{1}{2} \theta_0^2 &= 1 - \frac{\Delta n}{n_0} \\
\Rightarrow \theta_0^2 &= \frac{2\Delta n}{n_0}.
\end{aligned}
\tag{2.18}$$

On the other hand, the typical magnitude of the diffraction angle of a laser beam at wavelength λ is

$$\theta_d = \frac{0.61\lambda}{n_0 d}. \tag{2.19}$$

Comparing equations (2.18) and (2.19) we notice that in order for total internal reflection, thus self-focusing to occur

$$\left(\frac{0.61\lambda}{n_0 d} \right)^2 \leq \frac{2\Delta n}{n_0}. \tag{2.20}$$

This implies

$$d^2 I \geq \frac{0.186\lambda^2}{n_0 n_2}. \tag{2.21}$$

Although the nonlinear index of refraction is an intensity dependent phenomenon, it appears that self-focusing exhibits a power threshold P_{crit} (*i. e.* $d^2 I$) instead. This critical power can be expressed as [5]

$$P_{\text{crit}} = \frac{3.77\lambda_0^2}{8\pi n_0 n_2}, \tag{2.22}$$

where λ_0 is the incident laser wavelength. The typical values of P_{crit} for condensed matter are on the order of megawatts ($P_{\text{crit}} = 4.4$ MW for water). For a collimated CW laser beam, the resulting focus forms at a distance z_{sf} measured from the front face of the material (see Figure 2.1) [5]

$$z_{sf} = \frac{0.367ka_0^2}{\left[\left(\sqrt{\frac{P}{P_{\text{crit}}}} - 0.852 \right)^2 - 0.0219 \right]^{1/2}}, \quad (2.23)$$

where $k = 2\pi/\lambda_0$ is the wavenumber and a_0 is the input beam radius. When a focusing lens of focal length f is used, self-focusing is reinforced by the external focusing. The modified critical power P'_{crit} is [5]

$$P'_{\text{crit}} = [0.852 + 0.0219 + (0.367ka_0^2/f)^2]^2 P_{\text{crit}}. \quad (2.24)$$

The corresponding self-focusing distance z'_{sf} can be obtained by applying the lens transformation to z_{sf} in (2.22) [6, 7]

$$z'_{sf} = \frac{z_{sf}f}{z_{sf} + f}. \quad (2.25)$$

The tendency of a laser beam above critical power to contract due to self-focusing should eventually lead to a catastrophic collapse of the incident beam [5]. However, a number of mechanisms also compete with the Kerr nonlinearity. Besides diffraction, which limits the self-focal diameter to about one optical wavelength [8], the free electrons generated due to the very high laser intensity achieved at the focus (especially for short pulses) contribute negatively to the index of refraction and eventually stop self-focusing [9]. The negative contribution to the index of refraction, Δn_e , by the electrons can be estimated from the Drude model

$$\Delta n_e = - \frac{2\pi e^2 N_e}{n_0 m_e (\omega_0^2 + \nu^2)}, \quad (2.26)$$

where N_e is the electron density, and ν is the electron collision frequency. An electron plasma that has a density of $\sim 10^{17}$ to 10^{18} cm^{-3} induces enough refractive index change to cancel the Kerr effect $n_2 I$ [9, 10].

Femtosecond laser pulses have high peak power because of the short pulse duration. Since self-focusing depends on pulse power instead of intensity, even without any tight focusing femtosecond laser pulses of a few hundred of nanojoules have enough power to cause self-focusing. When studying femtosecond laser interaction, it is therefore necessary to take into consideration the effect of self-focusing.

2.2.3 Filamentation

The high intensity can be created by the self-focused laser beam at the focus can cause damage in the material. It has been observed that the propagation of powerful laser beams can produce filaments in air [11-13] and leave damage tracks in solids [14, 15]. Self-focusing is believed to be the cause of these effects. Although self-focusing of intense ultrashort laser pulses is not fully understood yet, we present two models in this section that have been applied to explain the physical processes of filamentation, the self-channeling model and the moving focus model. When we discuss our experimental results of laser tissue surgery, we will be dealing with filamentation effects again. A qualitative analysis will be provided based on one of the following models.

2.2.3.1 Self-channeling of laser beam

The self-channeling mechanism was proposed by Braun *et al.* [1] to explain the filamentation in air of powerful laser pulses. The authors suggest that as the laser beam self-focuses, a high intensity is reached which causes ionization of the medium. The laser beam is then stabilized against self-focusing due to the negative index of refraction induced by the electron plasma that defocuses the beam as discussed in the previous section. However, some theoretical calculations have demonstrated [5, 16] that self-channelled propagation is unstable under perturbations and should occur only at precisely the critical power.

2.2.3.2 The moving focus model

The moving focus model was later proposed as an alternative explanation for filamentation [17]. The laser pulse is considered to be made up of a longitudinal stack of infinitely thin transverse slices. Each slice propagates independently of the others and self-focuses according to its power. As the power of each slice varies successively along the pulse, the position of the focus moves, resulting in the so-called moving focus as illustrated in Figure 2.3. The moving focus appears as a filament.

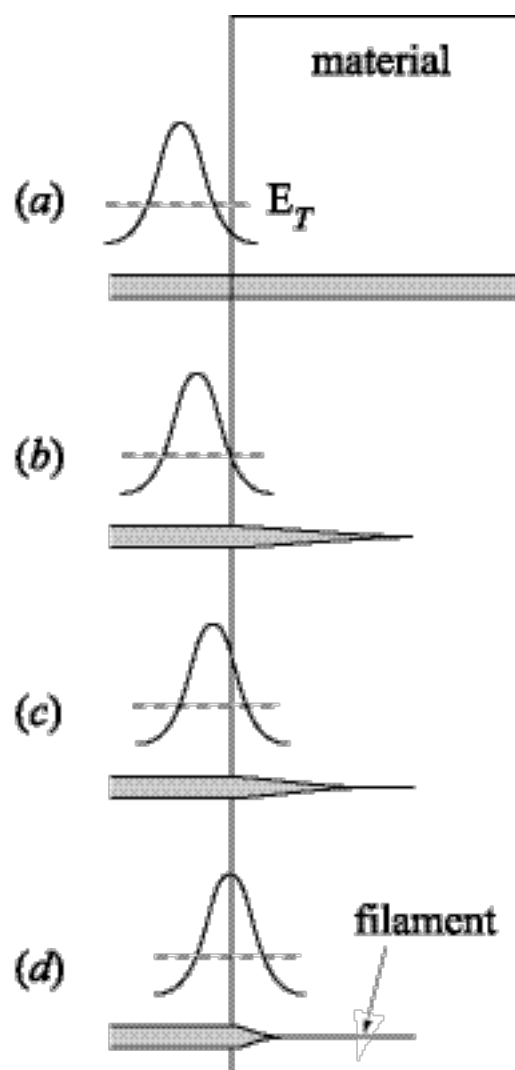


Figure 2.3 Filament formation due to self-focusing. (a) When the energy of the pulse slices inside the material is below the self-focusing threshold, the beam follows the original beam path. (b) As the energy a slice reaches the threshold, that slice self-focuses. (c) At higher energy, stronger self-focusing occurs and the focus moves closer to the surface and a filament forms. (d) When the peak of the pulse enters the material, maximal self-focusing causes the beam to focus most strongly, defining the end of the filament.

The motion of the moving foci was indeed observed experimentally using an imaging technique [15, 18]. Measurements of the energy in a filament at a point along the filament done by Brodeur *et al.* revealed that less than 7% of the total pulse energy is located within the diameter of a filament at any point [19]. This is in direct conflict with the self-channeling theory, which assumes that all of the pulse energy is trapped in the filament. The moving focus theory, on the other hand, is consistent with this observation since the energy measured from only the few slices of the pulse that self-focuses to the point where the measurement was performed.

2.3 Femtosecond laser induced optical breakdown

When the strength of the incident laser field is comparable to the Coulomb field that binds the electron to its ionic core, the electron experiences a force of similar magnitude to the atomic Coulomb force, and can be excited to a free state. Laser ionization of electrons in gases has been studied extensively, from which the basic understanding of the ionization processes were obtained [20-22]. In condensed matter, ionization and subsequent plasma formation leads to a phenomenon called optical breakdown, which can result in permanent material modification. In this section, we first review three ionization processes that can take place during optical breakdown: multiphoton, tunneling, and avalanche ionization. A discussion of material modification due to laser induced ionization and plasma generation in transparent materials will also be presented.

2.3.1 Multiphoton and tunneling ionization

Ionization in gases has been traditionally divided into two regimes, the multiphoton and tunneling regime. In the multiphoton regime, although a single photon at the laser irradiation wavelength does not have enough energy to excite the bound electron out of the Coulomb potential, a number of photons can work simultaneously to promote the bound electron to a free state as illustrated in Figure 2.4*a*. The tunneling ionization picture describes the process in which the Coulomb potential is suppressed by the strong incident field to allow the tunneling of a bound electron to a free state (see Figure 2.4*b*). The physical mechanisms that govern optical breakdown in condensed matter are basically the same as in gases. In solids, for example, the bound electron in the valence band is excited through either multiphoton or tunneling to the conduction band and becomes quasi-free.

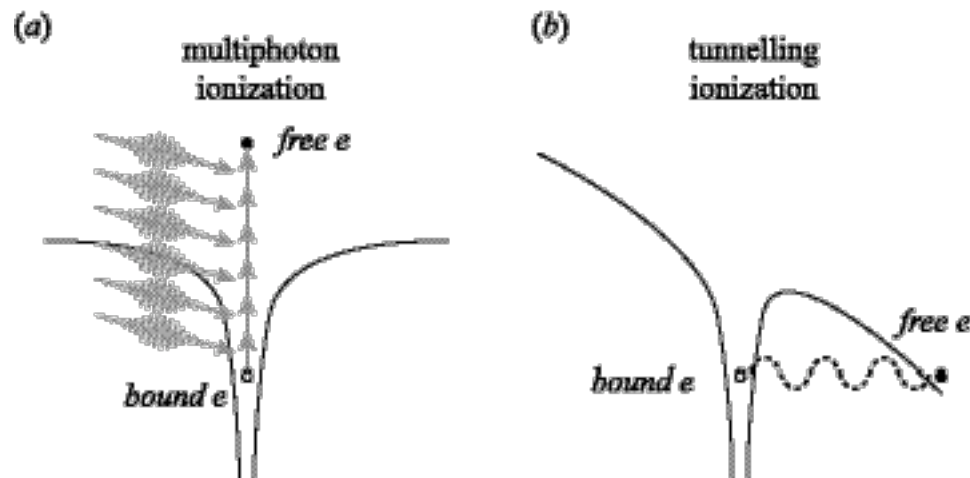


Figure 2.4 Schematic diagram that illustrates (a) multiphoton ionization and (b) tunnelling ionization of electrons by intense laser pulses.

Keldysh developed the theory that describes the ionization of electrons in condensed matter by intense laser fields [23]. Which of the two mechanisms, multiphoton

or tunneling, plays a more significant role in the ionization process in a material can be theoretically predicted using the Keldysh parameter

$$\gamma = \sqrt{\frac{m\omega_0^2 c n_0 \epsilon_0 E_{gap}}{e^2 I}}, \quad (2.27)$$

where ω_0 is the frequency of the incident laser light, m is the reduced mass of the electron, and E_{gap} is the band gap of the material. γ can be qualitatively viewed as the ratio of the incident laser frequency and field strength. For relatively weak fields with high frequencies (large γ), multiphoton ionization is more important since electrons have less time to tunnel through the only moderately suppressed Coulomb potential than in the small γ case (strong field with low frequency).

2.3.2 Avalanche ionization

In condensed matter, multiphoton or tunneling ionization alone can not explain the rapid creation of free electrons and the subsequent plasma generation responsible for optical breakdown for pulse durations greater than ~ 40 fs [24-26]. Instead, they only serve to provide the initial free electrons for the avalanche process that follows. Once created, the free electron can linearly absorb several photons from the laser field to gain enough kinetic energy and impact-ionize another bound electron by collision (Figure 2.5). The free electron plasma density increases exponentially due to this avalanche effect.

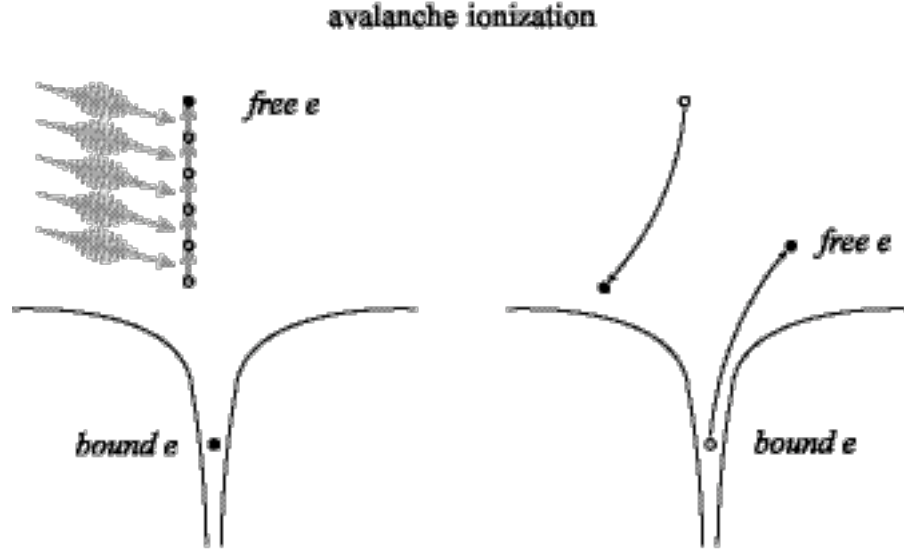


Figure 2.5 Schematic diagram of avalanche ionization in which a free electron absorbs several photons successively and impact-ionizes another bound electron.

2.3.3 Plasma absorption and material damage

As soon as the density of the plasma becomes appreciable, the incident laser light can be efficiently absorbed by electrons via free-carrier absorption. This intense heating of the electron plasma and the subsequent hydrodynamic expansion of the plasma cause permanent material modification in condensed matter.

A free electron plasma of density N has a characteristic frequency ω_p [3, 4]

$$\omega_p = \left(\frac{Ne^2}{\epsilon_0 m} \right)^{\frac{1}{2}} \quad (2.28)$$

The complex dielectric function associated with such an electron gas is

$$\epsilon(\omega) = 1 - \frac{\omega_p^2}{\omega^2(1 + i\nu/\omega)} \quad (2.29)$$

where ω_p is the incident laser frequency, and ω_p is the electron scattering frequency. The optical refractive index n is

$$n = \varepsilon^{\frac{1}{2}} = n' + i\kappa = \left(1 - \frac{\omega_p^2}{\omega^2 \left(1 + i\nu/\omega \right)} \right)^{\frac{1}{2}} \quad (2.30)$$

Separating the real and imaginary parts, we obtain

$$n' = \frac{1}{\sqrt{2}} \left[\sqrt{\left(1 - \frac{\omega_p^2}{\omega^2 + \nu^2} \right)^2 + \left(\frac{\nu}{\omega} \frac{\omega_p^2}{\omega^2 + \nu^2} \right)^2} + \left(1 - \frac{\omega_p^2}{\omega^2 + \nu^2} \right) \right]^{\frac{1}{2}} \quad (2.31)$$

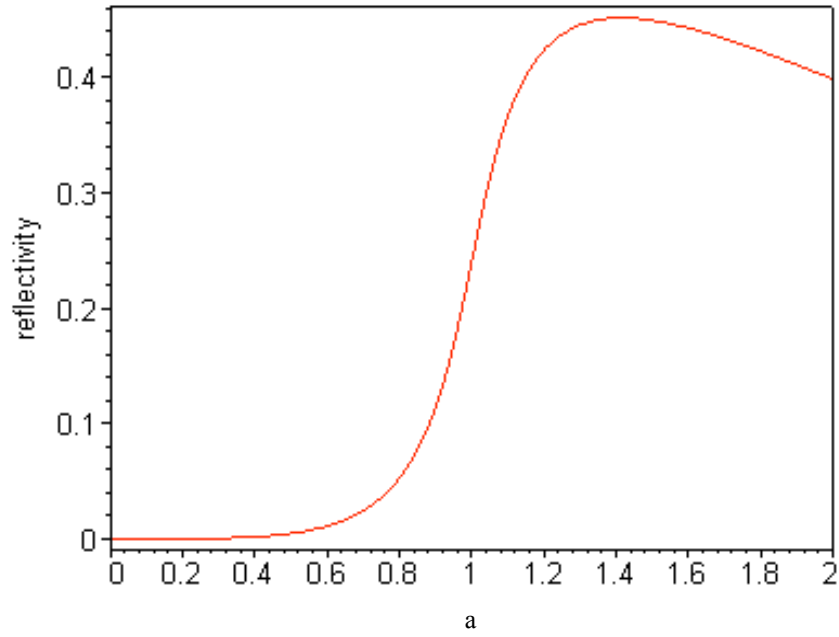
$$\kappa = \frac{1}{\sqrt{2}} \left[\sqrt{\left(1 - \frac{\omega_p^2}{\omega^2 + \nu^2} \right)^2 + \left(\frac{\nu}{\omega} \frac{\omega_p^2}{\omega^2 + \nu^2} \right)^2} - \left(1 - \frac{\omega_p^2}{\omega^2 + \nu^2} \right) \right]^{\frac{1}{2}} \quad (2.32)$$

The reflectivity of the plasma R can be expressed in terms of the refractive index. As the plasma frequency ω_p approaches the laser frequency ω (ω_p/ω approaches 1), R increases dramatically as plotted in Figure 2.6. In the limiting case, for a collisionless plasma ($\nu=0$), equation (2.29) reduces to

$$n' = \left(1 - \frac{\omega_p^2}{\omega^2} \right)^{\frac{1}{2}} \quad (2.33)$$

The index of refraction vanishes and R goes to unity when $\omega_p = \omega$, suggesting that the plasma at this density causes total reflection of the laser light. This density $N = \frac{\varepsilon_0 m \omega^2}{e^2}$

is called the critical density. For 800 nm light, the critical plasma density is $\sim 10^{21}/\text{cm}^3$.



The imaginary part of the dielectric function, κ , is a measure of the absorption of the plasma and determines the attenuation of the laser intensity at a given depth. The plasma becomes highly absorptive as the plasma frequency approaches the laser frequency. A significant fraction of the pulse energy has already been absorbed by the time the plasma density reaches the critical value [27].

2.3.4 Discussion

Optical breakdown by femtosecond laser pulses is intrinsically different from that of longer pulses. The high intensity of a femtosecond pulse guarantees the generation of seed free electrons independent of the initial electron concentration in a material, whereas impurity and defects are the source for such seed electrons for pulses longer than ~ 5 picoseconds [28]. Also, because of the short duration of the laser pulse, the energy

absorbed by the electron from the laser field does not have enough time to be transferred to the lattice. Instead, the absorbed energy efficiently heats up the electrons and also feeds the avalanche process. As a result, breakdown thresholds for femtosecond pulses are more deterministic and less influenced by the material impurity.

Energy transfer between electrons and ions happens on a much longer time scale relative to the pulse duration (on the order of picoseconds), but still before any significant thermal diffusion takes place (microseconds). The expansion of the hot plasma then follows after the energy transfer. Intense heating and rapid expansion of material in the small focal volume cause ablation on the surface of the material and vaporization in the bulk. Because of these features, the femtosecond laser is an ideal tool for highly localized material modification. In the next few chapters, we will discuss in detail how femtosecond laser induced optical breakdown can be used for precise surgery in biological tissues and manipulation of subcellular structures in living cells.

2.4 Laser systems

Recent advances in the generation and amplification of ultrashort laser pulses have made the femtosecond lasers nearly turnkey devices. A simple oscillator today produces pulses with megawatt peak power and less than 10 fs in pulse duration. Amplified femtosecond light sources routinely generate pulses with terawatt (10^{12}) peak power. Experiments presented in this study were performed primarily on a regenerative amplified femtosecond laser system. Some of the results on subcellular surgery and multiphoton

imaging were obtained using a standard femtosecond laser oscillator or a long-cavity oscillator.

2.4.1 Regenerative femtosecond laser amplifier

Most standard femtosecond laser oscillators nowadays use titanium-doped sapphire (Ti:sapphire) crystal as the active gain medium. Ti:sapphire has a wide gain bandwidth, from 700 to 1100 nm, and a very high thermal conductivity and energy storage density [29]. In addition, self-modelocking by the Kerr lens effect [29, 30] made the Ti:sapphire laser oscillator the most common ultrafast light sources. The basic cavity follows a simple X configuration (Figure 2.7a). It produces a pulse train at ~ 80 MHz repetition rate and a pulse energy of ~ 5 nJ at a central wavelength of 800 nm.

In order to achieve higher pulse energy/peak power, a second stage amplifier is needed. We use a regenerative amplifier for our study. The short pulse from an oscillator is stretched with gratings [29, 30] to picoseconds to reduce its peak power and avoid damage to the optics, and then injected into the amplifier. It completes ~ 20 roundtrips inside the cavity to gain energy before being switched out by a Pockels cell. The output pulse is then recompressed externally back to femtoseconds (using prisms or gratings). Typical output pulses from our amplifier after compression are at 1KHz repetition rate, with up to 300 μ J pulse energy and 100 fs pulse duration. A more detailed review of femtosecond laser oscillators and regens can be found in references [29, 30].

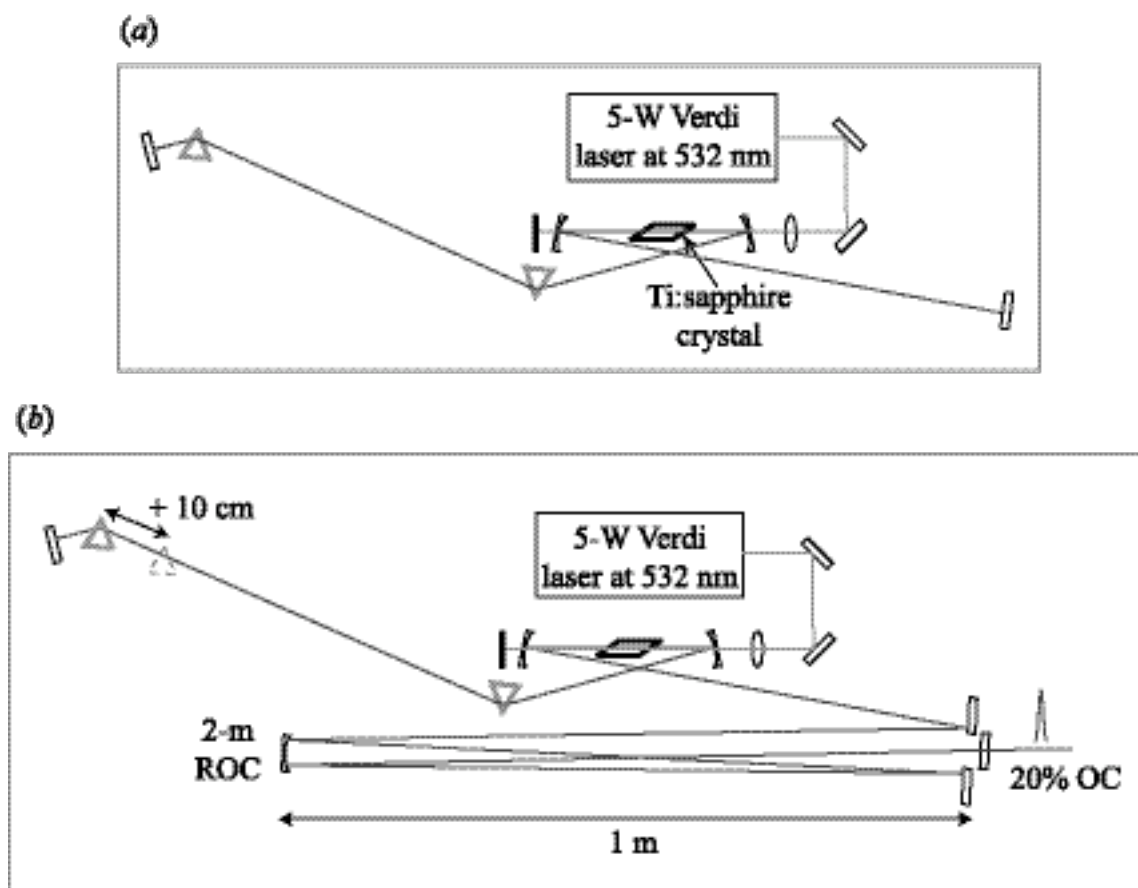


figure 2.7 Schematic diagrams of (a) standard Ti:sapphire laser oscillator with the X cavity configuration, (b) long-cavity oscillator configuration with a 20% output coupler (OC) and a 2-m radius of curvature (ROC) mirror which extends the cavity by 4 meters.

2.4.2 Long-cavity oscillator

An energy gain of $\sim 10^5$ can easily be achieved in an amplifier. However, the repetition rate of the laser has to be reduced. In some studies, it may not be necessary to have such a huge energy gain. Instead, a higher repetition rate pulse train (usually in MHz range) may be more desirable in order to induce thermal effect by depositing energy at a faster rate or to achieve real-time imaging with fast frame rate. As we will see in Chapter 4, for subcellular surgery, only a few nanojoules are needed at the sample. We therefore modified the standard Ti:sapphire femtosecond laser oscillator into a long-cavity configuration that delivers enough pulse energy for cell surgery and still maintains a high repetition rate.

The standard laser cavity is extended by 4 meters (see Figure 7*b*) by inserting a one-to-one telescope. The longer cavity length allows more gain to build up in the crystal between pulses, thus generating a higher energy per pulse. This long-cavity oscillator produces 55-fs pulses at 25-MHz repetition rate with 20 nJ/pulse. In Chapter 5, we will discuss in more detail the advantage of having a long-cavity laser for microsurgery in cells.

References

1. J. D. Jackson, *Classical Electrodynamics* (John Wiley & Sons, New York, 1975).
2. M. Born and E. Wolf, *Principles of optics* (Pergamon Press, 1980).
3. R. W. Boyd, *Nonlinear optics* (Academic Press, 1992).
4. Y. R. Shen, *The principles of nonlinear optics* (Wiley, New York, 1984).
5. J. H. Marburger, *Progress in Quantum Electronics* **4**, 35 (1975).
6. H. A. Haus, *Waves and Fields in Optoelectronics* (Prentice-Hall, Englewood Cliffs, NJ, 1984).
7. A. Yariv, *Optical Electronics* (Saunders College Publishing, Philadelphia, 1991).
8. M. D. Feit and J. A. Fleck, *Journal of the Optical Society of America B (Optical Physics)* **5**, 633 (1988).
9. E. Yablonovitch and N. Bloembergen, *Physical Review Letters* **29**, 907 (1972).
10. Y. R. Raizer, *Soviet Physics Usp* **8**, 650 (1966).
11. A. Braun, G. Korn, X. Liu, *et al.*, *Optics Letters* **20**, 73 (1995).
12. E. T. J. Nibbering, P. F. Curley, G. Grillon, *et al.*, *Optics Letters* **21**, 62 (1996).
13. A. Brodeur, in *Physics* (Laval University, Quebec, 1997), p. 166.
14. M. Hercher, *Journal of the Optical Society of America* **54**, 563 (1964).
15. Y. R. Shen, *Progress in Quantum Electronics* **4**, 35 (1985).

16. W. G. Wagner, H. A. Haus, and J. H. Marburger, *Physical Review* **175**, 256 (1968).
17. J. H. Marburger and W. G. Wagner, *IEEE Journal of Quantum Electronics* **QE-3**, 415 (1967).
18. V. V. Korobkin, A. M. Prokhorov, R. V. Serov, *et al.*, *JETP Letters* **11**, 94 (1970).
19. A. Brodeur and S. L. Chin, *Journal of the Optical Society of America B-Optical Physics* **16**, 637 (1999).
20. S. Augst, D. D. Meyerhofer, D. Strickland, *et al.*, *Journal of the Optical Society of America B: Optical Physics* **8**, 858 (1991).
21. F. A. Ilkov, J. E. Decker, and S. L. Chin, *Journal of Physics B: Atomic, Molecular and Optical Physics* **25**, 4005 (1992).
22. N. B. Delone and V. P. Krainov, *Multiphoton Processes in Atoms* (Springer-Verlag, Heidelberg, 1994).
23. L. V. Keldysh, *Soviet Physics JETP* **20**, 1307 (1965).
24. Q. Feng, J. V. Moloney, A. C. Newell, *et al.*, *IEEE Journal of Quantum Electronics* **33**, 127 (1997).
25. P. K. Kennedy, *IEEE Journal of Quantum Electronics* **31**, 2241 (1995).
26. P. K. Kennedy, S. A. Boppart, D. X. Hammer, *et al.*, *IEEE Journal of Quantum Electronics* **31**, 2250 (1995).
27. J. B. Ashcom, in *Physics* (Harvard University, Cambridge, 2002).
28. B. C. Stuart, M. D. Feit, S. Herman, *et al.*, *Physical Review B-Condensed Matter* **53**, 1749 (1996).
29. S. Backus, C. G. I. Durfee, M. M. Murnane, *et al.*, *Review of Scientific Instruments* **69**, 1207 (1998).

30. A. Rundquist, C. Durfee, Z. Chang, *et al.*, *Applied Physics B-Lasers and Optics* **B65**, 161 (1997).

Chapter 3

Femtosecond laser surgery in turbid tissue

Laser induced breakdown and damage in biological materials at the tissue level are what makes clinical laser surgery possible. In this chapter, we review laser surgery techniques presently available in the framework of turbid tissue surgery. We present a description of the current understanding of the physical events that can occur when the laser interacts with tissue, and discuss some open questions regarding the subject. We present experiments that investigate the potential of using femtosecond lasers for skin tissue surgery. Using this technique, we demonstrate the creation of incisions, surface and subsurface photodisruption cavities in skin tissues. Despite the high precision and other unique abilities femtosecond lasers exhibit when used for tissue surgery, limitations exist and will be discussed. Possible applications of femtosecond laser surgery are suggested.

3.1 Optical properties and light propagation in turbid tissues

Lasers were first used in surgical procedures in the early 1960s. Since then, there has been a growing number of medical applications for lasers first in ophthalmology, and

later in dermatology, neurology, dentistry, and other fields [1, 2]. A wide range of biological tissues is being studied in these applications. The effective use of lasers in tissue surgery requires an understanding of the fundamental interactions between the incident laser light and biological tissues. Different tissue types have different intrinsic optical properties that dictate these interactions. Choosing the right laser source for the right surgical application therefore depends on the understanding the basic laser-tissue interactions and specific tissue properties. We will be discussing mainly soft turbid tissues, skin tissue in particular, in this chapter. The structure of the skin tissue needs to be addressed before we discuss its optical properties and light-tissue interactions.

The skin is composed of two major tissue layers: the epidermis and the dermis (Figure 3.1). The epidermis is the outer layer of the skin with varying composition from the stratum corneum (the outermost layer) to the stratum germinativum (which separates the dermis from the epidermis). The stratum corneum is low in water content (approximately 10-20% by mass), and consists of cells rich in keratin, the protein which oligomerizes into tough, durable protein fibers [3]. Deeper into the skin tissue, the water content gradually increases to a maximum of 70-80% by mass. The epidermis also contains melanocytes, which are cells that produce melanin (skin pigments) and are responsible for determining the coloration of skin and hair. The dermis, lying below the epidermis, consists mainly of water and a matrix of loose connective tissue composed of fibrous proteins such as collagen, elastin, and reticulin. This matrix is traversed by a vascular network rich in hemoglobin. The dermis also houses skin appendages such as sweat glands and hair follicles [3].

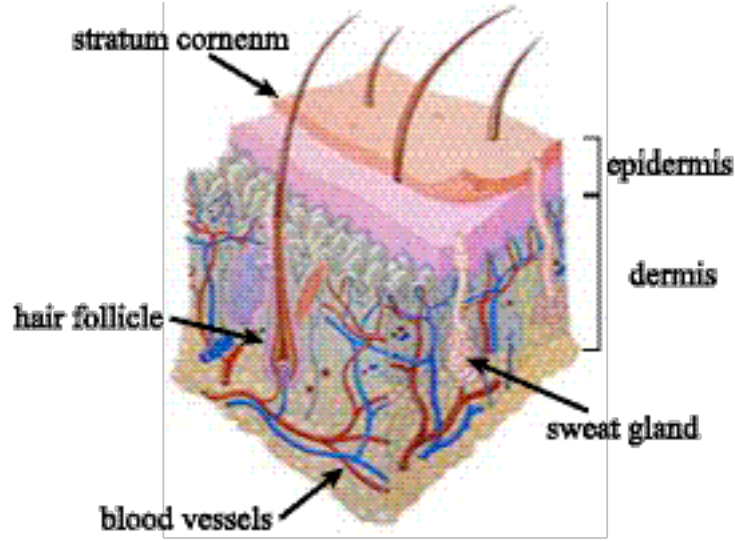


Figure 3.1 Schematic diagram of animal skin structure [3].

When skin tissue is exposed to light, three effects can occur that will perturb the photon propagation, and hence affect light-tissue interaction. They are reflection, absorption, and scattering. Only unreflected, unabsorbed or forward scattered photons are able to reach and contribute to processes occurring in the tissue layer of interest.

3.1.1 Reflection and refraction

When a beam of laser light is incident on the boundary of two different materials, a small portion of it is reflected due to the difference in indices of refraction, in our case air and the stratum corneum [4]. The reflectivity (R) is determined by the Fresnel equations and depends on the angle of incidence, light polarization, and the indices of refraction of the materials forming the boundary [5],

$$R_{//} = \left(\frac{E_r}{E_i} \right)_{//}^2 = \left[\frac{n_t \cos \theta_i - n_i \cos \theta_t}{n_i \cos \theta_t + n_t \cos \theta_i} \right]^2 \quad (3.1)$$

$$R_{\perp} = \left(\frac{E_r}{E_i} \right)_{\perp}^2 = \left[\frac{n_i \cos \theta_i - n_t \cos \theta_t}{n_i \cos \theta_i + n_t \cos \theta_t} \right]^2 \quad (3.2)$$

Here light is incident from a medium with index of refraction n_i at an angle θ_i into a medium with n_t and a angle of refraction of θ_t determined according to Snell's law. For normal incidence in air ($n = 1$) on water ($n = 1.33$), R is about 2%. In the case of skin tissue, the light reflection is diffuse rather than specular because of surface roughness. Furthermore, the reflectivity from an interface is inversely related to the interface roughness [6]. Photons reflected from a surface do not contribute to the total energy in the laser-tissue interaction that produces surgical effects. Some of the photons that do enter the tissue may also get scattered back to the tissue-air interface. If those photons strike the interface at an angle greater than the total-reflection angle, they do not exit the boundary. Instead, they tend to be trapped near the tissue surface contributing to the subsurface fluence [7-9] and make it more complex to predict energy distribution of laser light in the tissue during surgery.

3.1.2 Absorption

When the frequency of the incident light matches the natural electronic excitation frequency of a molecule, strong absorption takes place. In biological tissues, absorption is mainly caused by either water molecules or macromolecules such as proteins and pigments [4]. Absorption in the infrared region of the spectrum can be primarily attributed to water molecules, whereas proteins as well as pigments absorb more strongly in the ultraviolet and visible range. Protein, in particular, usually has an absorption peak

at about 280 nm. The typical absorption spectrum of water from UV to IR is plotted in Figure 3.2. The most important biological absorbers in skin tissues are melanin and hemoglobin [3, 4]. Melanin is the basic pigment of skin and its absorption coefficient increases monotonically as the light frequency increases from the near-IR to UV [3, 4]. On the other hand, hemoglobin has absorptions peaks around 280 nm, 420 nm, 540 nm, 560 nm, and exhibits a sharp cut-off at approximately 600 nm. The effective absorption coefficient α_a , due to all of the absorbers, determines the exponential decay rate as light propagates deeper into the tissue:

$$I = I_0 \exp(-\alpha_a z) \quad z: \text{propagation depth}$$

The typical absorption coefficient for human skin is about 2.7 cm^{-1} at 800 nm [4]. Since neither water nor macromolecules present in skin tissue absorb strongly in the near infrared range (roughly between 600 nm to 1200 nm), this spectral range is considered a “therapeutic window”. Laser radiation in this window can penetrate deeper into biological tissues with lower loss during treatment.

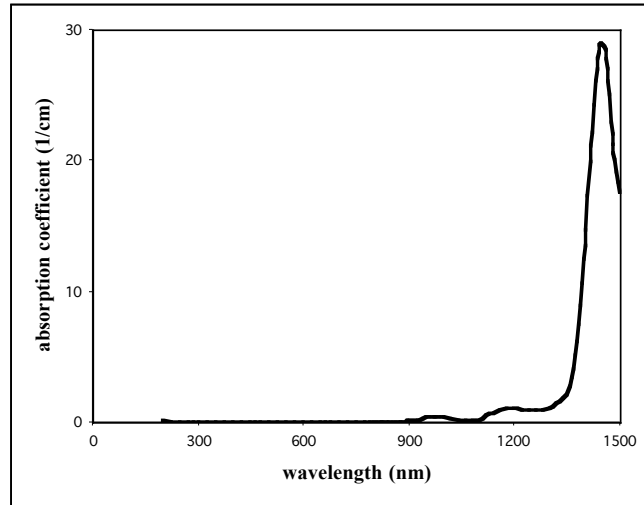


Figure 3.2 Water absorption coefficient from UV to IR.

3.1.3 Scattering

If the medium through which the light is passing has spatial or temporal variation in electromagnetic properties such as the index of refraction, some of the light is scattered. In general, the scattered photons have the same frequency as the incident photons. Their phases, on the other hand, differ, causing dispersion when penetrating into denser medium. Light scattering in tissue occurs at many levels from membranes to membrane aggregates to collagen fibers to nuclei to cells, with structure sizes varying from less than 10 nm (membrane) to over 10 μm (cell). In the limit where the scatterer is much smaller than the wavelength of the incident light, the Rayleigh scattering formalism predicts that the scattering cross section is inversely proportional to the fourth power of the wavelength [4]. When the size of the scatterer becomes comparable to the wavelength of the incident light, scattering takes place mainly in the forward direction according to Mie theory, and has a weaker dependence on wavelength compared to Rayleigh scattering [4]. Experiment has shown that, in biological tissue, scattering occurs preferably in the forward direction, which fits Mie theory [10, 11]. However, it is also observed that scattering shows a rather strong dependence on wavelength. For human skin, the measured value for the scattering coefficient is about 237 cm^{-1} with 800 nm irradiation [4].

3.1.4 Lasers for turbid tissue surgery

Both the absorption and scattering properties of a turbid tissue (*e. g.* skin) determine how photons propagate inside that medium. The total effective attenuation coefficient that measures how deep the laser light can penetrate is expressed as [4]

$$\alpha_{eff} = \frac{1}{\sqrt{3\alpha_a(\alpha_s + (1 - g))}} \quad (3.3)$$

where g is the scattering anisotropy factor which depends on the tissue type, with $g=1$ denotes perfectly forward scattering and $g=-1$ perfectly backward scattering, with g varying. The effective penetration depth of the incident light is

$$L_t = \frac{1}{\alpha_{eff}} \quad (3.4)$$

Because of tissue variation, it is difficult to determine the exact theoretical value of the scattering and absorption coefficients. Generally, in the epidermal layer of skin tissue, absorption dominates due to rich melanin content. Although the dermis also contains certain pigments such as hemoglobin, scattering has a greater effect in the dermis because of high concentrations of collagen fibers. Table 1 lists the approximate penetration depth in tissue of different wavelength taking into consideration absorption and scattering.

Table 3.1: Laser penetration depth in tissue at different wavelengths [4].

Laser Wavelength (nm)	248	514.5	830	1064	2100	2940	10600
Tissue Penetration Depth (μm)	5	330	1300	1400	400	1	20

Precise surgical effect is achieved when the right amount of laser energy is deposited (by absorption) to the right tissue target and only to the target. Understanding both the processes involved in delivering laser energy to a tissue target and the tissue properties themselves are therefore crucial in choosing laser parameters appropriate for the surgical application.

3.2 Laser-tissue surgery mechanisms

The effects light has on tissue depend not only on tissue properties but also on the characteristics of the laser source. Besides laser wavelength some of the basic parameters are power, irradiation time, and spot size for continuous wave (CW) lasers, and intensity, pulse width, repetition rate, spot size, and number of pulses for pulsed lasers. The spectrum of commercially available lasers for medical applications stretches from 193 nm to 10.6 mm. Both CW and pulse lasers with pulse durations ranging from microseconds to femtoseconds are currently available in the UV, visible, and IR range.

Ever since the first application of laser surgery in ophthalmology, lasers have been applied to a broad range of medical disciplines. Most of the applications belong to the family of minimally invasive surgery, a term that describes non-contact, bloodless surgical procedures. Despite the wide acceptance of the laser as a universal scalpel, careful studies of laser surgery are still necessary. Laser-induced effects are manifold. An effect which is essential for one treatment might be harmful for another. For instance, heating of cancerous tissue by laser irradiation could lead to desired tumor necrosis. Using the same laser parameters for retinal coagulation will burn the retina, resulting in

irreversible blindness. Understanding the mechanisms that cause laser surgical effect is therefore important for choosing the correct treatment. In the following sections we compare four different types of mechanisms that could lead to surgical effects. The four mechanisms are photochemical interaction, thermal interactions between lasers and biological material, UV laser ablation, and plasma-induced ablation and disruption.

3.2.1 Photochemical interaction

It has long been known that light can induce chemical effects in macromolecules. In current medicine, photochemical effects play a significant role in photodynamic therapy [4]. In such a therapy, special light sensitive molecules can be injected into the patient's body. Light irradiation of specific wavelength then triggers selective photochemical reactions, resulting in toxic reaction products cause irreversible destruction of target cell structure for treatment purpose. Low intensity laser light (typically 1 W/cm^2) in the visible range and long exposure times are often used to stimulate chemical reaction pathways [4]. Skin tissue surgery requires a much higher laser intensity. Hence, photochemical interactions play a less important role in determining the effect of laser irradiation on tissue. We will come back to this type of interaction again in the next chapter where the intensity of femtosecond laser pulses used to manipulate subcellular organelles is lower than when dealing with skin tissue, and so photochemical effects may be more significant.

3.2.2 Thermal interaction

Both CW and pulsed laser irradiation can cause local temperature changes in tissue producing thermal effects after photon energy has been absorbed by protein, pigment, or water molecules. Once heat is generated from absorption, it is transported to the neighboring tissue mainly through conduction. Heat convection may also occur when blood flow is significant. Different thermal effects can be achieved in biological tissues including coagulation, vaporization (of water molecules in the tissue), carbonization, and melting. Assuming a normal body temperature of 37 °C, there is no measurable physical effect in tissue with a 5 °C temperature increase. When the tissue temperature reaches 42-50 °C, hyperthermia occurs which is associated with membrane deformation and chemical bond destruction. If the temperature is elevated for more than several minutes, cells in tissue undergo necrosis. Beyond 50 °C, enzyme activity in tissue cells is reduced, energy transfer slows down, and cell repair mechanisms are disabled. At 60°C, protein denaturization occurs, leading to more immediate cell necrosis and tissue coagulation. If the tissue temperature reaches 100 °C, vaporization of water content in tissue takes place, which causes mechanical ruptures and possibly decomposition of the tissue. Above 100 °C tissue carbonizes. Melting occurs when tissue temperature rises above 300 °C. In summary, exposing tissue to temperatures above 60 °C for more than six second causes irreversible thermal damage [4]. It is therefore essential to minimize thermal effect during laser irradiation.

To determine the temperature profile of the tissue after laser irradiation, we examine the heat conduction process. Since the focus of this thesis is on femtosecond

laser interaction with biological material, we consider only the situation where laser energy is absorbed in a small focal volume, and we treat a single laser pulse as an instantaneous point source of heat. The differential heat conduction equation in spherical coordinates is [12]

$$\frac{\partial T}{\partial t} = \kappa \left(\frac{1}{r^2} \frac{\partial}{\partial r} \left(r^2 \frac{\partial T}{\partial r} \right) + \frac{1}{r^2 \sin \theta} \frac{\partial}{\partial \theta} \left(\sin \theta \frac{\partial T}{\partial \theta} \right) + \frac{1}{r^2 \sin^2 \theta} \frac{\partial^2 T}{\partial \phi^2} \right) \quad (3.4)$$

where κ is the diffusivity. Assuming a spherical symmetry in heat conduction, and a focal volume of radius a where the laser energy is absorbed, equation (3.4) can be simplified to

$$\frac{\partial u}{\partial t} = \kappa \frac{\partial^2 u}{\partial r^2}, \quad \text{where } u = Tr \text{ and } r > 0 \quad (3.5)$$

with boundary conditions

$$\begin{aligned} u &= T_0 r, & \text{when } t = 0, 0 \leq r < a \\ u &= 0, & \text{when } t = 0, r > a \end{aligned}$$

The solution of equation (3.5) is

$$T = \frac{1}{2} T_0 \left\{ \operatorname{erf} \frac{r+a}{2(\kappa t)^{\frac{1}{2}}} - \operatorname{erf} \frac{r-a}{2(\kappa t)^{\frac{1}{2}}} - \frac{2(\kappa t)^{\frac{1}{2}}}{r\pi^{\frac{1}{2}}} [e^{-(r-a)^2/4\kappa t} - e^{-(r+a)^2/4\kappa t}] \right\} \quad (3.6)$$

When a is small, the solution can be approximated as

$$T = \frac{4\pi a^3 T_0}{6(\pi \kappa t)^{\frac{3}{2}}} e^{-r^2/4\kappa t} \left\{ 1 + \left(\frac{r^2}{\kappa t} - 6 \right) \frac{a^2}{40\kappa t} \right\} \quad (3.7)$$

Figure 3.3 shows the temperature profile in water 1 ms after laser irradiation calculated according to equation (3.7), from which we can estimate the size of the thermally affected zone in skin tissue due to a 20- μ J laser pulse irradiation (with about 12 μ J reaching the focus after scattering), which is what we use in our experiments. Assuming the worst

case, where all of the absorbed energy at the focus (roughly 50% [30]) is converted to thermal energy, the resulting thermally affected zone (area where the temperature is greater than 60 °C) is $\sim 17\text{ }\mu\text{m}$. In most dermatology applications, laser pulses of energy $>10\text{ mJ}$ are used. At this energy level, the thermal damage zone can easily reach several hundred micrometers in diameter.

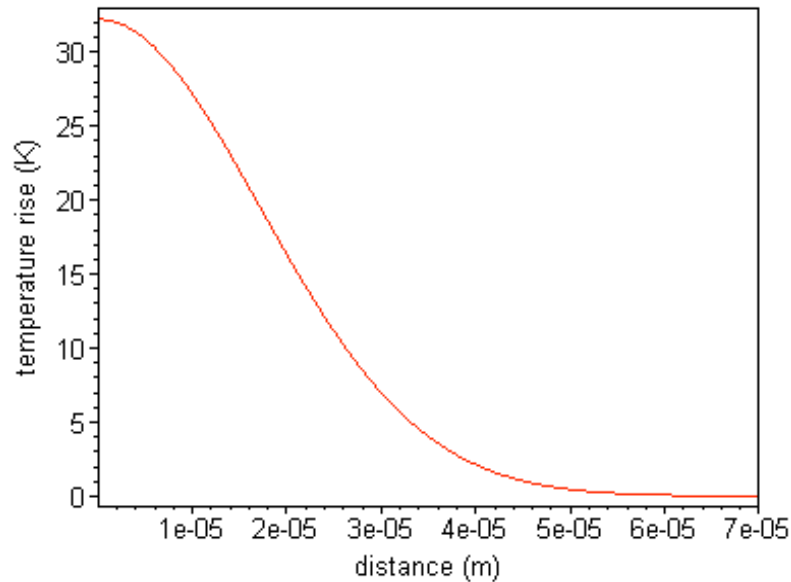


Figure 3.3 Temperature profile in water near the laser focus of a single focused 100-fs, 20-mJ pulse using a 0.6-NA objective lens.

3.2.3 UV ablation

Another type of laser tissue interaction involves UV ablation. The laser photon energy in this case exceeds many of the commonly found chemical bonds in biomolecules (Table 3.2). Once the photon energy is absorbed, it promotes the molecule to an excited state and can eventually cause dissociation of the molecules. Because the photon energy is used to break chemical bonds in this case instead of producing thermal effect, UV ablation has

high precision and generally causes little collateral damage. However, the hazard associated with UV ablation is that it is known to be harmful to cells. DNA molecules, for example, absorb strongly in the UV, which can result in mutations and lead to genetic diseases [4, 13]. Thus careful consideration needs to be given before applying UV irradiation in tissue surgery.

Table 3.2 Dissociation energy of selected chemical bonds with the corresponding wavelength [4].

Chemical bond	Dissociation energy (eV)	Wavelength (nm)
C=O	7.1	175
C=C	6.4	194
O-H	4.8	258
N-H	4.1	302
C-O	3.6	344
C-C	3.6	344
S-H	3.5	354
C-N	3.0	413
C-S	2.7	459

3.2.4 Plasma-induced ablation and disruption

When the laser intensity exceeds 10^{11} W/cm² [4], laser-induced optical breakdown occurs in biological tissue. The high concentration of photons can excite a large number of electrons in the medium and generate a plasma which causes vaporization of the material. Laser-induced plasma will then serve as an absorber of photon energy making it possible to deposit laser energy in the tissue with a low absorption coefficient. Plasma absorption is what leads to efficient tissue ablation.

When a short laser pulse (< 10 ns) is tightly focused into tissue, the laser intensity in the focal volume is high enough to induce nonlinear absorption of laser energy by the

tissue through multiphoton, tunneling, and avalanche ionization [14-21]. This nonlinear absorption produces a micrometer-sized, highly-excited plasma in the focal volume. The temperature of the laser-induced plasma can easily reach several thousand Kelvin during the duration of the pulse. The movement of these energetic free electrons in the plasma followed by the ions results in shock wave generation. The shock wave, once separated from the plasma boundary, initially travels at supersonic velocity then slows down to the speed of sound [4, 22-30]. The region of this supersonic propagation is referred to as the shock zone. Ultimately, vaporized material at the focus forms a cavitation bubble, which expands outward and then collapses under external pressure [23, 24, 27, 30, 31]. The time scale of these processes was examined by studying photodisruption events in water, and the results are plotted in Figure 3.4 [4].

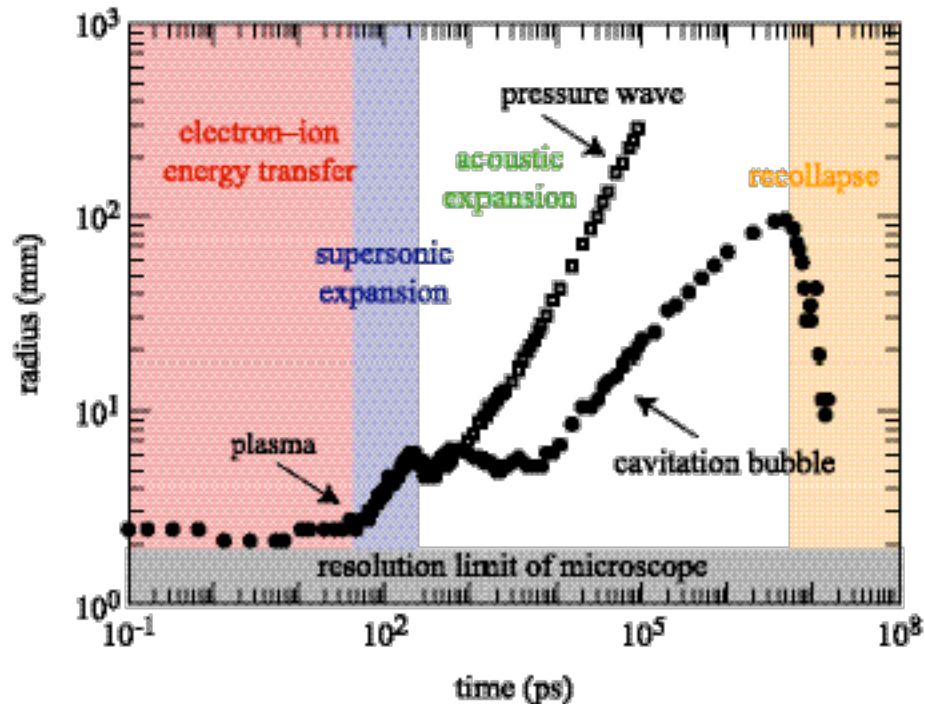


Figure 3.4 Evolution of the radius of the laser-produced plasma, pressure wave, and cavitation bubble as a function of time.

The threshold for plasma generation is generally higher for longer pulses because the intensity depends on pulse duration. There is another factor that contributes to the threshold increase in nanosecond pulses. The initiation of plasma depends on the generation of seed free electrons in the first stage before subsequent electron avalanche (see Chapter 2). For nanosecond pulses, the initial process of free electron generation is believed to be thermionic emission, where electrons are released due to thermal ionization [4, 32]. In contrast, the much higher intensity of the laser field generated by picosecond and femtosecond laser pulses can cause multiphoton ionization, which supplies the seed free electron needed to start plasma generation. As a result, a higher threshold energy is required for nanosecond laser plasma generation compared to femtosecond and picosecond lasers.

The absorption of the laser energy by the plasma, which determines the amount of energy deposition, also depends on pulse duration [33, 34]. The free-electron density, which determines the absorption coefficient, evolves over the duration of the pulse. For nanosecond pulses, the electron density reaches a peak value early in the pulse, leading to a large absorption coefficient. For picosecond pulses, maximum absorption is reached much later in the pulse, resulting in a lower average absorption coefficient. The absorption coefficient increases in the femtosecond regime due to an increased electron density earlier in the pulse. Not all absorbed energy gets converted to cause mechanical disruption however. The conversion efficiency decreases from more than 90% to about 50% as pulse duration decreases from 6 ns to 100 fs [30]. Consequently, a plasma resulting from longer pulses has a higher energy and temperature causing more mechanical disruption to tissue.

Laser-induced plasma formation vaporizes tissue in the focal volume, providing the surgical effect. However, the supersonic shock wave expansion, the expansion of the cavitation bubble, as well as heat diffusion after thermal equilibration all cause unwanted collateral damage to the surrounding tissue, limiting surgical precision [22, 29, 30, 35]. The size of the region affected by these mechanical (plasma and cavitation bubble expansion) and thermal effects depends on the amount of laser energy that is deposited into the sample. To minimize collateral damage the amount of energy deposited into the sample must be minimized while still maintaining a sufficiently high laser intensity to produce photodisruption through plasma formation.

3.3 Femtosecond laser photodisruption in skin tissue

Most surgical dermatology applications use continuous wave or pulsed lasers with a pulse duration of nanoseconds or longer [1, 4]. In these applications, laser energy is linearly absorbed by water or by natural or artificial (*e.g.*, tattoo) pigments in the skin, disrupting tissue by vaporizing tissue water content or destroying pigment molecules [4]. Because of the high laser energy and average power used in these applications, however, tissue surrounding the targeted region is affected by diffusion of thermal energy out of the target region. Furthermore, because of strong linear absorption, unwanted energy deposition can occur in any absorbing tissue outside the target region that is exposed to the laser light. Both of these effects limit the surgical precision of the procedure. Here, we investigate the possibility of using femtosecond laser pulses for precise disruption of turbid tissues such as skin.

Femtosecond pulses produce the least collateral damage in tissue compared to picosecond and nanosecond pulses. It has been reported that in corneal tissue with laser pulses that have about 3–5 times the threshold energy, the shock zone and cavitation bubble radii are 30 and 22 μm , respectively, for 150-fs laser pulses [35]. For 60-ps pulses, on the other hand, they are 100 and 130 μm , respectively [35]. In stratified human epidermis tissue (MatTek Inc.), picosecond laser pulse irradiation causes significantly more collateral damage both on the surface and inside the tissue bulk as shown in Figure 3.5 [36]. The collateral effects are even larger for the nanosecond photodisruptive lasers that are currently used in clinical applications in ophthalmology [2, 29].

Another advantage of femtosecond laser-induced photodisruption for surgical applications is the ability to work in any tissue, regardless of its absorption characteristics [37, 38]. Because infrared femtosecond laser pulses can be nonlinearly absorbed in virtually any tissue type, it is not necessary to match the laser wavelength with the absorption characteristics of the tissue or pigment as with techniques based on linear absorption [1]. In addition, even in the presence of weak linear absorption, nonlinear absorption dominates for femtosecond pulses [37]. Thus a single, near-infrared femtosecond laser system can be used to process a wide variety of tissue types and pigments.

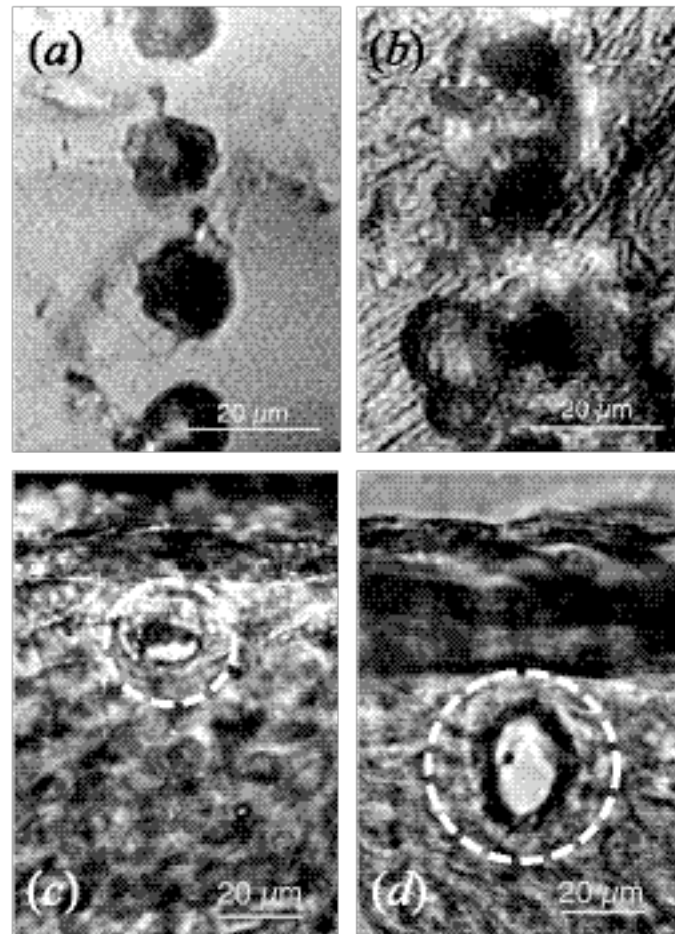


Figure 3.5 Femtosecond laser surface ablation and subsurface disruption in human skin tissue. (a) 100-fs, 40- μ J ablation spots with clearly defined crater edge. (b) 200-ps, 40- μ J ablation spots that show greater collateral damage. (c) Cross-sectional view of 100-fs, 20- μ J subsurface disruption cavity. (d) 200-ps, 20- μ J disruption cavity.

Recently, femtosecond laser pulses have been used for surface ablation of both hard (*e.g.*, teeth) [38-41] and soft (*e.g.*, cornea) [36, 37, 39, 42, 43] tissues. It is generally found that femtosecond pulses produce smoother ablation craters with less evidence of thermal and mechanical stress to the surrounding material compared to picosecond or nanosecond pulses. Producing bulk breakdown in turbid, or highly scattering, tissues is more difficult than in optically transparent tissue, such as the cornea [36, 44]. Photons scattered out of the beam path cannot participate in nonlinear absorption at the focus. As a result, higher pulse energies are required to overcome the scattering losses and reach the threshold intensity for photodisruption. This higher pulse energy, in turn, implies stronger nonlinear propagation effects in the tissue, complicating the photodisruption process. Nevertheless, many surgical procedures could benefit from the ability to disrupt the bulk of turbid tissue without affecting the surface. In dermatology, for example, if photodisruption can be achieved without rupturing the epidermis, the risk of infection is greatly reduced.

In this section, we present studies of femtosecond laser-induced photodisruption in mouse and pig skin tissues. We investigate both surface disruption and sub-surface cavity formation. We find that femtosecond laser pulses create precise incisions through different layers of skin tissue with only minimal collateral damage. We also demonstrate photodisruption of bulk skin tissue with precision at the cellular level and with no damage to the surface above the targeted region. Finally, we discuss the effects of self-focusing of intense femtosecond laser pulses in biological samples.

3.3.2 Experimental setup and procedures

All experiments were performed using a home-built amplified femtosecond Ti:Sapphire laser system delivering 100-fs pulses of 800-nm wavelength and pulse energy up to 300 μJ at a 1-kHz repetition rate. The tissue samples were mounted on an x - y translation stage. Collimated femtosecond laser pulses are focused into the tissue using a 0.6 numerical aperture (NA) microscope objective (Figure 3.6), which is secured on a separate stage allowing the laser focus to be moved in the z -direction.

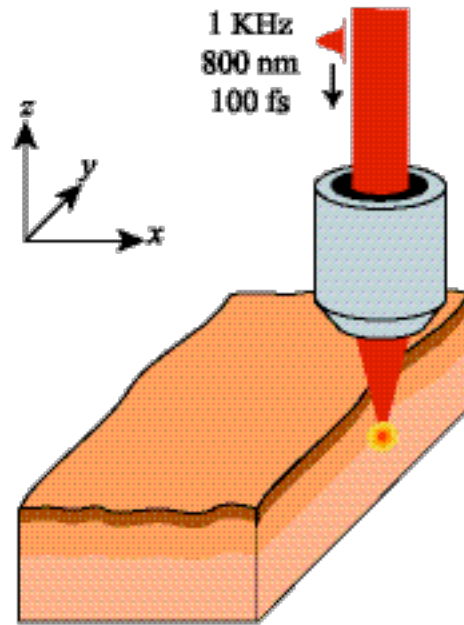


Figure 3.6 Schematic diagram of the experiments. A high numerical aperture microscope objective focuses 100-fs pulses either on the surface or into the bulk of a skin sample. The sample can be translated in the xy -plane; the objective moves along the z -direction.

To make an incision in the surface of the tissue, we focused the laser on the tissue surface and translated the sample perpendicular to the incident direction of the laser beam, while continuously irradiating with the 1-kHz pulse train. We created subsurface

cavities by focusing the laser beam at a fixed depth below the tissue surface and irradiating with the desired number of laser pulses. Parameters such as the laser energy, the sample translation speed, the depth at which the laser is focused, and the number of incident pulses were varied in our studies. For easy identification of photodisrupted regions in the sample, we produced “reference markers” using high-energy laser pulses, which create large damaged areas that can easily be located with an optical microscope. The incisions and subsurface cavities were then produced at a fixed distance of 200 mm away from the markers and from each other.

3.3.3 Sample preparation and processing experimental procedure

We investigated femtosecond laser photodisruption in fresh mouse skin and frozen pig skin. Any hair was shaved off the skin prior to use. Tissue samples were irradiated by femtosecond pulses within one hour after extraction and were kept cooled and moist in saline solution until the beginning of the experiments. The laser irradiation process takes about 10 minutes, during which the top surface of the tissue sample is exposed to air at room temperature.

Immediately after laser irradiation, the samples were fixed in Carnoy solution [45], dehydrated in a series of graded ethanol baths, and sliced into 6-mm sections using a microtome. The sample sections were stained with haematoxylin and eosin dyes and imaged under a white-light microscope [45]. Under the microscope, the nuclei appear in blue-black, the cytoplasm in varying shades of pink, and the muscle fibers in deep pinkish red. Pictures of the laser-irradiated sample slices were recorded on a digital color CCD camera.

3.3.4 Results and discussion

3.3.4.1 Precise incision

Figure 3.7 shows a cross-sectional view of an incision in mouse skin produced using 100-fs, 20- μ J laser pulses focused by a 0.6-NA microscope objective. The sample was translated along an axis perpendicular to the figure, at a speed of 5 mm/s, first with the laser focus at the tissue surface, then at 100 μ m and 200 μ m beneath the surface. The different layers visible in the image, going from top to bottom, correspond to the epidermis, the dermis, fatty tissue, and muscle cells [45]. The incision is over 100 μ m deep, reaching well into the fatty tissue layer, and is less than 5 μ m in width. The photodisrupted region is uniform and has clearly defined edges with virtually no visible collateral damage. The tissue in the surrounding area is unaffected.

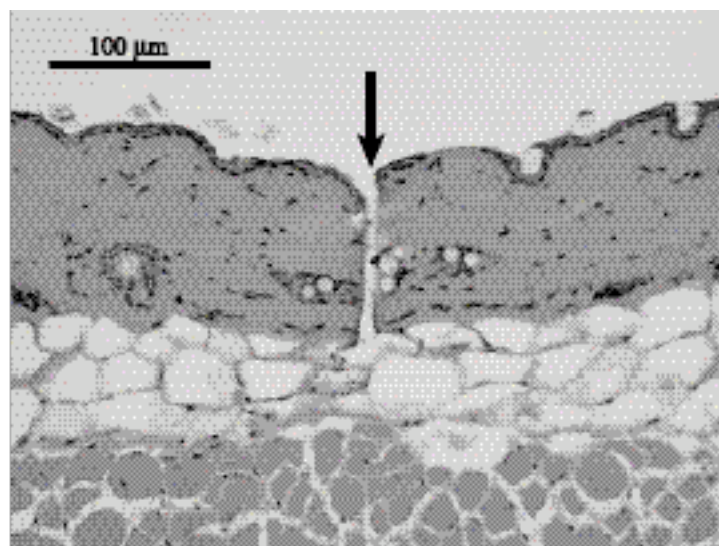


Figure 3.7 Incision in mouse skin produced by translating the sample at 5 $\mu\text{m/s}$ perpendicular to the plane of the image while continuously irradiating with a 1-kHz train of 100-fs, 20- μJ laser pulses focused by a 0.6-NA microscope objective. Three passes were made along the same line, with the laser focused first at the surface, then 100 μm , and finally 200 μm beneath the surface. The incision extends through the epidermis and dermis down into the fatty layer of the tissue.

3.3.4.2 Subsurface disruption

When focused inside the bulk of the skin rather than at the surface, femtosecond laser pulses produce small subsurface cavities. Figure 3.8 shows two such structures about 25 μm beneath the surface of mouse skin. Each of the cavities was created using a single 100-fs, 20-mJ laser pulse focused using a 0.6 NA objective. The cavities have smooth edges and show little sign of collateral damage. The diameter of these structures is about 10 μm , similar to the size of a single cell. By varying the pulse energy, the size of the sub-surface cavities can be controlled. Figure 3.9 shows that with 30 μJ of pulse energy the cavities are 40 μm in diameter, while with 5 μJ they are just 4 μm in diameter. At even lower energy the features are so small that they are likely to be altered by the sectioning and therefore difficult to observe.

In previous work, we demonstrated that in a stratified human skin model, 200-ps pulses can also produce subsurface cavities [36]. Those cavities, however, are larger in size and show significantly more collateral damage than the cavities produced by femtosecond pulses [36]. In the present study we were unable to create subsurface cavities in mouse skin with 200-ps laser pulses. Since mouse skin tissue scatters much more significantly than the stratified human skin model, pulses with higher energy have to be used to compensate for scattering loss in order to produce disruption. As a result, instead of seeing subsurface disruption, we find that the damage always extends up to the tissue surface rupturing it in the process as the laser intensity is already high before reaching the focus.

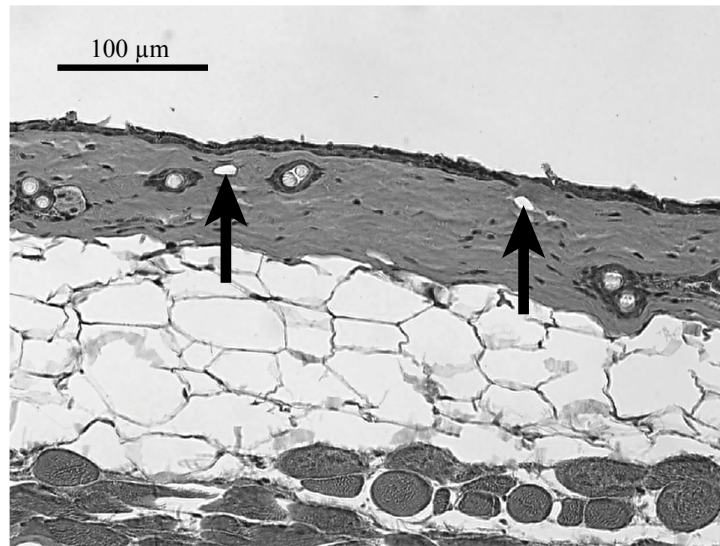


Figure 3.8 Subsurface cavities (marked by arrows), 25 μm beneath the surface of mouse skin, produced using single 100-fs, 20- μJ laser pulses focused by a 0.6-NA microscope objective. There is no observable damage to the surface of the tissue above the cavities, and collateral damage to the surrounding tissue is negligible.

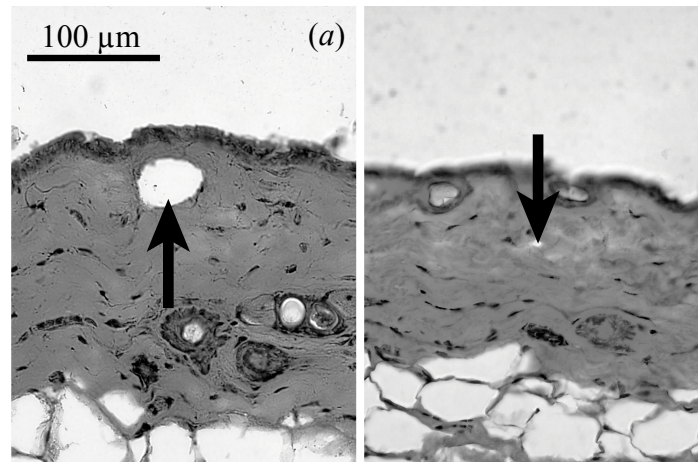


Figure 3.9 Subsurface cavities in mouse skin produced by single 100-fs pulses focused by a 0.6-NA microscope objective. The laser energies are (a) 30 μJ and (b) 5 μJ .

3.3.4.3 Subsurface filamentation and the effect of self-focusing

There is a limit to how deep beneath the surface photodisruption can be achieved in turbid tissue. In mouse skin, we were unable to create subsurface cavities deeper than about 100 μm beneath the surface using 100-fs pulses focused with a 0.60-NA objective. When the laser is focused deeper into the sample, we no longer observe well-defined subsurface cavities. Instead we see thin lines of bulk damage, tens of micrometers long that reach roughly 100 μm into the skin tissue as shown in Figure 3.10. At low pulse energies and with a low number of pulses irradiating a single spot, these structures are hard to resolve. However the lines become more pronounced when thousands of pulses are incident on a single spot (see Figure 3.11). We believe these lines of damage are the result of self-focusing of the laser pulse in the tissue.

Self-focusing results from the intensity dependence of the refractive index observed in all materials at high laser intensity [46-48]. The transverse intensity profile of the laser pulse results in a spatially-varying refractive index. As a result, the laser beam experiences an effective lens when propagating through the material, and the pulse is focused more tightly than predicted on the basis of the external focusing optics alone.

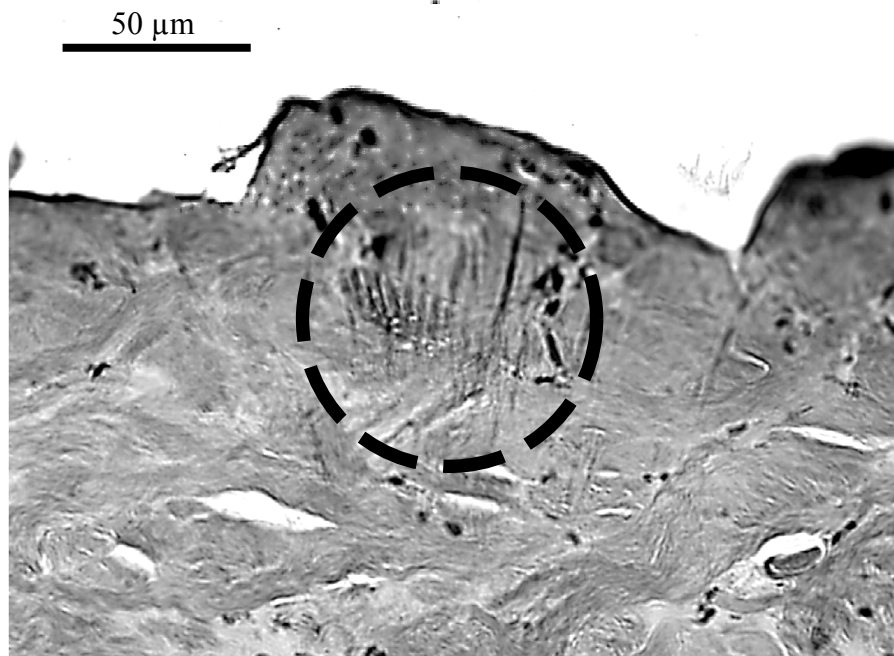


Figure 3.10 Lines of damage in pig skin produced by a single 100-fs, 30-μJ laser pulse focused by a 0.6-NA microscope objective. The laser is focused 300-μm beneath the skin surface and does not result in the formation of a subsurface cavity.

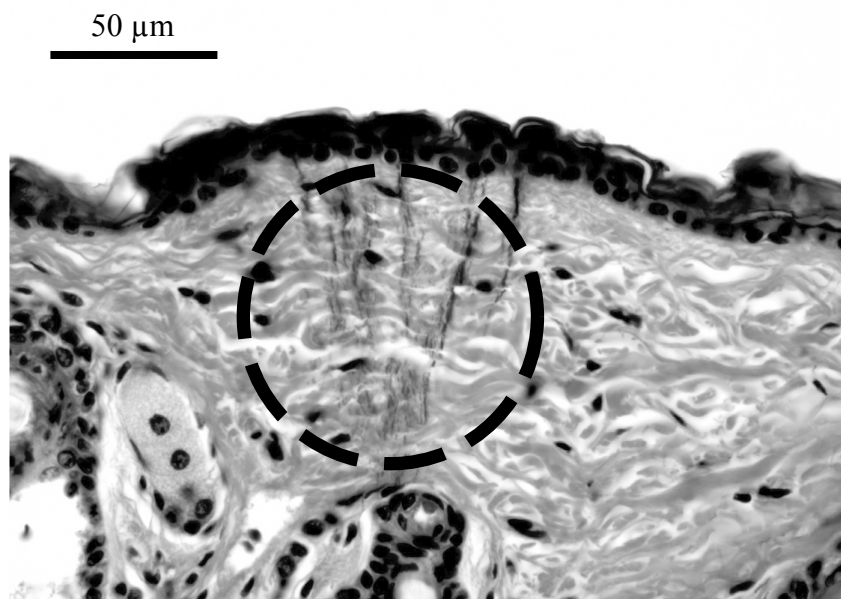


Figure 3.12 Lines of damage in mouse skin produced by 3000 100-fs, 3-μJ laser pulses focused by a 0.6-NA microscope objective. The laser is focused 300 μm beneath the skin surface.

Although the magnitude of the refractive index change is intensity-dependent, the strength of the self-focusing “lens” depends only on the laser power [46-48]. Basically, a larger diameter beam produces a longer focal-length lens than a smaller beam with the same power, but the focusing angle (the numerical aperture) is the same in both cases. The power required for a collimated laser beam to overcome diffraction and focus at infinity is called the critical power P_{crit} [46-48]. If the laser power exceeds this critical power, self-focusing effects become important [20]. The critical power depends on laser and material parameters, and is about 4.4 MW for femtosecond pulses in water [49], the main component of tissue. The peak power of the laser pulses used in our experiments exceeds this critical power by one to two orders of magnitude, and so we expect self-focusing to play an important role in the pulse propagation.

Based on the moving focus model, different temporal slices of the pulse self-focus independently of each other, with the strength of the self-focusing determined by the power in each slice [46]. The slice near the temporal peak of the pulse has the highest power, so it is focused most strongly, forming a focus the closest to the beam entrance (see Figure 2.3 in Chapter 2). The leading and trailing wings of the pulse have less power and therefore self-focus more weakly, forming a focus further away from the beam entrance. Slices in between fall somewhere in the middle and form a filament [46]. This “moving focus model” can account for the lines of tissue damage shown in Figures 3.10 and 3.11.

Because the laser intensity is high in the filament, nonlinear ionization leads to the formation of a plasma. The plasma contributes negatively to the index of refraction, counteracting self-focusing and limiting the diameter of the filament [50]. The plasma

density formed in the filament is not high enough to initiate vaporization and shock wave or cavitation bubble formation [51], but this low density plasma can still cause tissue damage via other mechanisms, such as photochemical damage to proteins or other structures in the tissue [52-56]. Because it takes about 100 μm of propagation in a material for self-focusing to form a filament, the lines of damage are only formed when the external laser focus is placed more than 100 μm into the sample [57]. Multiple lines of damage are created because the peak power of the laser exceeds the critical power by such a large factor that self-focusing causes the beam to break up spatially, with self-focusing filaments forming around higher intensity spots in the beam (either intrinsic to the laser beam or produced by refraction through the rough sample surface) [58].

The filaments in the Figures 3.10 and 3.11 appear to be roughly 50 to 100 mm long, starting near the surface and reaching as deep as ~ 120 mm into the skin tissue. We can check the experimental results against theoretical predictions. Using equations (2.22) – (2.25) in Chapter 2, we estimated the length of the filaments and how deep they will reach in skin tissue at the experimental laser and focusing conditions. Using the critical self-focusing power P_{crit} of water we find that for 100 fs, 20 mJ pulses, the resulting filaments should be about 360 mm in length and start a couple of hundred nanometers from the sample surface. The observed results are of the same order of magnitude, although the deviations are far from negligible. The discrepancy arises from the fact that skin tissue is inhomogeneous and has complex scattering and absorption properties. Further study is needed to understand the self-focusing processes in inhomogeneous materials, and to better predict the outcome for given laser and material parameters.

Our observation of collateral tissue damage due to self-focusing is of relevance to corneal refractive surgery procedures currently under development. In these procedures, femtosecond pulses are focused through up to 1 mm of corneal tissue to vaporize tissue via photodisruption [35, 59]. Because the cornea is transparent and laser energy is not lost due to scattering, the laser power necessary to induce photodisruption is lower than in turbid tissue. The typical power used in the corneal surgeries, however, still exceeds the critical power for self-focusing by almost an order of magnitude [35, 59], so self-focusing occurs and thus the importance of collateral damage to the cornea due to filaments formed by self-focusing needs to be addressed.

3.4 Conclusion

We studied photodisruption in turbid animal tissues using femtosecond laser pulses. We demonstrated that femtosecond lasers can achieve precise surgical effects both on the surface and in the bulk of turbid tissues with minimal collateral damage. When focused on the surface, these pulses produce precise, high aspect-ratio incisions in skin tissue, which may have applications for surgical incisions or for enhancing transdermal drug delivery. We also demonstrated photodisruption of bulk mouse skin, creating subsurface cavities without affecting the surface. This technique could also be used for subsurface skin surgery such as tattoo and port wine stain removal. We find that self-focusing plays an important role in photodisruption of bulk, highly scattering samples. When the laser focus is positioned more than 100 micrometers inside the skin bulk, the laser pulse produce collateral damage due to filamentation rather than subsurface cavities, placing a

limit on how deep in the bulk of turbid tissue material can be vaporized using femtosecond pulses.

References

1. C. A. Puliafito, *Laser surgery and medicine* (Wiley-Liss, Inc., New York, 1996).
2. R. F. Steinert and C. A. Puliafito, *The Nd-YAG laser in ophthalmology: principles and clinical applications of photodisruption* (Saunders, Philadelphia, 1985).
3. W. Montagna and P. F. Parakkal, *The structure and function of skin* (Academic Press, New York and London).
4. M. H. Niemz, *Laser-tissue interactions: fundamentals and applications* (Springer, Berlin; New York, 1996).
5. E. Hecht, *Optics* (Addison-Wesley Publishing Company, 1987).
6. J. F. Federici, N. Guzelsu, H. C. Lim, *et al.*, *Applied Optics* **38**, 6653 (1999).
7. M. Motamedi, S. Rastegar, G. LeCarpentier, *et al.*, *Applied Optics* **28**, 2230 (1989).
8. M. J. C. van Gemert, S. J. Jacques, H. J. C. M. Sterenborg, *et al.*, *IEEE Transactions on Biomedical Engineering* **36**, 1146 (1989).
9. B. C. Wilson and S. L. Jacques, *IEEE Journal of Quantum Electronics* **26**, 2186 (1990).
10. S. L. Jacques, C. A. Alter, and S. A. Prahl, *Lasers in Life Sciences* **1**, 309 (1987).
11. O. Parsa, S. L. Jacques, and N. S. Nishioka, *Applied Optics* **28**, 2325 (1989).
12. H. S. Carslaw and J. C. Jaeger, *Conduction of heat in solids* (Oxford University Press, London, 1959).

13. R. E. Rasmussen, M. Hammer-Wilson, and M. W. Berns, *Photochemistry and Photobiology* **49**, 413 (1989).
14. N. Bloembergen, *IEEE Journal of Quantum Electronics* **QE-10**, 375 (1974).
15. D. Du, X. Liu, G. Korn, *et al.*, *Applied Physics Letters* **64**, 3071 (1994).
16. S. C. Jones, P. Braunlich, R. T. Casper, *et al.*, *Optical Engineering* **28**, 1039 (1989).
17. M. Lenzner, L. J. Kruger, S. Sartania, *et al.*, *Physical Review Letters* **80**, 4076 (1998).
18. M. Sparks, D. L. Mills, R. Warren, *et al.*, *Physical Review B: Condensed Matter* **24**, 3519 (1981).
19. C. A. Sacchi, *Journal of the Optical Society of America B: Optical Physics* **8**, 337 (1991).
20. M. J. Soileau, W. E. Williams, N. Mansour, *et al.*, *Optical Engineering* **28**, 1133 (1989).
21. B. C. Stuart, M. D. Feit, S. Herman, *et al.*, *Physical Review B: Condensed Matter* **53**, 1749 (1996).
22. B. Zysset, J. G. Fujimoto, and T. F. Deutsch, *Applied Physics B: Photophysics and Laser Chemistry* **B48**, 139 (1989).
23. T. Juhasz, G. Kastis, C. Suarez, *et al.*, *Lasers in Surgery and Medicine* **19**, 23 (1996).
24. T. Juhasz, X. H. Hu, L. Turi, *et al.*, *Lasers in Surgery and Medicine* **15**, 91 (1994).
25. J. G. Fujimoto, W. Z. Lin, E. P. Ippen, *et al.*, *Investigative Ophthalmology and Visual Science* **26**, 1771 (1985).

26. A. G. Doukas, A. D. Zweig, J. K. Frisoli, *et al.*, *Applied Physics B: Photophysics and Laser Chemistry* **B53**, 237 (1991).
27. A. Vogel, S. Busch, and U. Parlitz, *Journal of the Acoustical Society of America* **100**, 148 (1996).
28. E. N. Glezer, C. B. Schaffer, N. Nishimura, *et al.*, *Optics Letters* **22**, 1817 (1997).
29. J. Noack, D. X. Hammer, G. D. Noojin, *et al.*, *Journal of Applied Physics* **83**, 7488 (1998).
30. A. Vogel, J. Noack, K. Nahen, *et al.*, *Applied Physics B: Lasers and Optics* **68**, 271 (1999).
31. A. Vogel, W. Hentschel, J. Holzfuss, *et al.*, *Ophthalmology* **93**, 1259 (1986).
32. C. A. Puliafito and R. F. Steinert, *IEEE Journal of Quantum Electronics* **QE-20**, 1442 (1984).
33. J. Noack, (Medical University of Lubeck, Lubeck, Germany, 1998).
34. A. Vogel, J. Noack, K. Nahen, *et al.*, in *SPIE Photonics West*, 1998, Vol. 3255, p. 34.
35. T. Juhasz, H. Frieder, R. M. Kurtz, *et al.*, *IEEE Journal of Selected Topics in Quantum Electronics* **5**, 902 (1999).
36. N. Nishimura, C. B. Schaffer, E. H. Li, *et al.*, in *Proceedings of the 20th Annual International Conference of the IEEE Engineering in Medicine and Biology Society*, 1998, Vol. 20(4), p. 1703.
37. A. A. Oraevsky, L. B. DaSilva, A. M. Rubenchik, *et al.*, *IEEE Journal of Selected Topics in Quantum Electronics* **2**, 801 (1996).
38. J. Neev, L. B. DaSilva, M. D. Feit, *et al.*, *IEEE Journal of Selected Topics in Quantum Electronics* **2**, 790 (1996).

39. F. H. Loesel, M. H. Niemz, J. F. Bille, *et al.*, *IEEE Journal of Quantum Electronics* **32**, 1717 (1996).
40. J. Neev, J. S. Nelson, M. Critelli, *et al.*, *Lasers in Surgery and Medicine* **21**, 186 (1997).
41. B. M. Kim, M. D. Feit, A. M. Rubenchik, *et al.*, *Applied Physics Letters* **76**, 4001 (2000).
42. F. H. Loesel, J. P. Fischer, M. H. Gotz, *et al.*, *Applied Physics B-Lasers and Optics* **66**, 121 (1998).
43. B. M. Kim, M. D. Feit, A. M. Rubenchik, *et al.*, *Applied Surface Science* **129**, 857 (1998).
44. N. Shen, C. B. Schaffer, D. Datta, *et al.*, in *Conference on Lasers and Electro-Optics* (Optical Society of America, Baltimore, MD, 2001), p. 403.
45. G. L. Hunason, *Animal tissue techniques* (W. H. Freeman and Company, San Francisco, 1972).
46. J. H. Marburger, *Progress in Quantum Electronics* **4**, 35 (1975).
47. Y. R. Shen, *The principles of nonlinear optics* (Wiley, New York, 1984).
48. S. A. Akhmanov, V. A. Vysloukh, and A. S. Chirkin, *Optics of femtosecond laser pulses* (Springer Verlag, New York, 1992).
49. A. Brodeur and S. L. Chin, *Physical Review Letters* **80**, 4406 (1998).
50. E. Yablonovitch and N. Bloembergen, *Physical Review Letters* **29**, 907 (1972).
51. A. L. Gaeta, *Physical Review Letters* **84**, 3582 (2000).
52. A. Vogel, J. Noack, G. Huttmann, *et al.*, in *SPIE Photonics West: Commercial and biological applications of ultrafast lasers IV*, San Jose, CA, 2002, Vol. 4633A, p. 23.

- 53. D. N. Nikogosyan, A. A. Oraevsky, and V. Rupasov, *Chemical Physics* **77**, 131 (1983).
- 54. A. Heisterkamp, T. Ripken, H. Lubatschowski, *et al.*, *Applied Physics B-Lasers and Optics* **74** (2002).
- 55. B. Boudaiffa, P. Cloutier, D. Hunting, *et al.*, *Science* **287**, 1658 (2000).
- 56. U. K. Tirlapur, K. Konig, C. Peuckert, *et al.*, *Experimental Cell Research* **263**, 88 (2001).
- 57. A. Brodeur and S. L. Chin, *Journal of the Optical Society of America B-Optical Physics* **16**, 637 (1999).
- 58. G. Fibich and B. Ilan, *Physica D* **157**, 112 (2001).
- 59. T. Juhasz, G. Djotyan, F. H. Loesel, *et al.*, *Laser Physics* **10**, 495 (2000).

Chapter 4

Disruption of subcellular organelles inside live cells

As shown in the previous chapter, the high precision that can be achieved with femtosecond lasers in tissue surgery suggests that it is possible to apply this surgical tool in cellular or even sub-cellular surgery. In this chapter, we discuss using femtosecond laser pulses to destroy discrete organelles in cells and present applications of using this technique to address biological questions.

4.1 Introduction

Complex behaviors of cells — mitosis, growth, motility, metabolism, differentiation, and apoptosis — are due to a combination of processes occurring in spatially distinct subcellular domains. To study these behaviors one needs to structurally modify or remove these functional domains within single living cells with spatial discrimination on the nanometer scale. Conventional dissection tools such as microneedles, however, are invasive, have spatial resolution limitations on the order of tens of micrometers and usually disturb the physical relationships between structures. Hence, in order to study

cellular processes, it is necessary to develop a precise subcellular surgery technique that provides submicrometer resolution, minimal alteration to cellular environment, and that can be applied to live biological samples. In this paper, we report on a novel nanosurgery technique using near-infrared femtosecond laser pulses to manipulate subcellular structures inside live cells with 300-nm resolution. Using this technique we demonstrate the cleaving of actin fiber bundles and vaporization of individual mitochondria without compromising cell viability. Our nanosurgery technique provides a direct, non-contact method for manipulating or removing individual intracellular organelles or chromosome sections in live cells. The technique opens the door to precise studies of organelle function and cellular processes by allowing observation of cell behavior after the perturbation or removal of an individual organelle.

The use of lasers in biological research and surgery has greatly increased over the past decade [1, 2]. Laser radiation affects tissue in a number of different ways: through heating, bondbreaking, and ablation or vaporization. While vaporization is limited to the focal volume, which can be made of submicrometer size, heating and indirect mechanical stresses caused by the laser excitation result in unwanted side effects on a much larger scale. Because living cells are restricted to a rather narrow range of temperatures, even relatively little heating can cause cell necrosis, limiting the total amount of energy that can be deposited in the sample. We must therefore adjust the laser parameters such that unwanted side effects are minimized.

The temperature rise in a cell due to the absorption of laser irradiation can readily be calculated. Because cells consist mainly of water, we can use measured values of the intensity threshold for laser induced plasma generation in water [3-5] to determine the

minimum energy required to cause optical breakdown in a cell under various focusing conditions and for different laser pulse durations. Using these energy values and assuming the cell to be in an aqueous medium, we numerically solved the heat diffusion equation to find the maximum temperature rise in the cell at the radius $R = 1$ mm and the radius of the volume around the focus that is transiently heated by more than 10 K (as well as the duration of this transient heating). The results for six pulse durations and four focusing conditions are summarized in Table 4.1 and Figure 4.1.

The larger the numerical aperture (NA) of the objective, the tighter the focusing is and the lower the energy required to reach the intensity threshold. Also, the shorter the pulse duration, the higher the intensity is for a given pulse energy. Therefore, the threshold intensity is reached with the least amount of energy for short pulse durations under tight focusing. This can clearly be seen in Figure 4.1, which shows that the maximum temperature just outside the focal volume is lowest for 100 fs pulses focused with a 1.4 NA objective. These pulses also minimize the time and region exposed to heating of more than 10 K (Table 1). Another important point that can be seen from Figure 1 is that the energy required for breakdown is less than 2 nJ for subpicosecond pulses, a pulse energy that can be generated without amplification, greatly simplifying the laser requirements. As the data in Table 4.1 show, for 100 fs laser pulses the increase in temperature just outside the focal volume is only 26 K. Furthermore only a 1.4 μm sized region is transiently heated by more than 10 K (for a mere 2 μs). In contrast, for pulses of longer pulse duration much larger regions are heated for significantly longer periods of time.

Table 4.1 Threshold intensities I_{th} for plasma generation in water as a function of pulse duration [3-5] corresponding energy threshold at 1.4 NA and parameters describing the resultant heating in an aqueous medium: ΔT_{max} , the peak temperature at the radius $R = 1 \text{ mm}$, R_o , the radius out to which the temperature rises by more than 10 K, and t_o , the time duration for which the temperature rise within a radius R_o is more than 10 K.

Pulse duration	$I_{th} (10^{15} \text{ W/m}^2)$	$E_{th} \text{ (nJ)}$ (1.4 NA)	$\Delta T_{max} \text{ (K)}$ ($R = 1 \text{ mm}$)	$R_o \text{ (}\mu\text{m)}$ ($T > 10 \text{ K}$)	$t_o \text{ (}\mu\text{s)}$ ($T > 10 \text{ K}$)
76 ns	0.23	1900	35000	15	260
6 ns	0.3	230	4300	7.6	65
30 ps	3.8	14	260	3.1	11
3 ps	8.5	3.8	71	1.9	4.2
300 fs	47.6	1.8	34	1.5	2.5
100 fs	111	1.4	26.5	1.4	2.1

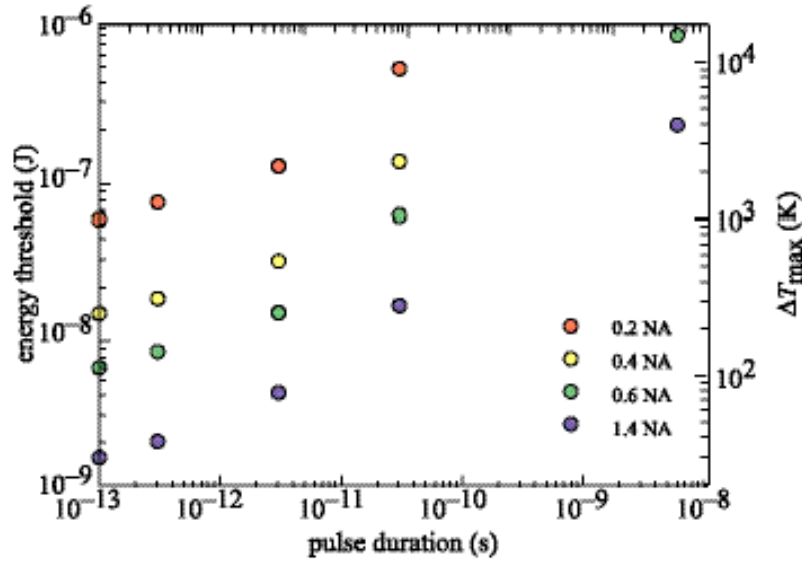


Figure 4.1 Laser pulse duration dependence of the energy threshold for laser plasma generation in an aqueous cellular medium under various focusing conditions. The corresponding maximum temperature rise at a radius of $1 \mu\text{m}$ is shown on the right hand scale.

In addition to the thermal effects caused by the laser induced plasma, we also need to consider mechanical effects on the material surrounding the focal volume. After excitation, the plasma expands supersonically into the surrounding tissue and launches a pressure wave as the laser-induced plasma expansion slows to acoustic velocity [4-10]. In addition, the vaporized material at the focus forms a cavitation bubble that expands outward and then collapses under external pressure [4, 6, 8, 11]. The size of the region affected by these mechanical effects, called the ‘shock zone’, increases with the energy deposited by the laser pulse. For 1-mJ pulses of nanosecond duration, the size of the shock zone is about half a millimeter [7]. For shorter pulse durations (and consequently lower pulses energies), the shock zone is much smaller: at 40 ps and 8 μJ it is on the order of 100 μm [7] and at 100 fs and 1 μJ it is only 11 μm [10]. For the 100-fs pulses of 2 nJ used in this paper, we estimate the shock zone to be less than 1 μm .

As the above results show collateral thermal and mechanical effects are minimized for subpicosecond pulses. When such pulses are tightly focused into biological tissue, the laser intensity at the focal volume causes nonlinear absorption of laser energy through multiphoton, tunneling, and avalanche ionization [12-16]. This nonlinear absorption produces a submicrometer-sized, highly-excited plasma, vaporizing material in the focal volume and providing the surgical effect. Because the absorption is nonlinear, laser energy is only absorbed at the focus inside the material where the laser intensity is high. So, in addition to minimizing unwanted collateral effects, subpicosecond pulses offer two additional advantages. First, they do not require any linear absorption at the laser wavelength and so any region within the medium can be targeted regardless of the wavelength of the laser. Secondly, by placing the focus beneath

the surface of the sample, material within the bulk of the sample can be vaporized, forming sub-surface cavities, without affecting the surface itself [17-24].

Figure 4.2 shows a schematic diagram of the nanosurgery setup. A femtosecond Ti:sapphire laser system delivers 100-fs pulses at 800 nm with a pulse energy of 2–5 nJ at a 1-kHz repetition rate. A mechanical shutter in the beam path allows us to control the number of pulses that irradiate the sample. The sample is mounted on a temperature-controlled stage, placed on top of a computer-controlled x - y translation stage. We focus the collimated femtosecond laser beam into the sample using a 1.4 NA oil immersion microscope objective, which is mounted on a separate stage allowing the laser focus to be moved in the z -direction. In order to monitor the sample and position the subcellular target at the focus of the femtosecond laser beam, we use the same objective to obtain an epi-fluorescence microscope image of the sample cell. The epi-fluorescence microscope allows us to observe the photodisruption in situ and to monitor the resulting cell response in real-time. We used this setup to disrupt individual actin fiber bundles and single mitochondria inside cells.

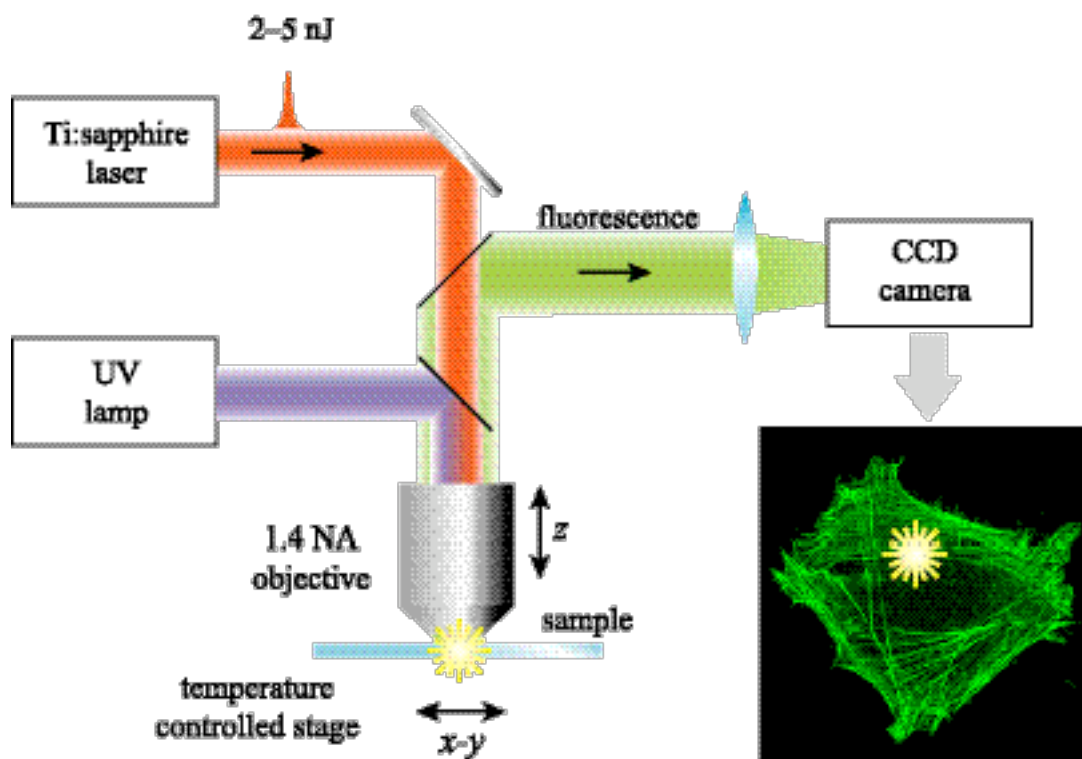


Figure 4.2 Schematic diagram of the laser cell surgery setup. Femtosecond laser pulses are focuses through a 1.4 NA oil immersion microscope objective to disrupt structures in a cell. Cell behaviors are monitored using an epi-fluorescence microscope with the same objective.

4.2 Optical imaging of cells

Optical imaging techniques enable direct visualization of sub-cellular organelles of interest, and also allow real-time observation of both morphological and biochemical responses after laser irradiation. Among some of the most widely used imaging methods in biological research, fluorescence microscopy is probably the most widely used. Although we also use other techniques such as white-light, phase contrast, and differential image contrast (DIC) in our study, only epi-fluorescent microscopy and confocal scanning microscopy will be discussed here.

4.2.1 Epi-fluorescent imaging

Fluorescence denotes the process where an electron in a molecule or atom absorbs energy (usually in the form of a photon) and is promoted from its ground to the excited state; after losing some of its vibrational energy and/or going through non-radiative conversion to a lower excited state, the electron returns to the ground state and emits a photon. The fluorescence is therefore usually red-shifted. Figure 4.3 shows the electron energy diagram of the fluorophore in this process. Because of the energy difference between the absorbed and emitted photon, background-free detection can be achieved by choosing the right combination of filters and a dichroic mirror. However, besides the obvious requirement of having the right excitation wavelength for the fluorophore, the signal in fluorescent imaging can be very low. Hence an efficient detection system is crucial to reduce signal loss.

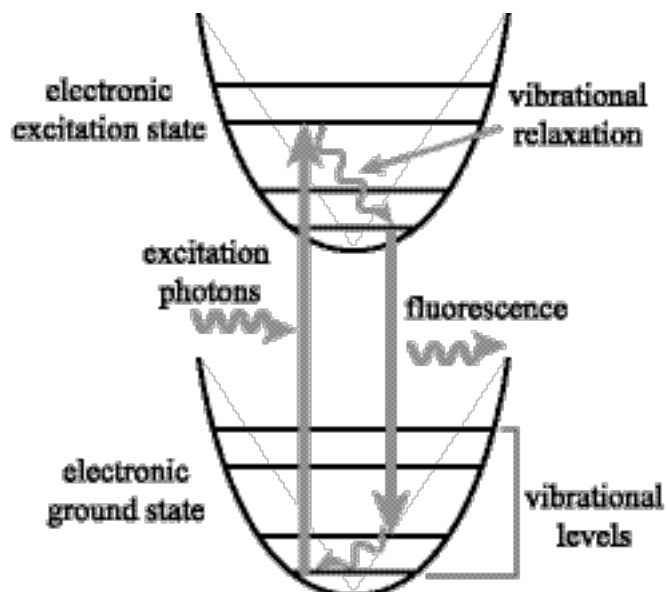


Figure 4.3 Energy diagram of the fluorescence processes. process. An electron is excited from its ground state to an excited state by absorbing a photon. A fluorescence photon is released when the electron returns to the ground state.

A fluorescent microscope consists of an excitation light source (usually an incoherent white light source such as a mercury arc lamp), focusing lens, objective lens, dichroic mirror, excitation and emission filters, and an imaging lens (for direct viewing) or a CCD camera [25]. Epi-fluorescent refers to an arrangement where fluorescently emitted photons are collected on the same side as the incident excitation light (Figure 4.2). The theoretical resolution limit of an imaging system is determined by the 3-dimensional point spread function (PSF), the intensity variation of the image of an ideal point source through a lens. Using diffraction theory, one can calculate the diffraction pattern of a point source. The resolution of an imaging system refers to the smallest separation between two points that can be resolved. It is determined by the radius of the Airy disk [26], the diffraction of a circular aperture, and can be expressed as a function of the excitation wavelength λ_0 and the numerical aperture of the focusing lens as:

$$r_{airy} = 0.61 \frac{\lambda_0}{NA} \quad (4.1)$$

where NA is defined as

$$NA = n \sin \alpha \quad (4.2)$$

and α is half of the focusing cone angle.

A fluorescent signal can be generated from certain existing molecules in cells (vitamin A, collagen fibers, chlorophylls) or from artificially introduced chemicals. The excitation and emission spectra of fluorescence in fluorescein isothiocyanate (FITC) and tetramethylrhodamine isothiocyanate (TRITC), two common chemical fluorophores for fluorescent microscopy used in biological research, are shown in Figure 4.4. There are a number of fluorescence techniques used in biology for sample preparation. We will be discussing two of them, immunofluorescence and fluorescent proteins, in more detail

later in the next section. Figure 4.5 is the epi-fluorescent microscopy image of a 3T3 fibroblast cell with actin fiber stained using Alexa Fluor 488 Phalloidin (Molecular Probes).

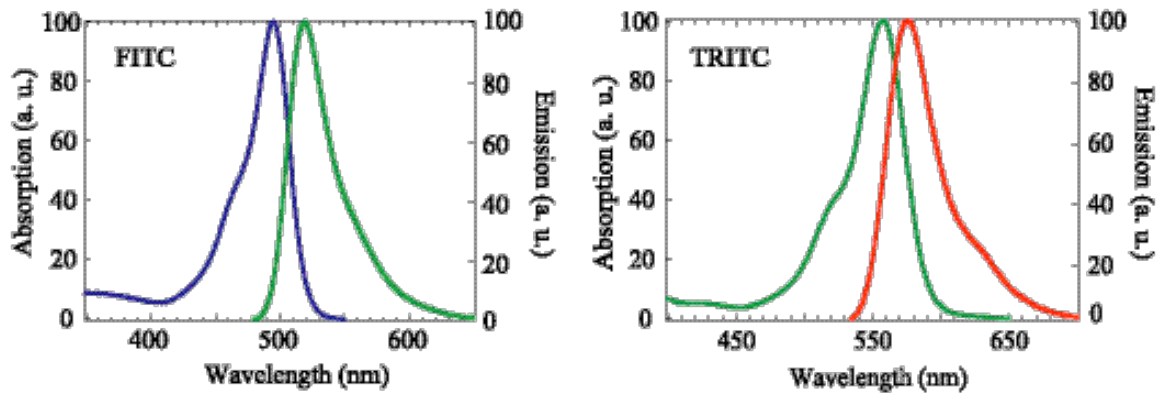


Figure 4.4 Absorption and emission spectra of fluorescein and rhodamine.

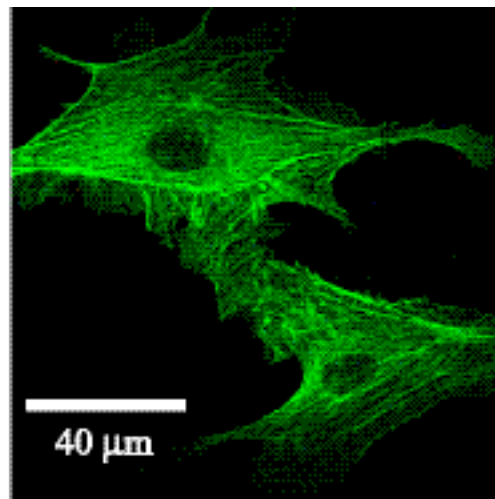


Figure 4.5 An epi-fluorescence microscope image of a 3T3 fibroblast cell with actin fibers stained with Alexa Fluor 488 phalloidin.

4.2.2 Confocal laser scanning microscopy

Confocal laser scanning microscopy exhibits a number of advantages over conventional optical microscopy. The most important feature stems from the fact that out of focus blur

due to photon scattering and fluorescence generated outside the focal plane is largely eliminated from confocal images, making direct non-invasive sectioning of fixed and live biological specimens possible. Three dimensional images of thick transparent samples such as cells and tissues can then be generated by combining the images of successive sections.

In conventional fluorescence microscopy, excitation light illuminates the entire field of view of a sample. Fluorophores throughout the depth of the sample may be excited and fluoresce. As a result, the collected signal comes from not only the focal plane, but also regions above and below, contributing to the final image as out-of-focus blur. The maximum sample thickness is about 10 μm in order to have acceptable image contrast and sharpness [25].

In order to overcome this limitation, a pinhole is placed in front of the detector in a confocal microscope, allowing only the fluorescent signal generated from one spot in the sample to pass through by spatially blocking the rest. The principle of this pinhole function is illustrated in Figure 4.6. Laser sources are often used for excitation. The laser focus is imaged as one pixel onto a two-dimensional detector array or a single photo multiplier tube. A 2-D image frame is then built pixel by pixel by scanning the laser beam. The lateral resolution limit of confocal laser scanning imaging is similar to an epi-fluorescence imaging. The axial resolution z , on the other hand, is greatly improved [25-27]

$$z \sim n\lambda/(NA)^2 \quad (4.3)$$

For a 1.4 NA oil objective, the lateral resolution is about 200 nm, and the axial resolution is roughly 400 nm.

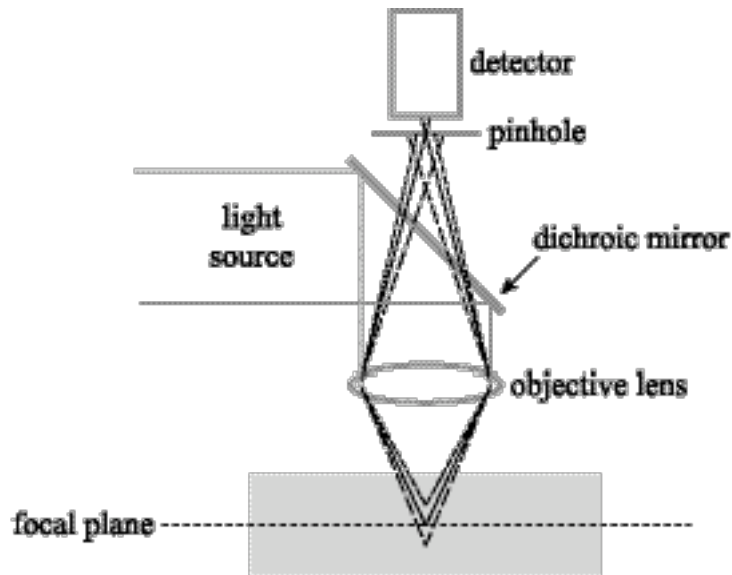


Figure 4.6 The principle function of the pinhole in a confocal microscope. Only photons generated from the focal plane of the objective lens pass through the spatial pinhole and get detected.

4.3 Fluorescence methods

Since it is necessary to identify the organelles inside cells before targeting them with femtosecond laser pulses, fluorescence staining methods with high specificity are needed. Furthermore, since cell responses are often observed over a long period of time under the fluorescence microscope, it is important to use fluorophores with a slow bleaching rate. Two methods are used to fluorescently tag specific subcellular organelles in the experiments, immunofluorescence and fluorescent proteins.

4.3.1 Immunoofluorescence

The immunofluorescence technique makes use of a specific reaction between an antibody and an antigen [27]. Antibodies are immunoglobulins that defend human or animal bodies against foreign compounds (antigens). Binding of the antibody to the antigen neutralizes the antigen. Because an antibody is only produced when the body recognizes an invading antigen, a certain antibody only interacts with a specific antigen. Furthermore, antibodies can be covalently labeled with fluorophores without inhibiting their immunological specificity, *i.e.*, biological function [27]. The immunofluorescence technique also has limitations. One is that many of the fluorophore-antibody conjugates are not permeant or have very low permeability to live cells. This means these conjugates can be used only with chemically fixed cells or cells with a compromised membrane. Another limitation comes from the fact that fluorophores tend to photobleach, which makes signal detection a challenge when experimental observation over a long period of time is required.

In fixed 3T3 fibroblast cells, we selectively label actin fibers in the cellular cytoskeleton using Alexa Fluor 488 Phalloidin or Alexa Fluor 546 Phalloidin from Molecular Probes (Figure 4.5). Phalloidin is isolated from poisonous mushrooms and binds to F-actin (filamentous actin) in the cytoskeleton. Alexa Fluor 488 and 546 have absorption and emission spectra similar to FITC and TRITC. They are also more stable to photobleaching, water soluble, pH-insensitive and have stronger absorption. We use standard FITC and TRITC filter sets (Figure 4.7) from Chroma Inc. in our fluorescence microscope.

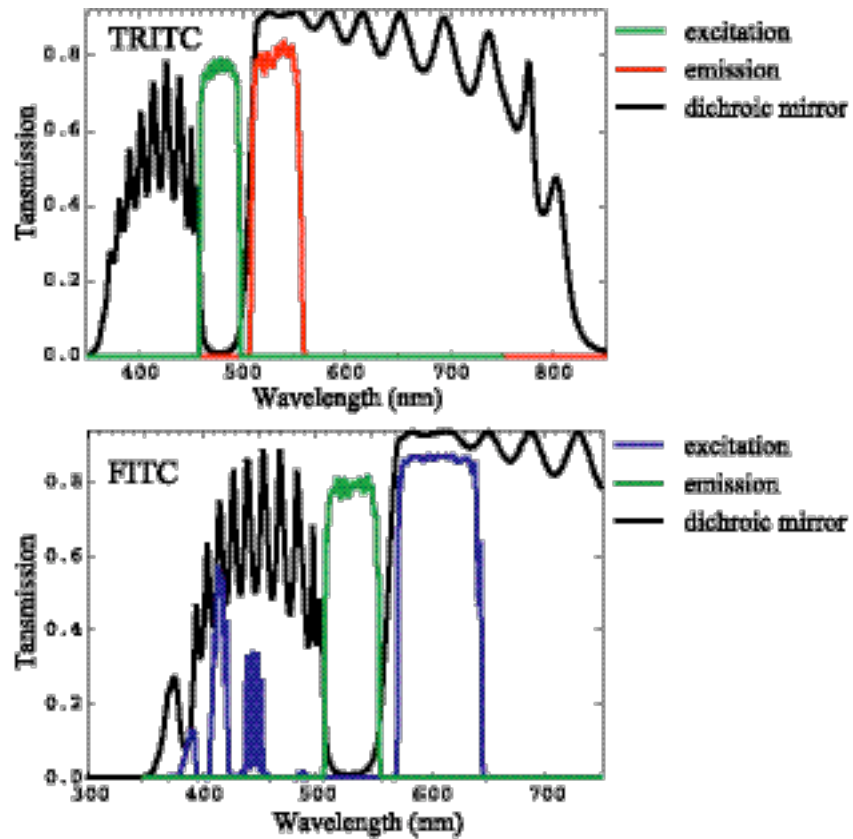


Figure 4.7 Spectra response of the components in two fluorescence microscopy filter sets used in the experiments.

4.3.2 Fluorescent protein

In order to get around the limitations that the immunofluorescence technique has with live cell samples, we selectively label subcellular organelles in live bovine capillary endothelial cells (BCE) with transfected fluorescent proteins. Figure 7 shows the image of a BCE cell with yellow fluorescent protein (YFP) transfected mitochondria.

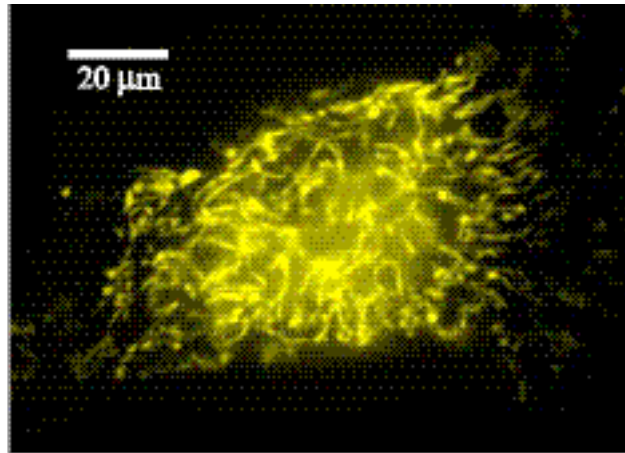


Figure 4.8 An epi-fluorescence microscope image of a bovine capillary endothelial (BCE) cell with yellow fluorescent protein (YFP) transfected mitochondria.

Green fluorescent protein (GFP) was originally discovered in jellyfish, and the biochemical and physical properties of purified GFP have been studied extensively ever since. Once the primary genetic sequence of GFP was understood, scientists were able to explore mutations in regions of the sequence adjacent to the fluorophore; this led to discovery of a number of GFP variants with brighter fluorescence or shifted absorption and emission spectra [28]. GFP and its variants have now been successfully used as specific multicolor fluorescent subcellular probes for gene expression studies, *in vivo* and *in vitro*, as tracers for cells within complex tissues, and as sensors of alterations in extracellular and intracellular micro-environments. Figure 8 shows the spectra of GFP and four other structurally engineered fluorescent proteins based on GFP.

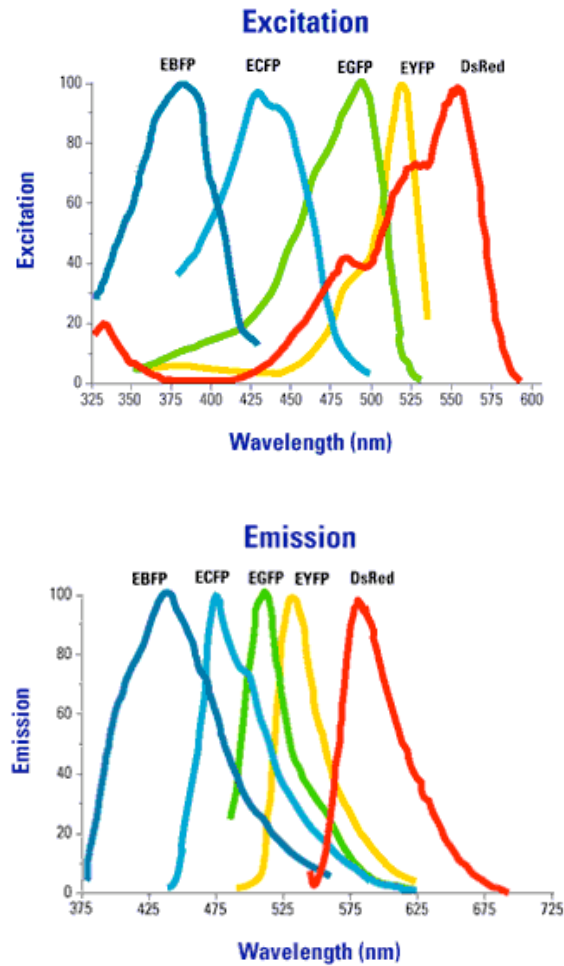


Figure 4.9 Absorption and emission spectra of fluorescent proteins.

Various strategies have been developed to optimize the expression of GFP in cells or organisms. Fusion of GFP to a protein under study was first demonstrated in 1994 [29]. The GFP gene is usually fused to the N- or C-terminus of the protein of interest, and viruses are used to deliver the fusion construct into mammalian cells, a process known as transfection [28]. The transfection of a viral vector for fluorescent protein gene transcription in cells occur rapidly, usually within 2-4 days after transfection. The level of protein expression is relatively high due to the strong viral promoter controlling the

expression of the foreign protein and active replication of the viral RNA for more templates for protein production [30].

4.4 Results and discussion

Using chemically fixed cell samples, we characterize the effects of femtosecond laser disruption in cells, and determine the energy threshold for disruption. We also target individual organelles in live cells, and observe cellular response to laser irradiation.

4.4.1 Photodisruption in fixed cells

To demonstrate the ability to locally vaporize organelles inside a cell, we first used fixed 3T3 fibroblast cells and disrupted the actin fibers in the cell cytoskeleton. Cells were cultured under 5% CO₂ on Petri dishes (Falcon) in Dulbecco's Modified Eagle's Medium (DMEM, Gibco) containing 10% fetal bovine serum, 2 mM glutamine, 100 µg/ml streptomycin, and 100 µg/ml penicillin. Cells were dissociated from culture plates with trypsin/EDTA and washed in DMEM containing 1% w/v BSA (BSA/DMEM). Before photodisruption, the cells were washed in phosphate buffered saline (PBS) with calcium, and then fixed in 4% paraformaldehyde in PBS. The cells were then permeated in wash buffer, PBS containing 0.2% Triton X-100 and 0.1% bovine serum, for 5 minutes. The cells were stained with Alexa Fluor 488 Phalloidin at a concentration of 1:100 in wash buffer for 15 minutes.

We first compare the effects of continuous wave (CW) and femtosecond laser irradiation on target cells. The unmode-locked CW laser beam from the long cavity Ti:sapphire laser system (see Chapter 2) was focused inside a fixed fibroblast cell sample for a period of 5 s. The average power of the laser beam was 75 mW. No apparent photodisruption or bleaching was detected (Figure 10a). When we mode-locked the laser at the same average power (corresponding to ~ 3 nJ/pulse), and allowed the femtosecond laser pulses to irradiate the same area in the cell, photodisruption occurred immediately (Figure 10b). This test proves the principle that energy absorption of near infrared laser radiation in biomaterials is a nonlinear process which depends strongly on laser intensity.

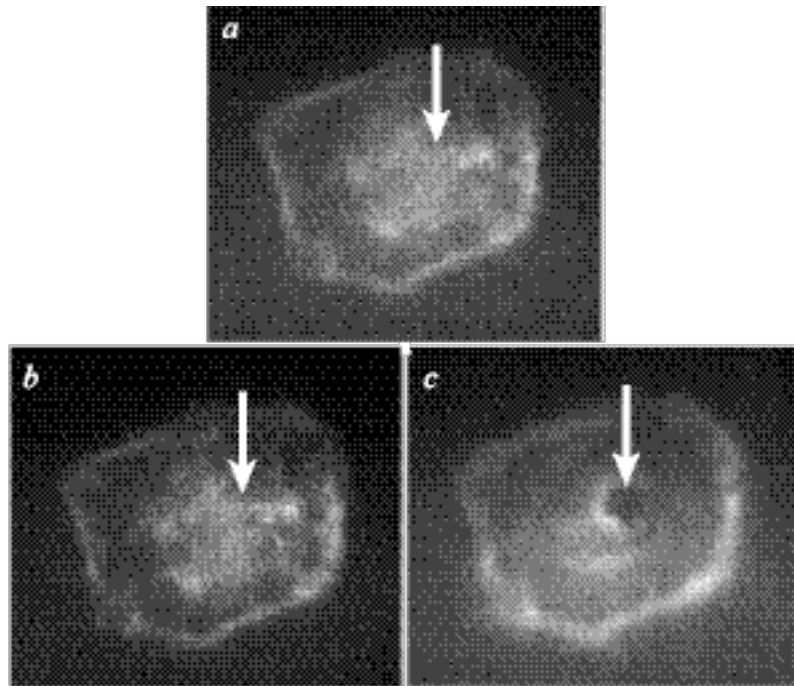


Figure 4.10 Epi-fluorescence microscope images of a 3T3 fibroblast cell (a) before laser irradiation, (b) after 800 nm CW laser irradiation, and (c) after 800 nm, 100 fs laser irradiation. Arrows indicate the position of laser focus.

The femtosecond laser pulses from the amplified Ti:Sapphire laser system were focused on target fibers inside the fixed cell and the sample was translated perpendicularly to the laser propagation direction while being continuously irradiated with the 1-kHz pulse train to cleave fibers and create channels. Cavities were produced by allowing a desired number of laser pulses to irradiate a fixed spot inside the cell, thus vaporizing materials in region roughly the same diameter as a single actin fiber bundle. Laser scanning confocal microscopy images of the cell were captured before and after laser photodisruption to characterize disruption effects. Actin fibers were cleanly severed along the path of the femtosecond laser irradiation. The varying widths of the disruption area reveal the precise control of the size of the ablated domains as the pulse energy varied from 2 to 5 nJ (Fig. 11*a*). The side view of the same cell reveals the internal control of the disruption region in the z -plane (Fig. 11*b*). The area of disruption can be confined to an interior region without affecting areas in the cell outside the focus. We also performed atomic force microscopy on another fixed 3T3 fibroblast cell, on the surface of which channels were produced using 2-nanojoule femtosecond laser pulses. The width of the channels is roughly 300 nm. Thus disruption spatial selectivity is possible inside a cell.

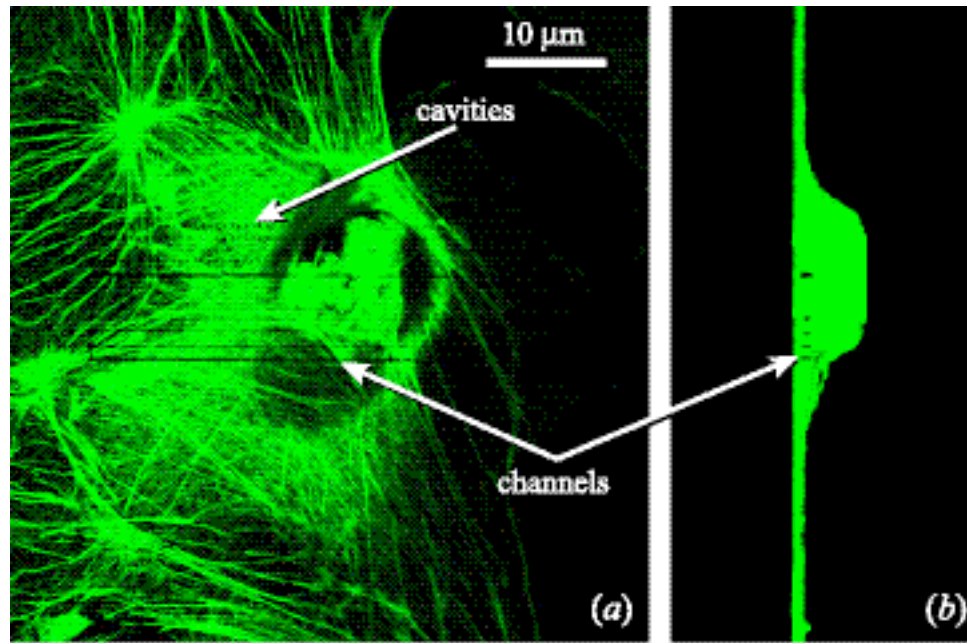


Figure 4.11 Laser scanning fluorescence confocal microscope images of a 3T3 fibroblast cell with Alexa Fluor stained actin fibers photodisrupted using femtosecond laser pulses. (a) Top view of a mid plane section through the cell in which channels and cavities were produced. (b) Reconstructed orthogonal side view image of the same cell where the spatially defined ablated regions correspond to the channels seen in (a).

We rely on fluorescent microscopy to identify laser irradiation effects, and associate the disappearance of fluorescence signal in microscopy as an indication of laser photodisruption, *i.e.*, vaporization/destruction of cellular material. However, it is important to ensure that the disappearance of fluorescence signal is not due to photobleaching of fluorophores. Photobleaching occurs when excited fluorophores undergo irreversible destruction under high-intensity illumination conditions, reducing fluorescence emission. A number of photochemical pathways have been suggested that could cause fluorophore photobleaching. They all involve the excited electron crossing from a singlet state to a triplet excited state. Hence, intense femtosecond laser pulses can cause photobleaching to the fluorophore. To pinpoint the cause of the disappearance of

fluorescent signal and verify that femtosecond laser irradiation can lead to localized vaporization/destruction of cellular material, we performed a second staining after laser irradiation with another actin-binding fluorophore, Alexa Fluor 546 Phalloidin. Alexa 546 has an emission peak in the red that can be easily distinguished from the previous stain, Alexa Fluor 488. Femtosecond laser pulses at 2 nJ (the lowest energy level used in the previous photodisruption study in fixed cells) clearly produce channels in the cell when viewed with the Alexa 488 filter set (Figure 12*a*). Although they appear to have a smaller width (Figure 12*b*), the channels nonetheless remain under the Alexa 546 filter, indicating the destruction of actin due to the femtosecond laser irradiation. As a result, it is safe to conclude that the subsurface channels and cavities we observe in fixed cells are produced by femtosecond laser disruption of cellular material.

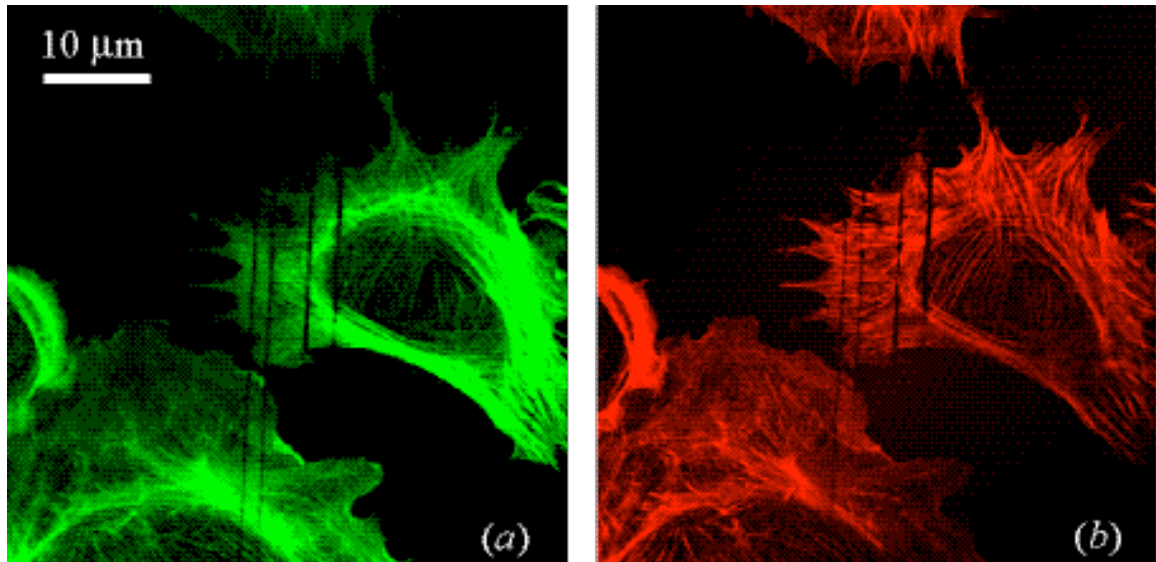


Figure 4.12 Laser scanning fluorescence confocal images a fixed 3T3 fibroblast cell taken (a) immediately after laser irradiation using a FITC filter set, (b) after restaining of the actin fibers with Alexa Fluor 546 using a TRITC filter set. The six thicker channels were produced with 5 nJ laser pulses as markers. Thinner channels were created using 2 nJ per pulse.

We also determined the femtosecond laser disruption threshold of actin fibers in cells using this method. With 1.5 nJ femtosecond laser pulses, actin fibers are cleaved

due to photodisruption in fixed fibroblast cells (Figure 13*a* and 3*b*). When we lower the laser pulse energy to 1 nJ, photobleaching effects dominate with only barely noticeable disruption remaining after the second staining. Below this energy, no photodisruption of F-actin in the cell cytoskeleton is observed, indicating that 1.5 nJ is the threshold for photodisruption of actin fibers with 100-fs, 800-nm laser pulses.

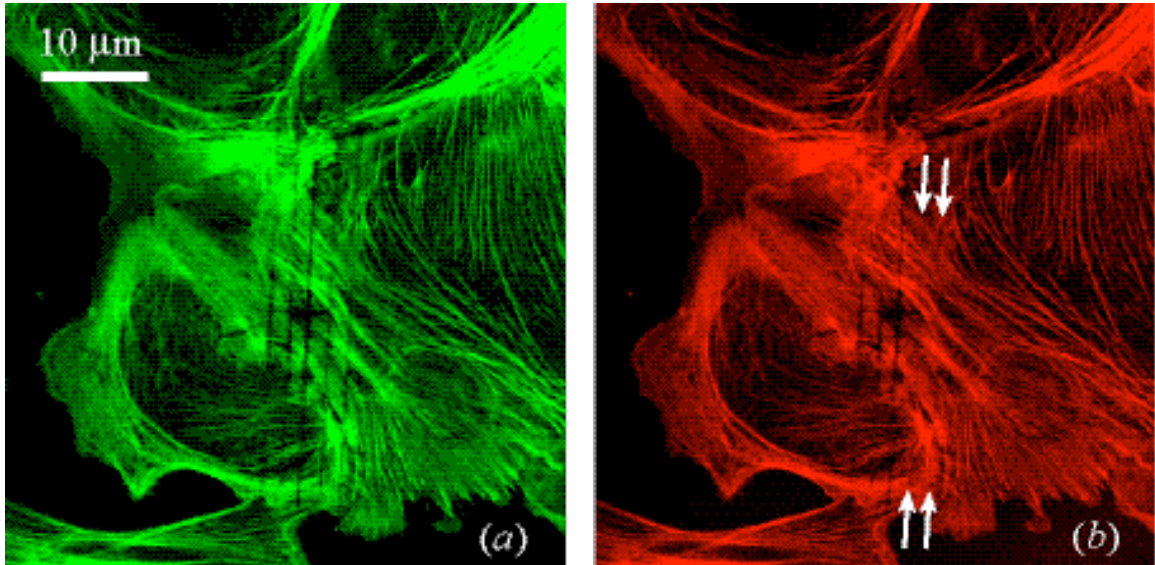


Figure 4.13 Laser scanning fluorescence confocal images a fixed 3T3 fibroblast cell taken (a) immediately after laser irradiation using a FITC filter set, (b) after restaining of the actin fibers with Alexa Fluor 546 using a TRITC filter set. The three thicker channels were produced with 5 nJ laser pulses. Thinner channels were created using 1.5 nJ per pulse energy.

4.4.2 Photodisruption in live cells

In live bovine capillary endothelial cells, we target single mitochondria with femtosecond laser pulses. BCE cells were cultured under 10% CO₂ content in standard medium (see previous section). For long-term experiments in air, cells were cultured in CO₂-independent media (Gibco) with 10 μg/ml high-density lipoprotein, 5 μg/ml transferrin, and 5 ng/ml basic fibroblast growth factor. A fusion construct containing the gene for enhanced yellow fluorescent protein (EYFP) and the mitochondrial targeting sequence

from human cytochrome C oxidase (pEYFP-Mito; Clontech) was transfected into BCE cells using the Effectene (Qiagen) technique. Single mitochondria were targeted for photodisruption. A group of mitochondria in a single cell (Figure 14a) were visualized and one was targeted with the femtosecond laser pulses of 2 nJ of energy. After the disruption, only the untargeted mitochondria remain (Figure 14b). We notice almost no structural alterations to the adjacent mitochondria separated by only hundreds of nanometers (Figure 14c). Transfected mitochondria in the cell continue to fluoresce during an observation period of one and a half hours showing no sign of morphological change to the organelles or conformational change to the protein that could lead to loss of fluorescence signal.

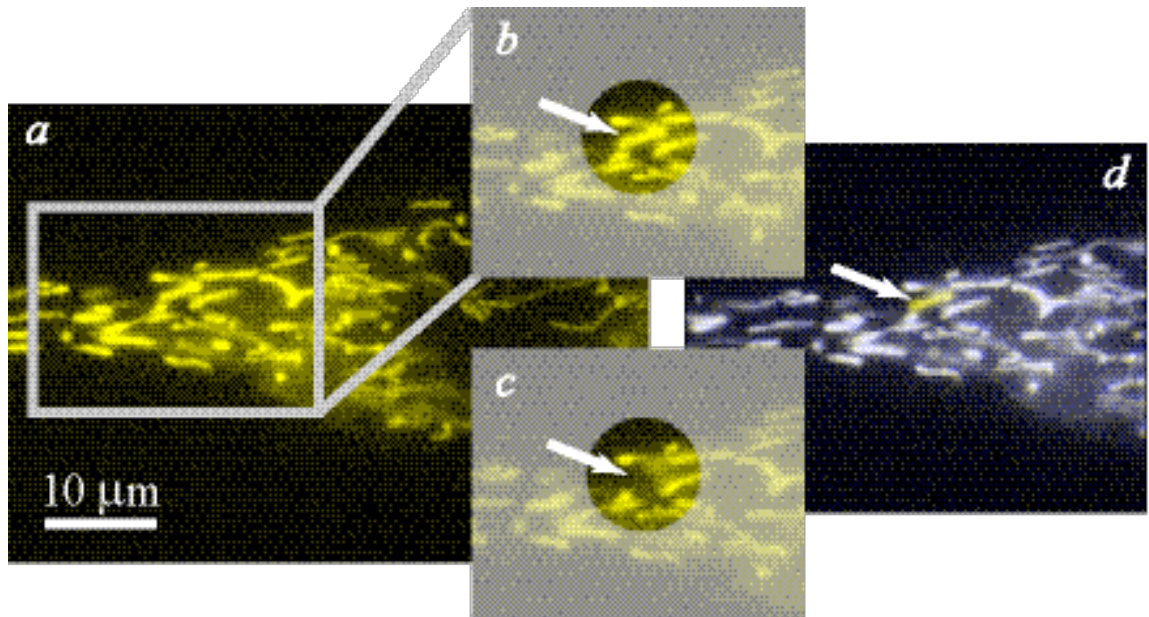


Figure 4.14 Epi-fluorescence microscope images of a BCE cell (a) before femtosecond laser irradiation with arrow indicating the target mitochondrion for disruption in (b), and (c) after 100 fs, 2 nJ laser pulse irradiation. (d) Computer generated overlay of images (b) and (c) showing a minimal effect on neighboring structures by the laser pulses.

Cell membrane integrity was tested after mitochondrion ablation to prove that photodisruption occurs inside the cell without rupturing the cell membrane. Rhodamine-

conjugated ethidium bromide, which is plasma membrane impermeable and binds to nucleic acid, was used to examine membrane integrity. Before laser irradiation, ethidium bromide (Molecular Probes) is added to the CO₂-independent cell culture media in which cells are suspended at 10 mM before laser irradiation. We selectively disrupted one mitochondrion using femtosecond laser pulses with 2 nJ of energy (Figure 15*ab*). The ethidium bromide remains on the periphery of the cell after disruption suggesting that local disruption in nanodomains of a cell does not compromise membrane integrity or lead immediately to cell necrosis. The focus of the laser pulses was then translated toward the cell membrane. When the laser focus comes into contact with the membrane, the nucleus of the cell immediately increases ten fold in fluorescent intensity as the ethidium bromide rapidly diffuses into the cell (Fig. 15*c*).

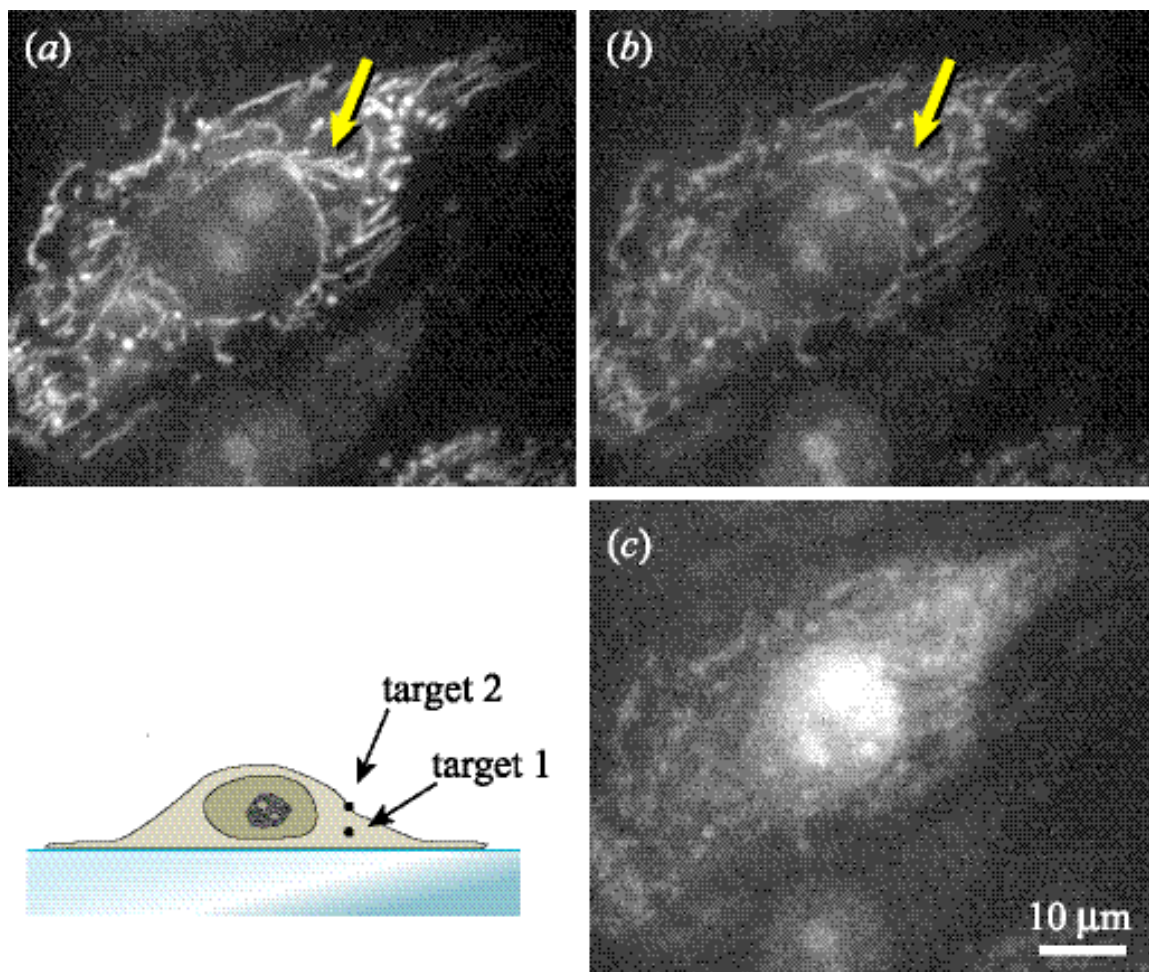


Figure 4.15 Femtosecond laser disruption of a single mitochondrion in a live BCE cell. (a) YFP-transfected mitochondria before laser irradiation. (b) Removal of the target mitochondrion indicated by the arrow (c) after laser disruption with pulses of 2 nJ of energy. Epi-fluorescence microscopy was used with TRITC filter set to capture the images.

4.4.3 Discussion

It is often believed that a critical free electron density of 10^{21} cm^{-3} has to be reached in simple materials, such as glass, before the plasma becomes dense enough to be able absorb a significant fraction of the laser energy to cause femtosecond laser-induced optical breakdown. Numerical simulation and experimental observation yield an optical breakdown intensity threshold of $\sim 10^{13} \text{ W/cm}^2$ in water for 100 fs laser pulses [5, 31].

The measured energy threshold at which we observe actin vaporization/destruction is about 1.5 nJ, corresponding to an intensity threshold of 0.9×10^{13} W/cm² assuming a diffraction-limited focus spot size. Near this threshold, we believe the shock wave propagation due to plasma expansion (the dominating mechanical effect in laser-induced material modification [8, 32]) discussed in the introduction and in the previous chapter is less important. It is simply because most of the laser pulse has just enough energy to free the bound electron during the avalanche process. These free electrons do not have enough kinetic energy to generate a significant shock wave. Hence, the high precision subcellular surgery can be achieved.

Near or below the energy level at which significant mechanical effects are achieved, photochemical effects may play an important role in determining subcellular surgery results. It has been shown that the formation of two highly reactive oxygen species OH* and H₂O₂ following ionization can lead to damage in cellular materials [33-36]. Another observation indicated that low energy electrons of less 15 eV could cause fragmentation of small molecules. Boudaiffa *et al.* [37] reported DNA strand breaking associated with low-energy electrons. Results of disruption in biomaterials using femtosecond laser pulses with energy below breakdown threshold [38] could be due to these photochemical effects.

4.5 Application: Probing mitochondrial organization in single cells

A number of existing techniques to spatially manipulate cells have subcellular resolution, but all have severe limitations. Commercially available UV microscissors use a near-

ultraviolet (337 nm) nanosecond laser pulse to dissect tissue with a resolution of about 1 μm . Because most cell components linearly absorb strongly in the near-ultraviolet, however, any components in the light path outside the focal plane also absorb the radiation, making it impossible to disrupt subcellular organelles in live cells without compromising the cell membrane. Chromophore-assisted laser inactivation (CALI) has been used in protein function studies, providing both spatial and molecular specificity [39]. A specific protein is targeted by binding a visible light absorbing dye to the protein. Upon irradiation with visible light, the dye generates free radicals that damage the bound protein. The effects of CALI, however, are short-term and recovery of protein function occurs within hours to days. In nanosecond laser microsurgery, tightly focused nanosecond laser pulses with 300–500 nJ of energy at 532-nm are used to damage subcellular structures such as the centrosome [40, 41]. The pulses do not cause physical ablation but denature the protein molecules in and around the laser focus. However, cellular structures vary in sensitivity to the nanosecond 532-nm laser irradiation and pulses that are energetic enough to affect one organelle can damage many other structures in the beam path.

The nanosurgery technique using femtosecond laser pulses presented here provides an attractive method to photodisrupt subcellular domains within live single cells with high spatial selectivity. Structures outside the small focal region remain intact, and cell viability is preserved. We believe that the technique will be useful in studies of cell dynamics, chemotaxis, cell polarity, spatially regulated signaling, drug screening and other phenomena involving intracellular compartments and sub-cellular heterogeneity. We investigated mitochondrial connectivity, to study whether these energy-generating

organelles form a physically continuous network similar to the endoplasmic reticulum or exist as independent functional units.

Recent studies of the structural organization of mitochondria and their signaling role in living cells have produced conflicting reports. Some suggest that these energy-generating organelles form a physically continuous network similar to the endoplasmic reticulum [42, 43], while others suggest that mitochondria are organized as structurally independent functional units [44, 45] that are linked by cytoskeletal filaments [46, 47]. We studied the connectivity of mitochondria by selectively damaging a single mitochondrion and examining the effect on its neighbors. If each mitochondrion is physically isolated from the others, then damage to one should not compromise the structural integrity of its neighbors.

Femtosecond laser pulses of 2 nJ energy were focused on one of a closely clustered group of mitochondria in a living bovine capillary endothelial cell (Fig. 16*a*). After damaging the target mitochondrion, only the surrounding mitochondria could be visualized (Fig. 16*b*). We carefully examined the spatial distribution of the mitochondria in the cell by overlaying cell images before and after laser irradiation. No significant alterations in the shape or position of adjacent mitochondria could be detected, even though they were separated by only hundreds of nanometers (Fig. 16*c*). We continued to observe the cell after the removal of the mitochondrion, and detect no recovery of fluorescence (Figure 16*d*) that could indicate fast protein diffusion through a tubular network. Using this approach, we conclusively demonstrate that mitochondria exist as isolated organelles within mammalian cells, thus providing direct structural evidence in support of recent physiological studies [44, 45].

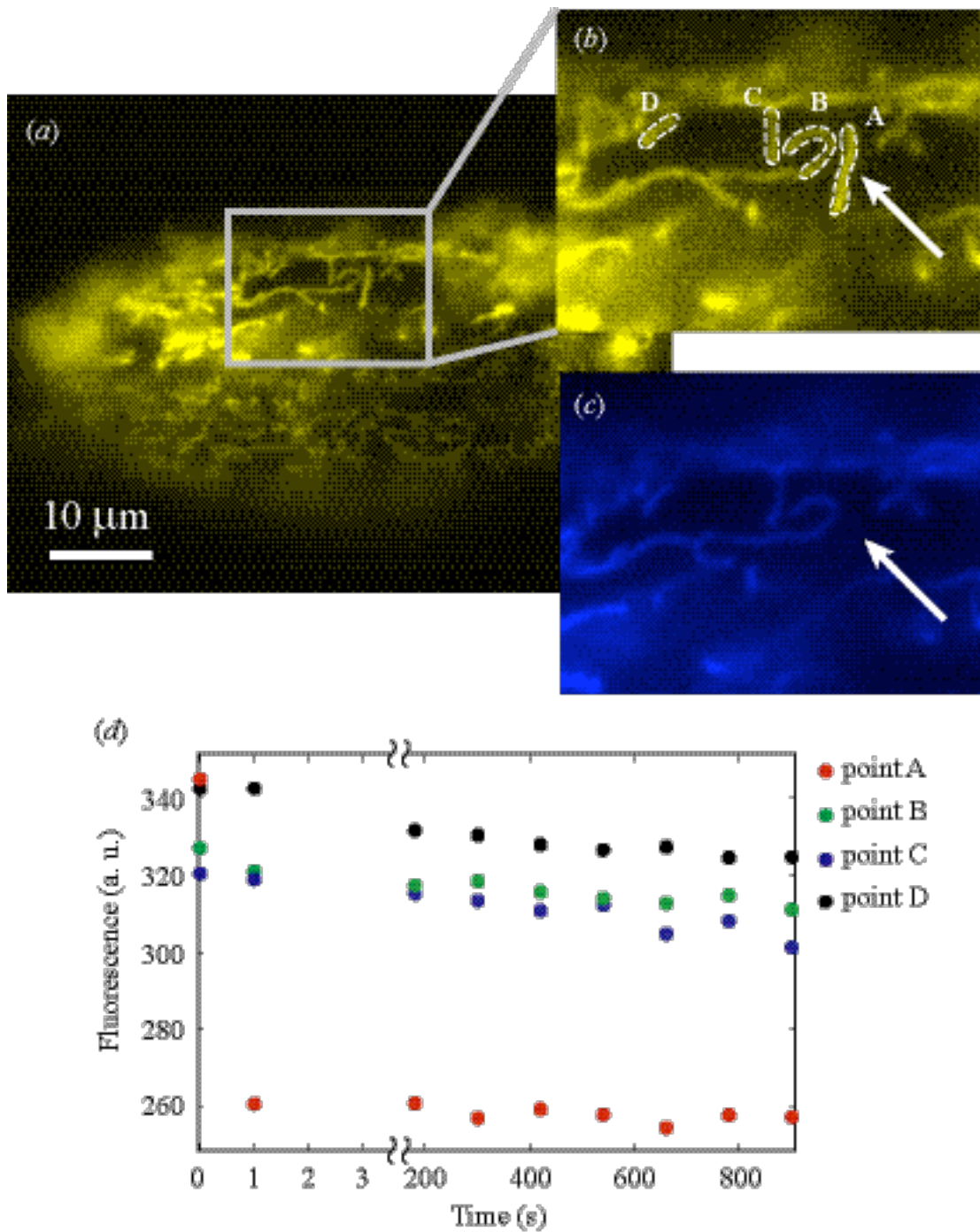


Figure 4.16 Epi-fluorescence microscope image of a live BCE cell (a) and (b) before laser irradiation, (c) after 2 nJ femtosecond laser pulses disrupted a single mitochondria at point A, and (d) measurement of fluorescence intensities at four points in the cell.

When the intensity and effective radius of irradiation are increased by using higher energy pulses at 4 nJ, the surrounding mitochondria are slightly displaced after

irradiation (Figure 17), probably due to disruption of nearby (unstained) microtubule scaffolds which orient the mitochondria [48].

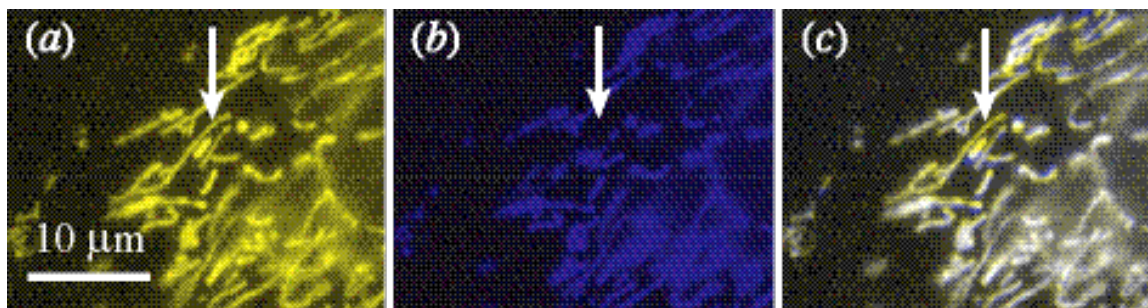


Figure 4.17 Epi-fluorescence microscope images of a BCE cell with YFP-transfected mitochondria in computer generated pseudo colors (a) before laser irradiation, (b) after laser pulses of 4 nJ irradiated a single mitochondrion indicated by the arrow, and (c) computer overlay of images (a) and (b).

4.6 Conclusion

We showed that femtosecond laser disruption provides a means to selectively vaporize, and hence physically excise molecular structures with nanometer resolution within the cytoplasm of living cells. Importantly, laser disruption of organelles within the cytoplasm does not disrupt overlying cell membranes or compromise cell viability. The femtosecond nanoscissor presented in this chapter may be useful in future studies on the role of discrete subcellular microdomains, specialized organelles, and supramolecular scaffolds in the control of complex cellular behaviors, such as growth, motility, polarity, mitosis, and spatially regulated signaling, which similarly involve contributions from multiple intracellular structural components and subcellular heterogeneity.

References

1. R. F. Steinert and C. A. Puliafito, *The Nd-YAG laser in ophthalmology: principles and clinical applications of photodisruption* (Saunders, Philadelphia, 1985).
2. C. A. Puliafito, *Laser surgery and medicine* (Wiley-Liss, Inc., New York, 1996).
3. A. Vogel, J. Noack, K. Nahen, *et al.*, in *SPIE Photonics West*, 1998, Vol. 3255, p. 34.
4. A. Vogel, S. Busch, and U. Parlitz, *Journal of the Acoustical Society of America* **100**, 148 (1996).
5. J. Noack, D. X. Hammer, G. D. Noojin, *et al.*, *Journal of Applied Physics* **83**, 7488 (1998).
6. T. Juhasz, G. Kastis, C. Suarez, *et al.*, *Lasers in Surgery and Medicine* **19**, 23 (1996).
7. J. G. Fujimoto, W. Z. Lin, E. P. Ippen, *et al.*, *Investigative Ophthalmology and Visual Science* **26**, 1771 (1985).
8. A. Vogel, J. Noack, K. Nahen, *et al.*, *Applied Physics B: Lasers and Optics* **68**, 271 (1999).
9. B. Zysset, J. G. Fujimoto, and T. F. Deutsch, *Applied Physics B: Photophysics and Laser Chemistry* **B48**, 139 (1989).
10. E. N. Glezer, C. B. Schaffer, N. Nishimura, *et al.*, *Optics Letters* **22**, 1817 (1997).
11. A. Vogel, W. Hentschel, J. Holzfuss, *et al.*, *Ophthalmology* **93**, 1259 (1986).
12. N. Bloembergen, *IEEE Journal of Quantum Electronics* **QE-10**, 375 (1974).
13. D. Du, X. Liu, G. Korn, *et al.*, *Applied Physics Letters* **64**, 3071 (1994).

14. M. Lenzner, L. J. Kruger, S. Sartania, *et al.*, *Physical Review Letters* **80**, 4076 (1998).
15. C. A. Sacchi, *Journal of the Optical Society of America B: Optical Physics* **8**, 337 (1991).
16. B. C. Stuart, M. D. Feit, S. Herman, *et al.*, *Physical Review B: Condensed Matter* **53**, 1749 (1996).
17. R. R. Krueger, A. J. Quantock, T. Juhasz, *et al.*, *Journal of Refractive Surgery* **12**, 607 (1996).
18. M. H. Niemz, T. Hoppeler, T. Juhasz, *et al.*, *Lasers and Light in Ophthalmology* **5**, 149 (1993).
19. R. M. Kurtz, X. B. Liu, V. M. Elner, *et al.*, *Journal of Refractive Surgery* **13**, 653 (1997).
20. N. Nishimura, C. B. Schaffer, E. H. Li, *et al.*, in *Proceedings of the 20th Annual International Conference of the IEEE Engineering in Medicine and Biology Society*, 1998, Vol. 20(4), p. 1703.
21. R. R. Krueger, T. Juhasz, A. Gualano, *et al.*, *Journal of Refractive Surgery* **14**, 467 (1998).
22. T. Juhasz, H. Frieder, R. M. Kurtz, *et al.*, *IEEE Journal of Selected Topics in Quantum Electronics* **5**, 902 (1999).
23. T. Juhasz, G. Djotyan, F. H. Loesel, *et al.*, *Laser Physics* **10**, 495 (2000).
24. N. Shen, C. B. Schaffer, D. Datta, *et al.*, in *Conference on Lasers and Electro-Optics* (Optical Society of America, Baltimore, MD, 2001), p. 403.
25. F. W. D. Rost, *Fluorescence Microscopy* (Cambridge University Press, Cambridge, 1992).
26. M. Born and E. Wolf, *Principles of optics* (Pergamon Press, 1980).

27. J. S. Ploem and H. J. Tanke, *Introduction to fluorescence microscopy* (Oxford University Press, Oxford).
28. M. Chalfie and S. Rain, *Green Fluorescent Protein Properties, Applications, and Protocols* (Wiley-Liss, 1998).
29. S. Wang and T. Hazelrigg, *Nature* **369**, 400 (1994).
30. V. J. Allan, *Protein localization by fluorescence microscopy* (Oxford University Press, Oxford, 2000).
31. J. Noack and A. Vogel, *IEEE Journal of Quantum Electronics* **35**, 1156 (1999).
32. M. H. Niemz, *Laser-tissue interactions: fundamentals and applications* (Springer, Berlin; New York, 1996).
33. D. N. Nikogosyan, A. A. Oraevsky, and V. Rupasov, *Chemical Physics* **77**, 131 (1983).
34. A. Vogel, J. Noack, G. Huttman, *et al.*, in *SPIE Photonics West: Commercial and biological applications of ultrafast lasers IV*, San Jose, CA, 2002), Vol. 4633A, p. 23.
35. A. Heisterkamp, T. Ripken, H. Lubatschowski, *et al.*, *Applied Physics B: Lasers and Optics* **74** (2002).
36. U. K. Tirlapur, K. Konig, C. Peuckert, *et al.*, *Experimental Cell Research* **263**, 88 (2001).
37. B. Boudaiffa, P. Cloutier, D. Hunting, *et al.*, *Science* **287**, 1658 (2000).
38. K. Konig, W. Riemann, and W. Fritzsche, *Optics Letters* **26**, 819 (2001).
39. D. G. Jay and T. Sakurai, *Biochimica et Biophysica Acta* **874**, M39 (1999).
40. A. Khodjakov, R. W. Cole, B. R. Oakley, *et al.*, *Current Biology* **10**, 59 (2000).

41. A. Khodjakov, R. W. Cole, and C. Rieder, *Cell Motility and the Cytoskeleton* **38**, 311 (1997).
42. F. De Giorgi, L. Lartigue, and F. Ichas, *Cell Calcium* **28**, 365 (2000).
43. R. Rizzuto, P. Pinton, W. Carrington, *et al.*, *Science* **280**, 1763 (1998).
44. T. J. Collins, M. J. Berridge, P. Lipp, *et al.*, *The EMBO Journal* **21**, 1616 (2002).
45. M. K. Park, M. C. Ashby, G. Erdemli, *et al.*, *The EMBO Journal* **20**, 1863 (2001).
46. N. Wang, J. P. Bulter, and D. E. Ingber, *Science* **260**, 1124 (1993).
47. A. Lin, G. Krockmalnic, and S. Penman, *Proceedings of National Academy of Sciences USA* **87**, 8565 (1990).
48. M. Krendel, G. Sgourdas, and E. M. Bonder, *Cell Motility and the Cytoskeleton* **40**, 368 (1998).

Chapter 5

Multiphoton Imaging

Because the pulse energy required for precise photodisruption in cells is only on the order of a couple of nanojoules, it is possible to perform disruption using a high repetition rate femtosecond laser oscillator system. Furthermore, with only a small number of the pulses needed for photodisruption, the rest of the pulse train can be used to image cell samples in real-time with high resolution in a multiphoton microscopy configuration. In this chapter we discuss the principle of multiphoton microscopy and the technical details of constructing a multiphoton microscope in combination with a femtosecond laser nanosurgery apparatus.

5.1 Multiphoton laser scanning microscopy principles

The necessity for a three-dimensional imaging technique comes from the fact that many biological processes occur inside a cell and below layers of tissue. An *in vivo* study of a system requires minimal effects on the system's physiological and functional behaviors in order to fully understand these processes. Among existing 3-D imaging methods,

optical imaging provides resolution of a single micrometer or less, does relatively little harm to biological tissue, and is capable of following fast dynamic processes in biological samples on the millisecond timescale [1]. Multiphoton laser-scanning microscopy was first demonstrated by Denk *et al.* It has unique advantages over conventional single photon imaging systems and is suitable for both *in vivo* and *in vitro* imaging of biological samples.

5.1.1 Multiphoton vs. single photon imaging

Single photon fluorescence imaging, including confocal laser scanning microscopy, relies on the absorption and emission of fluorescent molecules inside a specimen. A single photon with a wavelength within the absorption band of the fluorophore promotes the molecule to an excited state. After thermal equilibration, the fluorophore relaxes back to the ground state and emits a red-shifted photon. The probability of fluorescent signal generated from a given axial plane depends on the density of the excitation photons available, *i.e.* the light intensity, and the number of fluorophores in the plane. In a plane closer to the focus, although excitation photon intensity increases in the smaller cross-sectional area, the fluorophore number decreases by the same amount. Thus for a given fluorophore, the fluorescence probability is constant from any given axial plane regardless of the focusing of the incident beam. Consequently, fluorescent photons are generated with an equal probability throughout the entire axial extent of the incident beam as illustrated in Figure 5.1*a*.

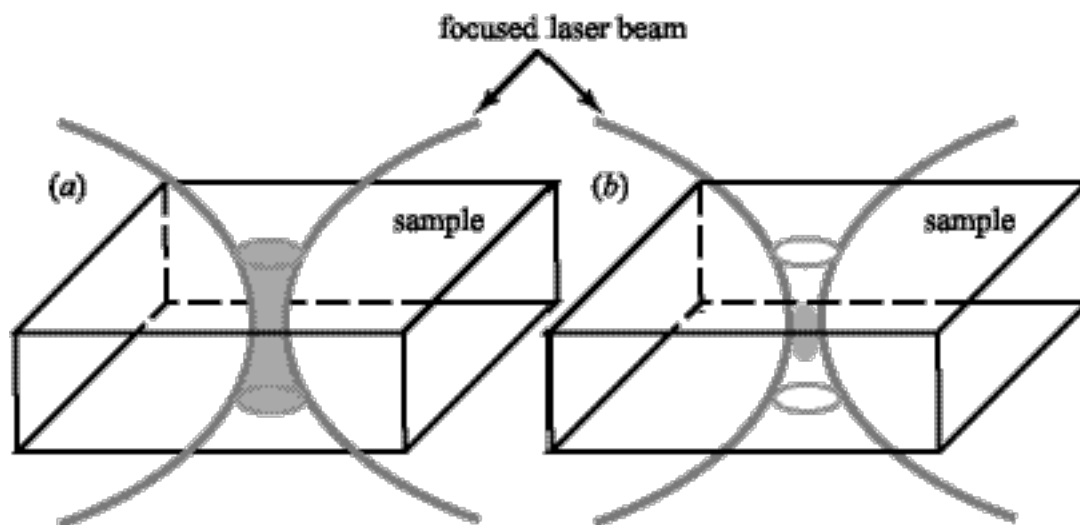


Figure 5.1 Fluorophore excitation volume in (a) single-photon microscopy and (b) multiphoton microscopy. Shaded areas represent absorption volume from which fluorescence photons are generated.

The fluorescence generated from planes outside the focal plane contributes to the background noise, decreasing axial resolution and the signal-to-noise ratio. Furthermore, photobleaching resulting from the single photon absorption process occurs everywhere in the excitation light path, reducing fluorescence signal over time. One of the methods used to increase axial resolution is the addition of a confocal pinhole in front of the detector. The pinhole preferentially passes fluorescent light generated near the focus. However, because a large number of photons is blocked by the pinhole, more intense excitation sources such as lasers are often used to make up for the generally low signal level. Hence, photobleaching is unavoidable. In general, confocal microscopy works well with optically thin samples, in which scattering is relatively less important. In thick samples, on the other hand, scattering increases substantially. A greater number of fluorescence photons from the focal volume are deflected from their original trajectories, are blocked by the confocal pinhole, and do not contribute to the imaging. Similarly, an increasing

portion of the fluorescence from outside the focus deviates from its path and may pass through the pinhole, reducing the signal-to-noise ratio.

Multiphoton imaging is based on the same fluorescence principle. However, instead of using a single photon to excite the fluorophore, the energy of multiple photons at a longer wavelength than the fluorophore excitation wavelength are absorbed simultaneously by the molecule. Figure 5.2 schematically illustrates such a process. The probability of multiphoton absorption thus scales with the n^{th} power of the incident laser intensity where n is the number of photons needed to bridge the energy gap between the ground and excited states of the fluorescent molecule. This nonlinearity of the absorption process provides the intrinsic mechanism for high axial resolution, and hence optical sectioning capability, since absorption only occurs in a small focal volume where the laser intensity is high.

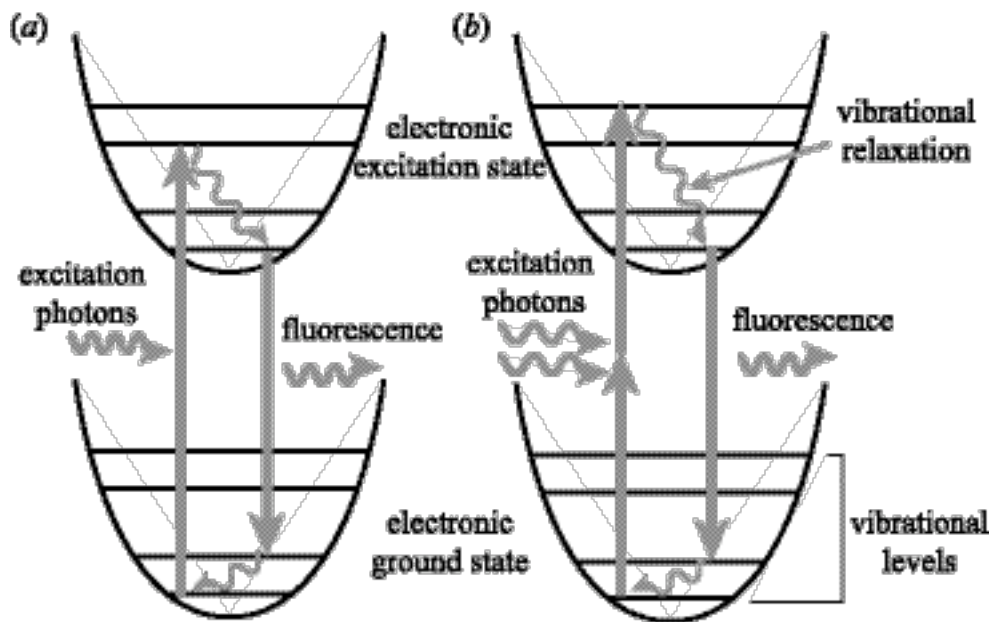


Figure 5.2 Energy diagrams of fluorescence process. (a) one-photon and (b) two-photon excitations.

It is also this small absorption volume that provides a solution to some of the problems confocal laser scanning microscopes face. Firstly, because the absorption is limited only to the focal volume, out-of-focus bleaching of fluorophores is greatly avoided. Secondly, since the fluorescence is only generated within the focus at any given time, no spatial filter is needed on the detection side. All the photons that reach the detector (*e.g.*, a photomultiplier tube) can be collected and assigned to a pixel corresponding to the position of the focus. This detection scheme means that a higher collection efficiency can be achieved, and is easier to align than a confocal setup.

Because the absorption depends strongly on excitation light intensity, it is necessary to choose a laser source that provides a high enough intensity to generate a significant multiphoton fluorescence signal. At the same time, a relatively low average power must be maintained in order to avoid thermal damage to the sample. The femtosecond laser pulses from a Ti:sapphire laser oscillator are well suited for use in two-photon imaging because of their high intensity and low average power [2, 3]. The near infrared wavelength of a Ti:sapphire laser is especially desirable for imaging biological samples as infrared light is much less destructive compared to UV or near-UV excitation wavelength used in some confocal microscopes.

5.1.2 Resolution in multiphoton imaging

The 3-D resolution of a microscope is ordinarily determined by the volume to which a point light source is imaged (the point spread function). In a laser-scanning imaging system based on the multiphoton absorption principle with no aperture, this volume is

exactly the excitation volume [4, 5]. The lateral and axial resolutions should then be related to the longitudinal and transverse intensity profiles of the incident laser beam. Because the absorption depends on the n^{th} power of the excitation intensity in multiphoton imaging, the multiphoton excitation volume should be smaller compared to the volume of which fluorescence is detected in a conventional single photon laser scanning confocal microscope [4, 5]. This suggests that multiphoton imaging has a better resolution than the traditional confocal microscopy, but in reality the enhancement is counterbalanced by the need to use a much longer wavelength for excitation.

Since femtosecond laser sources are usually used in multiphoton microscopes, the intensity distribution is that of a focused Gaussian shaped laser beam. The lateral resolution can then be expressed as the beam waist at the focus obtained using the paraxial approximation of the Fresnel diffraction theory:

$$r = 2\omega_0 = 2 \frac{\lambda_0 f}{\pi \omega} \quad (5.1)$$

where λ_0 is the excitation laser wavelength, f is the focal length of the lens, and ω is the beam waist before the focusing lens. Since f/ω is just the cotangent of the focusing angle α , Equation 5.1 can be rewritten as a function of $\sin\alpha$, which is just the numerical aperture (NA) of the lens in air,

$$r = 2\omega_0 = 2 \frac{\lambda_0}{\pi} \frac{\sqrt{1 - \text{NA}^2}}{\text{NA}} \quad (5.2)$$

For a 1.4 NA oil immersion objective (0.92 NA in air), equation (5.2) suggests that the ideal resolution r is ~213 nm when using 800 nm laser excitation.

The axial resolution is limited by the axial extend of the excitation light near the focus and depends on the confocal parameter of the focused beam:

$$z_{confocal} = 2 \frac{\lambda_0}{\pi} \frac{1 - NA^2}{NA^2} \quad (5.3)$$

When a 1.4 NA oil immersion objective is used, $z_{confocal}$ will be less than 100 nm.

In reality, the resolution is much worse than this prediction because the paraxial approximation is no longer valid for very high NA. It is believed that $z_{confocal}$ starts to plateau at about 0.8 NA. As a result, the expected lateral resolution and the depth discrimination of a multiphoton laser scanning microscope with a 1.4 NA oil immersion objective are similar to that of a confocal laser scanning microscope, and are on the order of a few hundred nanometers.

5.1.3 Discussion

Single photon fluorescence microscopy has been used for over a century [7]. The linear absorption (single photon absorption) process, which the microscopy is based on, has been extensively studied for even longer. Nowadays, there exists hundreds of fluorophores well characterized and understood for the purpose of single photon fluorescence microscopy. Multiphoton fluorescence imaging was first proposed in 1978 [6], and two-photon laser scanning microscopy was demonstrated by Denk *et al.* in 1990 [1]. Since the basic principles of multiphoton imaging are different from the traditional single photon imaging, it is necessary to look at some of the issues unique to multiphoton imaging such as the absorption cross-section of fluorophores and possible photodamage and bleaching effects.

5.1.3.1 Multiphoton absorption cross section and excitation spectra of fluorophores

Let us first compare the signal levels from one- and two-photon microscopes. The number of fluorescence photon collected F (photon per second per molecule) in fluorescence microscopy depends on the fluorescence quantum efficiency (η) of the fluorophore, the collection efficiency of the detector (ϕ) and the number of excitation photons absorbed (N_{abs}).

$$F = \eta \phi N_{abs} \quad (5.4)$$

The collection efficiency of the detector should be independent of the excitation process (single or multiphoton). The fluorescence quantum efficiency should also remain constant if we assume that it is the same excitation state that is reached in both processes. The number of absorbed photons at a wavelength, on the other hand, is proportional to the excitation intensity I for one-photon and I^2 for two-photon absorption, and the absorption cross section, $\delta(\lambda)$ which also depends on the process, of the molecule, will therefore vary for different processes. To achieve the brightest imaging result, it is therefore necessary to use fluorophores with large absorption cross sections and also choose the excitation source at a wavelength corresponding to the highest absorption cross section. Furthermore, in quantitative imaging, one needs to know the value of δ in order to relate the signal level to specific experimental parameters.

The one-photon absorption properties of many fluorophores have been carefully studied. From these properties, unfortunately, no quantitative predictions can be made about the two-photon absorption characteristics simply because the two processes are intrinsically different quantum mechanically [7]. The quantum-mechanical selection rules

for two-photon absorption differ from those for the one-photon process [8-10]. In fact, for isolated atoms, a one-photon transition is strictly forbidden for two-photon transitions and vice versa. Of course, for complex dye molecules, this exclusion usually does not hold due to the reduced symmetry and vibration effects in the molecules [11]. It is nonetheless important to gain some insight on the basic behaviors of the fluorophores in order to choose the best excitation source and fluorophore for the best images.

Many experiments were carried out in the 1990s to better understand the behavior of fluorophores under two-photon excitation, especially those widely used in biological studies. Because of the nature of this higher order process, the two-photon absorption cross section for a fluorophore is usually much smaller than that for the one-photon process. The typical value of the one-photon absorption cross section for commonly used fluorophores (including autofluorescent proteins) is $\sim 10^{-16}$ cm²/photon [12]. The absorption cross section is on the order of 10^{-50} cm⁴ s/photon [12-14] for a two-photon process. This means that the two-photon fluorescence signal is intrinsically small compared to one-photon fluorescence even when a high-intensity excitation source is used, which makes it a challenge for signal detection in two-photon imaging. However, because of the recent recognition of the advantages and an increasing popularity of two-photon fluorescence imaging in life science, a great deal of effort has been put into synthesizing fluorescent molecules with large two-photon absorption cross sections [15].

Another complication brought to light by the two-photon absorption cross section measurements is that the “twice-the-wavelength” rule (that the two-photon absorption peaks at twice the wavelength of the one-photon absorption maximum) is not always right. Instead, it has been observed that the two-photon absorption spectra for

fluorophores (which follow the behavior of their absorption cross section) often exhibit a peak wavelength blue shifted relative to twice their one-photon absorption. For example for fluorescein, the wavelength corresponding to twice the one-photon absorption wavelength should be about 1000 nm. It has been shown that two-photon absorption peaks at 760 and 800 nm. Although the exact quantum-mechanical basis of this phenomenon is not yet understood, it has been suggested that the shift occurs because some higher excited singlet states can be reached with greater probability by two-photon than one-photon excitation [16, 17]. The absorption cross section at the blue-shifted wavelength is then higher than at exactly twice the one-photon peak. Because of this complication, one has to be careful in choosing the two-photon excitation wavelength when using fluorophores even when their one-photon absorption properties are well-known.

5.1.3.2 Multiphoton bleaching and damage of fluorophores

Two other important issues associated with all fluorescence imaging in biological research are photobleaching of the fluorophore and photodamaging of the sample. Again, because multiphoton microscopy is relatively new, the exact effects of bleaching and damaging due to multiphoton excitation are not yet fully understood. However, there are still a number of experimental observations that offer some insight.

Because of the low absorption cross section, two-photon fluorescence imaging requires high intensity laser excitation of the fluorophore in order to generate appreciable signal. This high intensity can also lead to a higher photobleaching rate within the focal

volume. In fact, it is well known that many standard fluorophores exhibit significantly reduced photochemical lifetimes when subjected to two-photon excitation [18]. Also, unlike in one-photon excitation where the fluorophore bleaching rate increases linearly with excitation intensity, the bleaching rate for two-photon fluorescence often exhibits an increase proportional to I^2 [18]. This result suggests that the mechanism that leads to photobleaching in two-photon fluorescence is significantly different from the one-photon process. Further investigation is needed to better understand of the physical principles that govern the multiphoton bleaching, and to reduce any unnecessary bleaching during experiments.

In laser scanning fluorescence microscopy, continuous wave (CW) or high-repetition rate pulsed lasers are often used for excitation to achieve a fast frame rate. One consequence of having a large number of pulses constantly irradiating a biological sample is the heating and thermal damage of the sample due to absorption of the laser energy by water or other molecules. For multiphoton imaging, it is necessary to use short pulsed lasers instead of a CW sources because high intensity can be achieved with a femtosecond laser at a much lower average power compared to a CW source. The appropriate intensity/energy level should be determined in order to obtain a good fluorescence signal and avoid bleaching and heating the sample. The typical level of pulse energy in imaging thin samples such as cell cultures is on the order of picojoules per pulse. Of course the choice of the exact excitation pulse energy depends on the sample and the fluorophore used.

5.2 Multiphoton microscope setup

Multiphoton laser scanning microscopes are now commercially available. Generally, such a setup consists of an excitation light source, scanning device, focusing and translation apparatus, and detection system. We have constructed a multiphoton laser scanning microscope in our lab for the purpose of combining imaging and subcellular surgery into one complete system. The schematic diagram of the system is illustrated in Figure 5.3. In this section, we will discuss the technical details of the microscope design, and illustrate at the end how subcellular surgery can be achieved with the same set up.

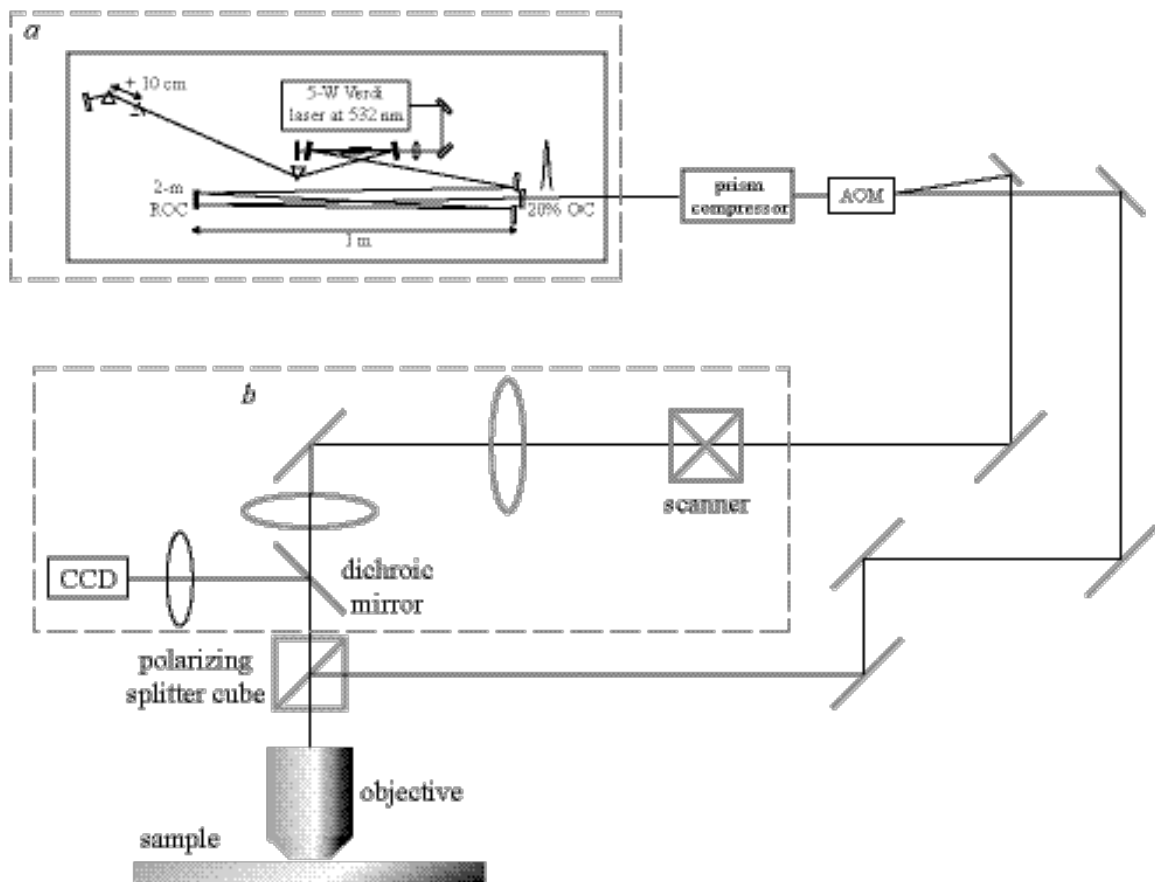


Figure 5.3 Schematic diagram of the multiphoton laser scanning microscope and laser surgery setup. The long-cavity Ti-sapphire laser is illustrated in (a), and the scanning optics in (b). Mirrors are 800-nm high reflector unless noted otherwise.

5.2.1 Laser source

As mentioned in the previous section, the excitation light source for a multiphoton microscope has to meet three requirements. Firstly, it has to have a wide wavelength tunability in order to excite different fluorophores. Secondly, it has to be able to achieve a high intensity with relatively low average power in order to generate enough fluorescence signal from fluorophores with a small absorption cross section and avoid sample heating. Thirdly, the laser has to operate at high repetition rate or CW in order to produce image frames at a fast rate. A Ti:sapphire laser oscillator satisfies all three requirements. The short duration of the pulse guarantees a large pulse power, hence high intensity, but the average power is low. The laser runs at a MHz repetition rate, fast enough to generate images at video-rate¹. And it has a tunable range from 700 to 1000 nm which covers most of the commonly used fluorophores in biology.

We used a modified Ti:sapphire long-cavity laser oscillator (Figure 5.3a) as described in Chapter 2 for multiphoton imaging. The laser produces 20-nJ, 55-fs pulses at 25-MHz repetition rate. Compared to a standard Ti:sapphire oscillator, we gain energy per pulse but lose repetition rate. We also insert an acoustic optical modulator (AOM) in the laser beam path. The AOM allows us to switch out a desired number of pulses from the 25 MHz pulse train by applying a high voltage. The extra pulse energy and the ability

¹ To image an area of 512 by 512 pixels at video rate (30 frames/second), one needs > 8 million laser pulses per second (assuming one pulse per pixel).

to switch out pulses are needed to perform subcellular surgery in our study as will be seen in the last part of this section.

5.2.2 Imaging and scanning system

The layout of the scanning and imaging part of the microscope is shown in Figure 5.3*b*. The excitation light enters the focusing objective via an epi-fluorescence path. The galvanometer-driven x - y scanning device (Cambridge Technology Inc.) scans the laser beams. A dichroic mirror (CVI Inc.) that reflects wavelengths lower than 630 nm is used to direct the fluorescence to the detector.

The design of the scanning scheme is the heart of the microscope. The laser beam needs to completely fill the back aperture of the objective in order to achieve the highest numerical aperture the objective is designed for and create the smallest focal volume. The scanning system also has to produce a true, distortion-free image. The essential idea is to be able to move the focus of the laser beam on a plane only by changing the angle at which the beam enters the back aperture of the objective without actually shifting the beam position on the back aperture, and hence affecting the degree of filling (see Figure 5.4*a*).

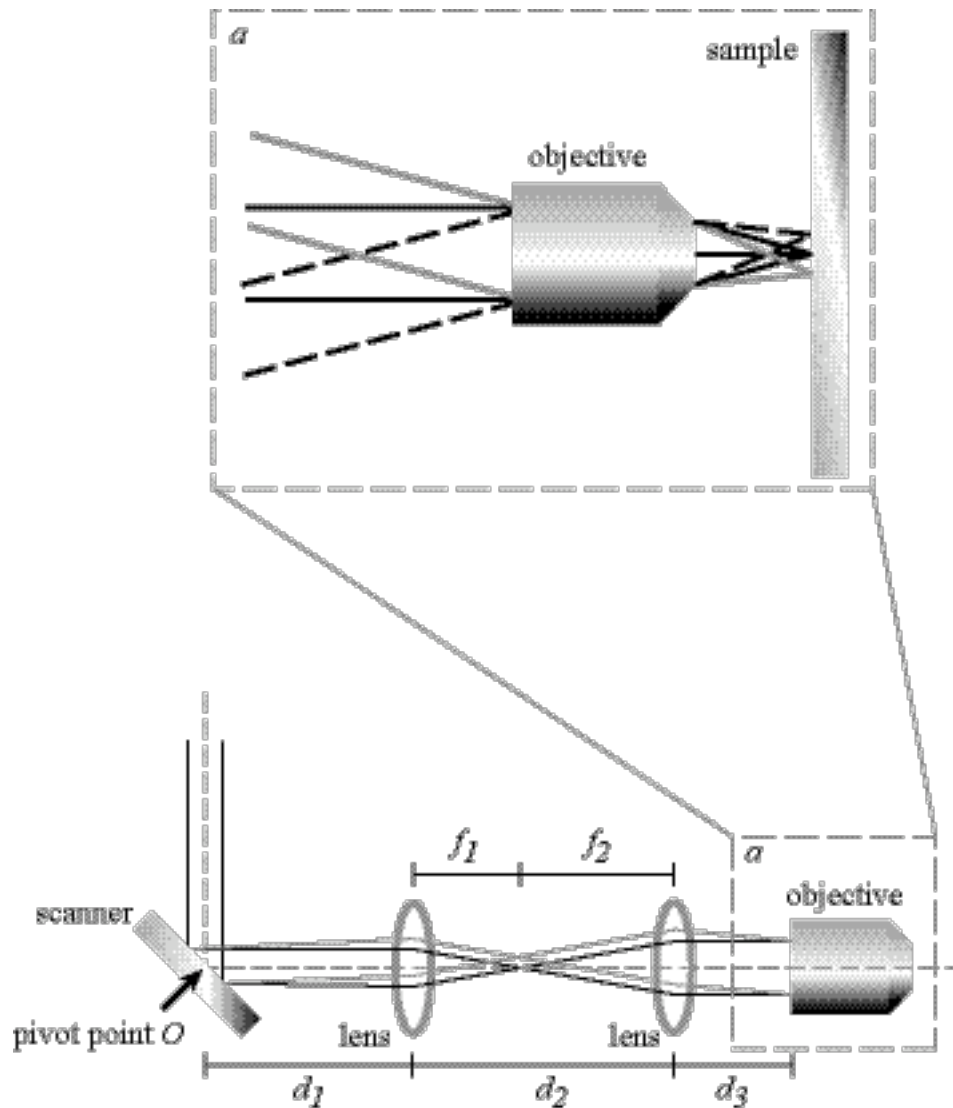


Figure 5.4 Alignment of the optics in the optical scanner of the multiphoton laser scanning microscope. The dotted line indicates the central axis of the system. The beam paths and the foci change as the scanner rotates about its pivot point as illustrated in (a).

To satisfy this requirement, we place a telescope that consists of two lenses in front of the objective (Figure 5.4). The telescope serves two purposes. The mirrors in a scanner are usually small in size. The laser beam incidents on the scanner therefore can not be very large. By selecting the right focal length for the lenses in the telescope, the diameter of the laser beam can be expanded or contracted so that it completely fills the

back aperture of the objective. The same telescope also relay-images the laser beam from the scanner to the back aperture of the objective with the pivot point of the scanner imaged exactly to the center of the back aperture of the objective. The principle of the scanning system is illustrated in Figure 5.4. The scanner rotates around a pivot point O . The collimated laser beam hits the scanner with the beam center on this pivot point. Depending on the rotation of the scanner, the beam is reflected at a different angle and enters the telescope at a different part of the lens. After the telescope, the beam is re-collimated. When it enters the back aperture of the objective, the center of the beam remains at the center of the back aperture, and the incident angle is determined by the angle of the scanning mirrors. The degree of filling is therefore unchanged, and the beam is focused to a spot on the focal plane. The size of the image area is determined by the angle of rotation of the scanner. The position of each element in the scanning system and the focal lengths of the lenses as indicated in Figure 5.4 and obey the following relations:

$$\begin{aligned} d_2 &= f_1 + f_2 \\ d_1 &= \frac{(f_1)^2}{f_2} + f_1 - d_3 \left(\frac{f_1}{f_2}\right)^2 \end{aligned} \quad (5.5)$$

5.2.3 Detection

There are two detection schemes in multiphoton imaging which we will call the imaging and raster-scanning modes. In the imaging mode, which is what we are using in our system at the moment, the fluorescence signal is focused onto a 2-D detector such as a CCD camera. An image frame is generated when the entire image area is covered by the scanner. The frame rate is determined by how fast an area of interest can be scanned.

With a commercially available scanning device and a MHz repetition rate laser, it is possible to achieve video-rate imaging of an area $100 \times 100 \mu\text{m}$. The advantage of this detection scheme is that the instrumentation requirement is relatively simple, as no special post-processing program is needed. But because of the low signal level, the 2-D detector (CCD) must be very sensitive. Also, when dealing with thick samples, fluorescence photons can be scattered out of the focal volume and introduce blurring in the image.

An image can also be generated in the raster-scanning mode, in which a photon detector such as photomultiplier tube (PMT) or photodiode is used. Again, the fluorescence photons are focused onto the detector. The signal collected within a time interval that corresponds to the time the laser beam is focused on one spot of the sample is recorded and assigned to one pixel of the final image corresponding to the position of the focus at that time. An image frame is then built up pixel by pixel and reconstructed at the end by computer. The advantage of this detection scheme is that all of the fluorescence photons, even if they are subsequently scattered, can be collected and attributed to the exact focal spot. The drawback is then the need for a computer hardware and software system to keep track of where the scanned focal spot is and relate the measured signal to that spot for image reconstruction at the end.

5.2.4 Combining multiphoton imaging with subcellular surgery

Subcellular surgery in living cells requires femtosecond laser pulses with energy on the order of a nanojoule (see Chapter 4). To perform surgery, the switched pulse has to be

focused onto the cell sample. Therefore, we insert a polarizing beam splitter cube in front of the objective lens (see Figure 5.3). The polarizing cube allows light in one polarization to go through and reflects the light in the orthogonal direction. The multiphoton imaging system uses most of the pulses from the long-cavity oscillator, which is p polarized and passes through the polarizing cube. When it is necessary to perform subcellular surgery, we take the switched pulse from the AOM, change its polarization direction to s and recombine it with the imaging beam through the polarizing cube. Both beams are focused through the same objective lens and imaging and surgery are achieved simultaneously.

5.3 System performance and discussion

We have tested the performance of our multiphoton imaging system by imaging fluorescent microspheres that are commercially available (Molecular Probes). Figure 5.5 shows an image of 2- μm microspheres taken with the microscope. The intensity profile of one microsphere in the inset has a FWHM (full width half maximum) of 2 μm .

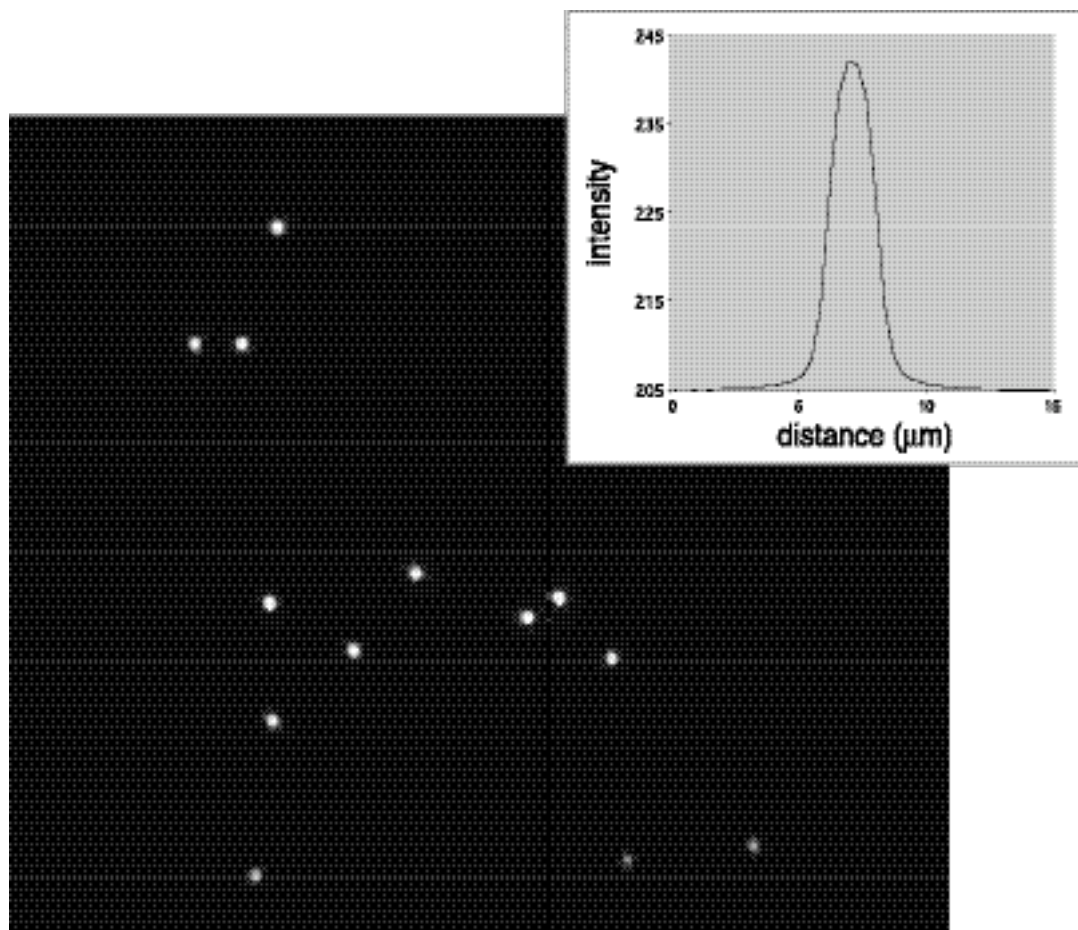


Figure 5.5 Multiphoton laser scanning microscopy image of yellow-green fluorescence microspheres. The intensity profile of one microsphere in the inset shows a FWHM radius of $\sim 2 \mu\text{m}$.

Multiphoton imaging with the help of autofluorescent proteins will enable us to follow dynamic processes in cells in 3-D. For example, fluorescence photobleaching recovery, which is used to observe 3-D molecular diffusion in cells, can be done on a multiphoton microscope. Comparing to a confocal microscope on which the experiments are currently done, the fluorescence bleaching volume is better estimated in a multiphoton microscope since the excitation (bleaching) occurs only in the focal volume [19]. Multiphoton microscopy can also be used to study membrane dynamics of embryos during cell fusion and measure actin dynamics [20, 21]

The advantage of multiphoton imaging becomes more pronounced when dealing with thick and/or scattering samples. The excitation wavelength used in multiphoton fluorescence imaging is longer (near infrared) than that of a confocal microscope (visible to near-UV). This results in less scattering and deeper penetration in tissue (see Chapter 3) for multiphoton imaging. The ability to resolve structures deep in the bulk of the tissue ($> 200 \mu\text{m}$) is now used to image blood flow in individual capillaries in rat cerebral cortex [22, 23].

By combining multiphoton imaging and subcellular laser surgery, we can physically perturb or remove structures in living cells that are involved in cellular processes being studied. With this technique, it is possible to investigate cell dynamics, repair mechanisms, spatially regulated signaling and other phenomena involving intracellular structures and subcellular heterogeneity.

5.4 Summary

In this chapter, we have briefly discussed the principles of multiphoton microscopy. With all the advantages we have highlighted, multiphoton imaging will become more important to biological research. Many improvements have already been made in the past few years. However, it is still a relatively new technique and more study needs to be done to ensure further advances.

References

1. W. Denk, J. H. Strickler, and W. W. Webb, *Science* **248**, 73 (1990).
2. K. Konig, *Journal of Microscopy* **200**, 83 (2000).
3. C. Xu, W. Zipfel, J. B. Shear, *et al.*, *Proceedings of National Academy of Sciences USA* **93**, 10763 (1996).
4. R. M. Williams, D. W. Piston, and W. W. Webb, *FASEB* **8**, 804 (1994).
5. O. Nakamura, *Optick* **93**, 39 (1993).
6. C. J. R. Sheppard and R. Kompfner, *Applied Optics* **17**, 2879 (1978).
7. J. B. Pawley, *Handbook of biological confocal microscopy* (Plenum Press, 1995).
8. R. Loudon, *The Quantum Theory of Light* (Oxford University Press, London, 1983).
9. D. M. Friedrich and W. M. McClain, *Annual Reviews of Physical Chemistry* **31**, 559 (1980).
10. R. R. Birge, *Journal of Chemical Physics* **70**, 165 (1979).
11. W. M. McClain, *Journal of Chemical Physics* **55**, 2789 (1971).
12. G. A. Blab, P. H. M. Lommerse, L. Cognet, *et al.*, *Chemical physics Letters* **350**, 71 (2001).
13. C. Xu and W. W. Webb, *Journal of the Optical Society of America B (Optical Physics)* **13**, 481 (1996).
14. M. A. Albota, C. Xu, and W. W. Webb, *Applied Optics* **37**, 7352 (1998).

15. M. Drobizhev, A. Karotki, and A. Rebane, *Optics Letters* **26**, 1081 (2001).
16. J. P. Hermann and J. Ducuing, *Optics Communications* **6**, 101 (1972).
17. D. J. Bradley, H. R. Hutchinson, T. M. H. Koetser, *et al.*, *Proceedings of the Royal Society of London* **328**, 97 (1972).
18. P. S. Dittrich and P. Schwille, *Applied Physics B-Lasers and Optics* **73**, 829 (2001).
19. E. B. Brown, E. S. Wu, W. Zipfel, *et al.*, *Biophysical Journal* **77**, 2837 (1999).
20. J. M. Squirrell, J. G. Wokosin, J. G. White, *et al.*, *Nature Biotechnology* **17**, 763 (1999).
21. W. A. Mohler, J. S. Simske, E. M. Williams-Masson, *et al.*, *Current Biology* **8**, 1087 (1998).
22. D. Kleinfeld, P. P. Mitra, F. Helmchen, *et al.*, *Proceedings of National Academy of Sciences USA* **95**, 15741 (1998).
23. P. S. Tsai, N. Nishimura, E. J. Yoder, *et al.*, *Methods for In Vivo Optical Imaging* (CRC Press, 2002).

Chapter 6

Summary and outlook

The advances in ultrashort laser technology have made femtosecond lasers robust enough to be introduced into many research fields including clinical and biological studies. Laser tissue interaction has remained an active area of research since the invention of the laser in the 1960s. The understanding of basic principles of intense femtosecond laser pulse interaction with biological tissue is the key to initiate new applications and promote better technologies of using femtosecond lasers in medicine and biology. In this chapter, we review briefly the results presented in this thesis, and discuss possible future works.

We focused our discussion of the fundamental physical principles of light-matter interaction on the nonlinear effects such as intensity-dependent index of refraction and photoionization. Femtosecond laser induced surgical effects are the results of these nonlinear processes.

In our study of laser skin tissue surgery, we tightly focus the femtosecond laser pulses using a microscope objective lens on the surface and inside the bulk of skin tissues. Ablation at the tissue surface and incision through different tissue layers can be produced with higher precision than other techniques. We also demonstrate that

femtosecond laser pulses can be used to create cavities inside the bulk of a tissue without affecting the tissue surface. The size of the cavity is determined by the laser energy deposited in the tissue.

With the high precision of femtosecond pulses, we can also target subcellular organelles in fixed and live cells. Using fixed cell samples, we determined that the energy threshold for femtosecond laser disruption of structures in cells is on the order of nanojoules. Single mitochondria within a live cell were disrupted at this energy without affecting cell viability.

Complex cell behaviors are the result of a combination of processes occurring in spatially distinct cellular domains. Using femtosecond subcellular surgery technique, one can study these behaviors by structurally modifying or removing the functional domains within single living cells. We investigated the organization of the mitochondrial network in the BCE cells, and observed that mitochondria function on an individual level instead of behaving as part of a network of connected organelles.

The ability to follow cellular dynamics in 3-D with high resolution is essential to biological research. By combining multiphoton imaging with subcellular surgery into one integrated system, we will be able to directly probe subcellular structural domains and observe cell response in real-time. This technique will be useful in studies of cell dynamics, chemotaxis, cell polarity, spatially regulated signaling, drug screening and other phenomena involving intracellular compartments and subcellular heterogeneity.